

Computational Homogenization Framework for Soft Elasto-Hydrodynamic Lubrication

Von der Fakultät für Maschinenbau
der Gottfried Wilhelm Leibniz Universität Hannover

zur Erlangung des akademischen Grades
Doktor-Ingenieur

genehmigte Dissertation
von

Dipl.-Ing.(FH) Michael Budt

geboren am 07.06.1978 in Hannover

2012

Herausgeber:

Prof. Dr.-Ing. Peter Wriggers

Verwaltung:

Institut für Kontinuumsmechanik
Gottfried Wilhelm Leibniz Universität Hannover
Appelstraße 11
30167 Hannover

Tel: +49 511 762 3220

Fax: +49 511 762 5496

Web: www.ikm.uni-hannover.de

© Dipl.-Ing.(FH) Michael Budt
Institut für Kontinuumsmechanik
Gottfried Wilhelm Leibniz Universität Hannover
Appelstraße 11
30167 Hannover

Alle Rechte, insbesondere das der Übersetzung in fremde Sprachen, vorbehalten. Ohne Genehmigung des Autors ist es nicht gestattet, dieses Heft ganz oder teilweise auf photomechanischem, elektronischem oder sonstigem Wege zu vervielfältigen.

ISBN 978-3-941302-04-4

1. Referent: Prof. Dr.-Ing. Peter Wriggers
2. Referent: Prof. İlker Temizer
Tag der Promotion: 15.12.2011

Abstract

The interaction between microscopically rough surfaces and hydrodynamic thin film lubrication is investigated at finite deformations. Within a coupled micro-macro analysis setting, the influence of roughness onto the macroscopic scale is determined using FE^2 -type homogenization techniques to reduce the overall computational cost. Exact to within a separation of scales assumption, a computationally efficient two-phase micromechanical test is proposed to identify the macroscopic interface fluid flux from a lubrication analysis performed on the deformed configuration of a representative surface element. Parameter studies show a strong influence of both roughness and surface deformation on the macroscopic response for isotropic and anisotropic surfacial microstructures.

Keywords: Reynolds equation, surface roughness, homogenization, finite deformation

Kurzbeschreibung

Die Wechselwirkung zwischen mikroskopisch rauen Oberflächen und einer Dünnschicht Flüssigkeitsschmierung werden unter der Annahme von großen Deformationen untersucht. In einem gekoppelten mikro-makro Problem wird der mikroskopische Rauigkeitseinfluss auf die Makroscale bestimmt. Um den Rechenaufwand zu reduzieren findet eine FE^2 artige Homogenisierungstechnik Verwendung. Ein effizienter mikromechanischer Zweiphasentest wird zur Bestimmung des makroskopischen Fluidflusses herangezogen wobei im ersten Schritt ein Körper mit rauer repräsentativer Oberfläche deformiert und im zweiten Schritt eine Flussanalyse auf der verformten Oberfläche durchgeführt werden. Parameterstudien von isotropen und anisotropen mikroskopischen Oberflächen zeigen einen starken Einfluss von Rauigkeit und Verformung auf den makroskopischen Fluidfluss.

Schlagworte: Reynoldsgleichung, Oberflächenrauigkeit, Homogenisierung, Große Deformationen

Acknowledgements

The present work arose under guidance of Prof. Dr.-Ing. habil. Peter Wriggers during my time at the Institute of Mechanics and Computational Mechanics (IBNM) and later at the Institute of Continuum Mechanics (IKM) of Leibniz Universität Hannover. The project was funded by a grant of the “Deutsche Forschungsgemeinschaft” (DFG)¹ within DFG Research Training Group 615: “Interaction of Modeling, Computation Methods and Software Concepts for Scientific-Technological Problems“.

First of all i would like to thank my advisor and first referee Prof. Dr.-Ing. P. Wriggers for giving me - as a graduate of a University of Applied Sciences - the opportunity to authoring the present work in an excellent working environment and for his support in presenting the research results on various conferences.

In the same breath i thank my former colleague and second referee Assistant Professor İlker Temizer for his lively interest in my work and particularly for many fruitful discussions and his encouragement whenever needed.

Furthermore i thank my colleagues of both Institutes for the pleasant working atmosphere and besides the beneficial technical discussions for their interest and support in regard to research and private concerns. Best wishes to all of you and good luck with your own research work.

Mein ganz besonderer Dank gilt meiner Familie und meinen Freunden. Ihr habt mich mit all Euren Möglichkeiten unterstützt und so in besonderem Maße zum Gelingen dieser Arbeit beigetragen. Dafür herzlichen Dank.

Hannover, December 2011

Michael Budt

¹German Research Foundation

Contents

1	Introduction	1
1.1	Motivation	1
1.2	Background and state of the art	2
1.3	Structure of the thesis	4
2	Continuum mechanics	7
2.1	Kinematics	7
2.1.1	Deformation gradient	8
2.1.2	Nanson's formula	9
2.1.3	CAUCHY-GREEN tensors	9
2.1.4	Strain	10
2.2	Balance equations	11
2.2.1	Balance of mass	11
2.2.2	Balance of momenta	12
2.2.3	Balance of energy	15
2.2.4	Thermomechanical balance equations	17
2.3	Constitutive solid equations	21
2.3.1	Linear elastic material	21
2.3.2	Hyperelastic material	22
3	REYNOLDS equation	25
4	Finite element method	35
4.1	Variational formulation	35
4.2	Linearization	37
4.3	Discretization	39
4.4	Solving nonlinear problems numerically	42
5	Finite element framework for elasto-hydrodynamic lubrication	45
5.1	Variational formulation	47
5.2	Linearization	48

5.3	Discretization	49
6	Macroscale numerical examples	55
7	Microscale test procedure	61
7.1	Homogenization fundamentals	61
7.2	Lubricant homogenization methodology	67
7.2.1	Interface testing procedure	67
7.2.2	Two-Phase micro mechanical test	69
7.2.3	Boundary conditions	75
7.2.4	Identification of macroscopic quantities	75
7.2.5	A micro-macro dissipation equality	77
8	Microscale numerical examples	79
8.1	Effects of solid incompressibility	81
8.2	Anisotropic/Isotropic surfaces	81
8.3	Deformation gradient	84
9	Conclusion	93
A	Contact Algorithms	95
B	Distributed computing	99
	Bibliography	102

Chapter 1

Introduction

1.1 Motivation

In many cases of engineering interest, two surfaces that appear to be macroscopically in contact are separated by a thin fluid film on the micro scale. The presence of such a film may be desirable or undesirable. The synovial fluid is critical to the healthy functioning of human joints [32] and lubricants are an integral design parameter in order to maintain the operation standards in various machinery by minimizing wear [58]. In ships the angular motion and momentum of an engine are transferred to the propeller via an axis, which commonly is routed by a water lubricated bearing [14, 46, 69]. On the other hand, wet road surfaces may lead to poor tire traction performance and eventually to hydroplaning [30, 45] while oil, a common lubricant, can also lead to reduced performance in wheel-rail contact [50] or it carries the load experienced by crankshafts in Otto-engines amongst a minimum of friction [16, 36]. An investigation of the tribological nature of such surfaces is an interdisciplinary task that forms the basis of the lubrication theory. See Hamrock et al. [33], Persson [56], Szeri [73] for extensive overviews of the field.

Experiments are expensive and computing power gets cheaper and enables the treatment of three dimensional problems of engineering interest, therefore numerical solution software has evolved and enjoys great popularity in science and industry [47, 48, 53, 60, 70]. Hence the present problem is tackled by making use of the *Finite Element Method (FEM)* which is a powerful tool in order to gain consolidated knowledge about nonlinear mechanical problems (of arbitrary geometry) prior to a products manufacturing [85, 88]. Although the finite element method is applicable to many mechanical branches, with a view to the current work just a few are mentioned. These are solid or fluid problems and furthermore interface problems where both solid and fluid interact with each other, cf. Persson

[56], Wriggers [84].

1.2 Background and state of the art

A central ingredient of the lubrication theory is the REYNOLDS equation [61] that is derived from the three-dimensional NAVIER-STOKES equations in the thin film limit. The REYNOLDS equation enables a predictive analysis of lubricated interfaces over a broad range of macroscopic contact situations and therefore plays a fundamentally practical role in circumventing a direct solution of the computationally more challenging NAVIER-STOKES equations. However, in its original form, the REYNOLDS equation assumes microscopically flat surfaces and employing a mean film thickness together with the original equation is generally unable to capture roughness effects accurately. Consequently, the construction of robust techniques of incorporating the effects of tribologically realistic surfaces that display roughness at various scales into the REYNOLDS equation has been of prime interest, in particular for surface texture design applications [74]. For the purposes of this work, attempts towards this goal may be grouped into two major categories: (i) stochastic approaches that augment the original REYNOLDS equation and (ii) homogenization techniques. The widely employed influential works of Patir and Cheng [54] and Patir and Cheng [55] introducing the flow factor method belong to the former category. This method regards the effect of three dimensional *isotropic* and *anisotropic* rigid surface roughness onto thin film lubrication problems. This is accomplished via shear and pressure flow factors – that are incorporated into the average REYNOLDS equation – based on empirical relations for the amplitude characteristics and by making use of autocorrelation parameters for the spectral characteristics of the surface roughness. Both surface generation and the smoothed flow problem are subject to numerical solution techniques. Additional early works of historical interest include Tripp [80] where anisotropic texture effects were accounted from an analytical view and Shukla [68] where an effective viscosity concept was introduced. For recent references, the reader is referred to Hamrock et al. [33] and Szeri [73].

Parallel to these efforts were perturbation techniques that operated directly on the fine scale pressure oscillations – see Tripp [80] for an early approach and Persson [57] for a recent development. Tripp directly computes the flow factors from the stochastic properties of the two rough surfaces. Elrod suggests a multi-scale analysis performed via an equation that relates mass flux of uniform direction to a REYNOLDS equation being smoothed by *flow-coefficients* formed by surface texture characteristics. Among other works, the small-parameter expansion approach of Elrod [28] can be considered as a precursor to modern homogenization techniques in lubrication and shows similarities with the asymptotic expansion

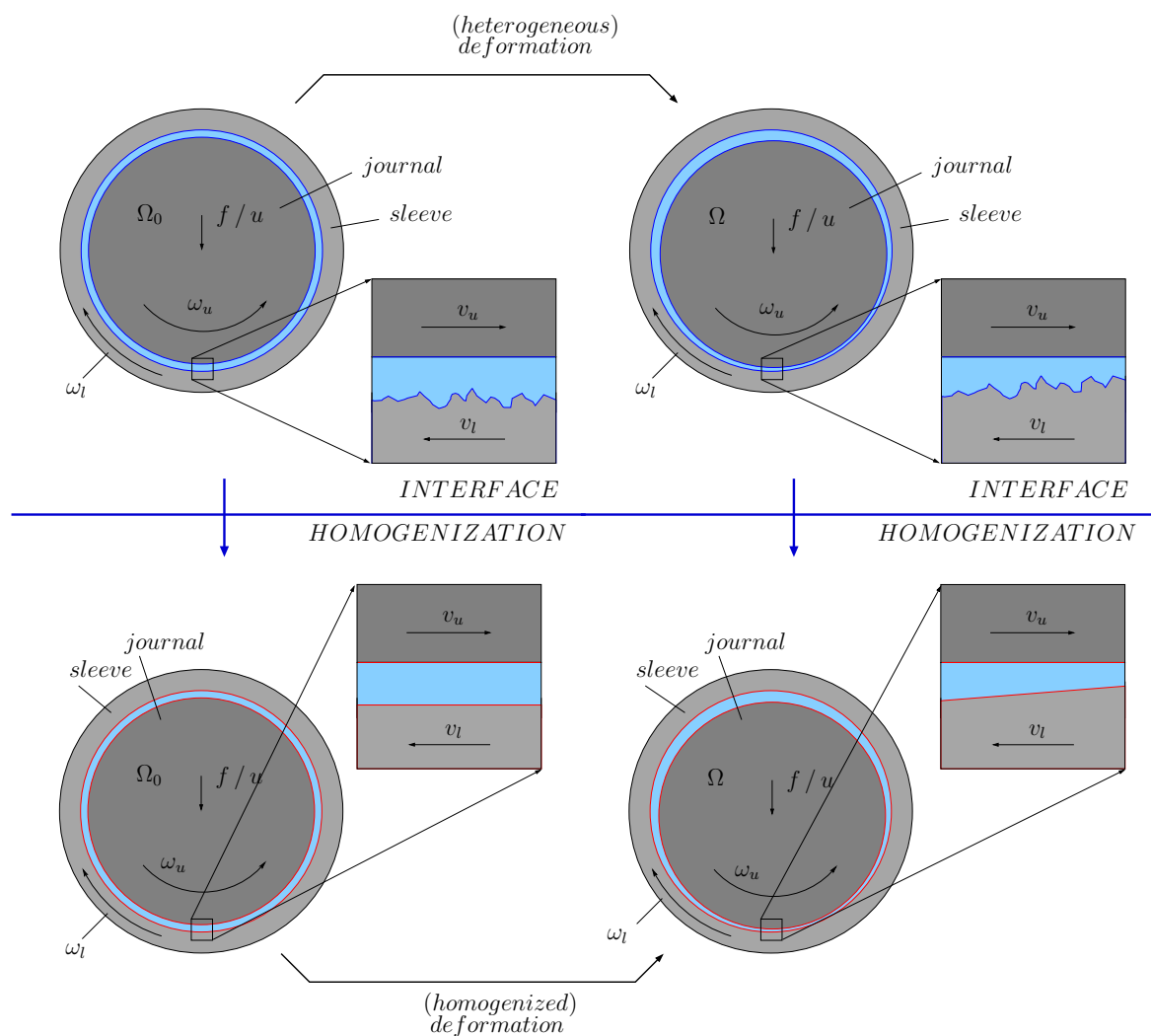


Figure 1.1: The lubrication homogenization idea is summarized. The original non-smooth boundary topography of the deformable body is replaced with a microscopically smooth one, leading to a homogenized problem with a lower discretization cost.

treatments that were first initiated in the context of heterogeneous media [7, 13, 65] – see Fabricius [31] for a review. For heterogeneous materials and interfaces, the homogenization approach based on the asymptotic expansion technique is exact in the sense that the macroscopic response of the medium can be extracted based on a given microstructure and microscale constitutive models without further simplification. Moreover, this inherently multiscale approach lends itself to computational homogenization frameworks (often referred to as FE^2) which can operate in pe-

riodic and random multiphysics settings, with discrete media or under constraint conditions like contact and in particular at finite deformations where analytical or closed-form mathematical approaches pose difficulties. While these advantages are at the expense of significant computational cost, their predictive potential complements and in some cases supersedes the alternatives offered by approximate homogenization techniques, such as estimates and bounds, based on simplified microstructures and constitutive relationships which are usually necessary to enable an analytical treatment of the multiscale problem. See Stupkiewicz [71], Temizer [76], Temizer and Wriggers [78], Torquato [79], Zohdi and Wriggers [89] for overviews with extensive references on computational homogenization techniques and their applications to finite deformation problems for materials and interfaces.

Asymptotic expansion based approaches have been analyzed for the REYNOLDS equation with and without cavitation, in the presence of compressibility effects as well as a possibly non-NEWTONIAN fluid in various works. Recent examples include Almqvist and Dasht [1], Almqvist et al. [2, 3], Bayada et al. [10], Jai and Bou-Said [42], Kane and Bou-Said [43, 44] – see also references therein for further remarks on the historical development of the approach. These enable exact treatments of the multiscale problem and are amenable to a computational implementation, thereby circumventing the demanding task of resolving microscopic roughness directly in the solution of the macroscopic problem, cf. (fig 1.1). Recently, analytical bounds for the macroscopic lubrication behavior have also been derived [4, 51], which are closely related to the bounds for heterogeneous materials [79]. Such bounds deliver a solution space for the performance of hydrodynamic lubrication as influenced by real measured surface roughness. Recent comparisons of homogenization and flow factor approaches may be found in Sahlin et al. [62, 63, 64]. As for heterogeneous media, absolute length scale dependence is also of concern in lubrication [40]. However, such effects are outside the scope of the present study.

1.3 Structure of the thesis

A summary of the underlying continuum mechanical basic principals is introduced in chapter 2 and inherits kinematical descriptions, balance equations and constitutive solid equations.

Due to the particular importance of the lubrication constitutive description for this work, REYNOLDS equation [61] is treated in chapter 3. In order to fulfill the linear momentum balance it can be derived from either the NAVIER-STOKES equation or alternatively from an infinitesimal volume element. Here a mixed approach was chosen. While the discussion of body forces and inertia terms is based on a dimensionless analysis of the full NAVIER-STOKES equation, the surface forces are deduced directly from an infinitesimal volume element. Subsequently a discussion

on different constraint formulations enforcing the effect of cavitation follows. At last all of these terms are subject to the mass balance (or continuity equation).

In order to extend the applicability of 2nd order differential equations (constitutive equations with balance laws) which have been discussed in the previous section, the finite element method will be introduced in terms of a solid description in chapter 4 and an elasto-hydrodynamic lubrication framework in chapter 5. Both chapters are subdivided into variational principles, linearization and discretization treatments. Furthermore a common employable numerical solution strategy for nonlinear problems is introduced briefly in chapter 4. Within the elasto-hydrodynamic lubrication description the “arbitrary Lagrangian-Eulerian” (ALE) description is used in order to handle the coupled interface problem efficiently. Furthermore a finite rotation formulation is introduced capable of handling curvilinear coordinates and large rotations as in shell problems. In order to familiarize the reader with results for a typical lubrication problem chapter 6 is introduced. The influence of cavitation is also demonstrated.

The major goal of this work is to introduce and investigate a computational homogenization framework for soft, i.e. finite deformation, elasto-hydrodynamic lubrication. The multiscale problem in the context of elasto-hydrodynamic lubrication has been investigated in Bayada et al. [11], Bohan et al. [15], Dowson [27] and explicit numerical solution strategies for the coupled problems of elasticity and lubrication have been proposed [45]. Although finite deformation effects have also been investigated in Shi and Salant [66], Shinkarenko et al. [67], Stupkiewicz and Maciniszyn [72], a sufficiently general computational homogenization framework that takes into account surface texture evolution effects due to large macroscopic deformations of the lubricated interface appears not to have been proposed. Section 7.2 constructs the homogenization methodology. In addition to a discussion of scale transition procedures, thermodynamical consistency of the proposed formulation is discussed by monitoring dissipation on micro- and macroscales. Finally, major aspects of the proposed approach are demonstrated in section 8 with an emphasis on finite deformation effects and the associated macroscopically anisotropic interface flow considerations. A critical discussion and an outlook complete the thesis in chapter 9.

Chapter 2

Continuum mechanics

In brief the fundamentals of Continuum Mechanics are introduced in this chapter. For detailed information the interested reader is referenced to Altenbach and Altenbach [5], Haupt [34], Holzapfel [39]. Here matter is considered at a macroscopic level without knowing its internal microscopic structure, hence assuming a uniform distribution of matter in space. Therefore the topics

- kinematics
- balance principles
- constitutive equations

as the basic tools to describe material behavior are introduced in the subsequent sections. In the kinematics section a material independent description of deformation and motion of bodies is introduced, followed by the principles of mass balance and linear momentum balance. These are general and hence material independent mathematical descriptions. Finally, the individual material properties are introduced via constitutive equations.

2.1 Kinematics

Basic mathematical considerations on the motion of a body and a description for deformation and its differential quantities are stated. Furthermore stretch and strain measures are constructed in order to depict the deformation - excluding translational and rotational rigid body motion - of a body in time.

Configuration and motion

At first, a body \mathcal{B} that is in a stress-free condition is introduced. This setting is referred to as the **initial configuration**. The volume it occupies is denoted

by Ω_0 and the surface via Γ_0 . The position of each point inside the body can be described by a vector \mathbf{X} . As a consequence of internal and external loads the body moves and deforms and fills out a volume Ω_t . The surface is denoted by Γ_t . This setting is called **current configuration**. In the current configuration each point can be described via a vector \mathbf{x} . This is depicted in figure 2.1, where φ denotes a mapping between the configurations, such that $\mathbf{x} = \varphi(\mathbf{X})$.

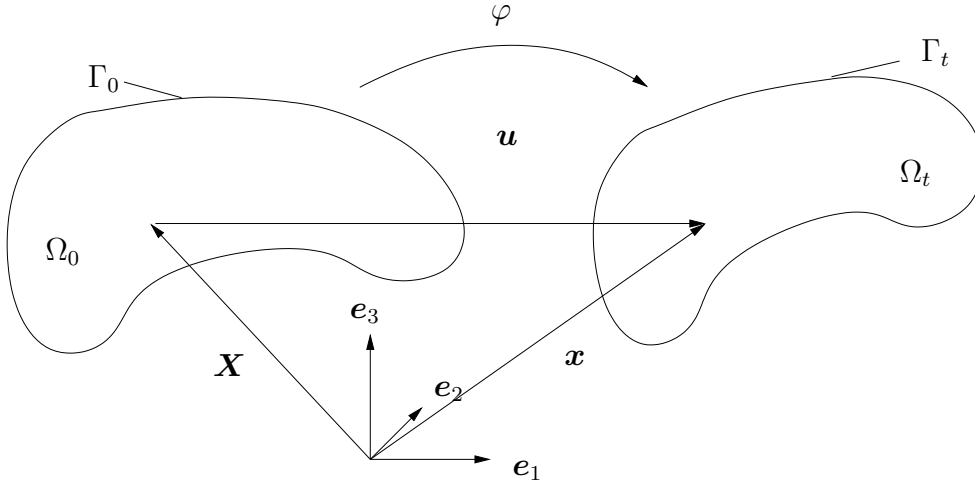


Figure 2.1: Motion of body \mathcal{B} .

The motion between the configurations is defined as

$$\mathbf{x}(\mathbf{X}, t) := \mathbf{X} + \mathbf{u}(\mathbf{X}, t), \quad (2.1)$$

where \mathbf{u} is the displacement.

2.1.1 Deformation gradient

The mapping of an infinitesimal line element $d\mathbf{X}$ in reference configuration and the same line element $d\mathbf{x}$ in current configuration is described by the *deformation gradient*

$$\mathbf{F} := \frac{\partial \mathbf{x}}{\partial \mathbf{X}} \quad (2.2)$$

and can be rewritten as

$$\mathbf{F} = \mathbf{1} + \underbrace{\frac{\partial \mathbf{u}}{\partial \mathbf{X}}}_{\mathbf{H}},$$

where \mathbf{H} denotes the *displacement gradient*.

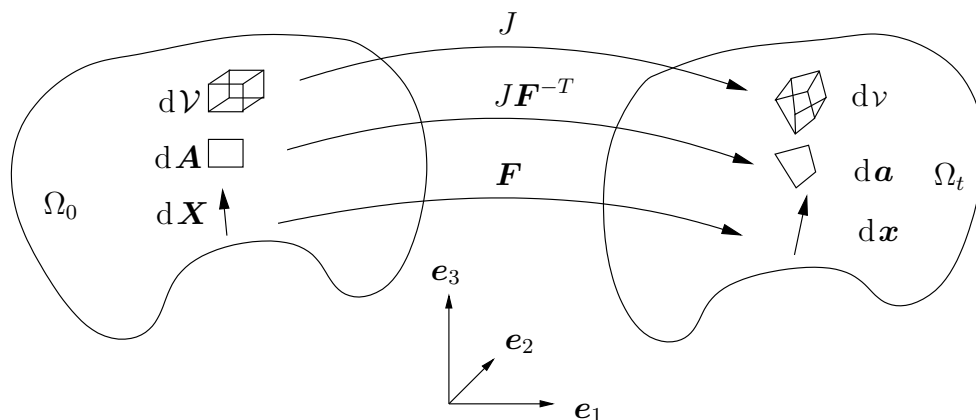


Figure 2.2: Differential quantities mapping between configurations.

2.1.2 Nanson's formula

Mapping the infinitesimal volume between the configurations is done by

$$dv = J dV, \quad (2.3)$$

where J is the Jacobian (also referred to as the *volume ratio*) that has to be greater than zero

$$J = \det[\mathbf{F}] > 0. \quad (2.4)$$

Deriving a relation between surface elements demands a mapping of unit vectors $\mathbf{N} \in \Gamma_0$ and $\mathbf{n} \in \Gamma$, that are normal to the surface in their respective configurations. This is achieved by Nanson's formula:

$$d\mathbf{a} = \mathbf{n} da = J\mathbf{F}^{-T}\mathbf{N} dA = J\mathbf{F}^{-T}d\mathbf{A} \quad (2.5)$$

2.1.3 CAUCHY-GREEN tensors

In order to prescribe the length of a line element on a body undergoing a deformation it is referred to previously introduced configurations. For both initial Ω_0 and current configuration Ω_t the length of an infinitesimal line element $d\mathbf{X}$ are denoted by dS and ds , respectively. These are defined by making use of the Euclidean norm $dS := \|\mathbf{dX}\|$ and $ds := \|\mathbf{dx}\|$. Expanding the length as follows

$$\begin{aligned} dS^2 &= \mathbf{dX} \cdot \mathbf{dX} = \left(\frac{d\mathbf{x}}{d\mathbf{X}} d\mathbf{X} \right) \cdot \left(\frac{d\mathbf{x}}{d\mathbf{X}} d\mathbf{X} \right) = \mathbf{X} \cdot \underbrace{\mathbf{F}^T \mathbf{F}}_{=: \mathbf{C}} \mathbf{X} \\ ds^2 &= \mathbf{dx} \cdot \mathbf{dx} = \left(\frac{d\mathbf{X}}{d\mathbf{x}} d\mathbf{x} \right) \cdot \left(\frac{d\mathbf{X}}{d\mathbf{x}} d\mathbf{x} \right) = \mathbf{x} \cdot \underbrace{\left(\mathbf{F} \mathbf{F}^T \right)^{-1}}_{=: \mathbf{b}} \mathbf{x} \end{aligned} \quad (2.6)$$

we obtain the **right CAUCHY-GREEN tensor** \mathbf{C} and **left CAUCHY-GREEN tensor** \mathbf{b} , prescribing the line stretch with respect to the initial and reference configuration. It can be shown that both CAUCHY-GREEN tensors are free of rotation \mathbf{R} . Besides the deformation gradient can be rewritten

$$\mathbf{F} = \mathbf{R}\mathbf{U} = \mathbf{v}\mathbf{R} \quad (2.7)$$

in terms of a rotation \mathbf{R} and stretch tensors \mathbf{U} or \mathbf{v} . Here the deformation is split into either a stretch followed by a rotation \mathbf{R} denoted as *right polar decomposition* $\mathbf{R}\mathbf{U}$ or it is split into a rotation \mathbf{R} followed by a stretch known as the *left polar decomposition* $\mathbf{v}\mathbf{R}$ of the deformation gradient. Since the rotation and stretches have the following properties

$$\mathbf{R}^T \mathbf{R} = \mathbf{R}\mathbf{R}^T = \mathbf{1}, \quad \mathbf{U} = \mathbf{U}^T, \quad \mathbf{v} = \mathbf{v}^T. \quad (2.8)$$

both CAUCHY-GREEN tensors read

$$\mathbf{C} = \mathbf{F}^T \mathbf{F} = \mathbf{U}^2 \quad \text{and} \quad \mathbf{b} = \mathbf{F}\mathbf{F}^T = \mathbf{v}^2. \quad (2.9)$$

Due to the positive definiteness of the right stretch tensor \mathbf{U} and the left stretch tensor \mathbf{v}

$$\mathbf{U} = \sqrt{\mathbf{C}} \quad \text{and} \quad \mathbf{v} = \sqrt{\mathbf{b}} \quad (2.10)$$

hold.

2.1.4 Strain

In order to depict the internal deviation between the point arrangements of both configurations *rigid body motion/rotation* must be eliminated. To accomplish this, the GREEN-LAGRANGE strain tensor \mathbf{E} - associated with Ω_0 - and GREEN-ALMANSI strain tensor \mathbf{e} - related to Ω_t - are constructed

$$\mathbf{E} = \frac{1}{2}(\mathbf{C} - \mathbf{1}) = \frac{1}{2}(\mathbf{H} + \mathbf{H}^T + \mathbf{H}^T \mathbf{H}) \quad (2.11)$$

and

$$\mathbf{e} = \frac{1}{2}(\mathbf{1} - \mathbf{b}^{-1}) = \frac{1}{2}(\mathbf{h} + \mathbf{h}^T - \mathbf{h}^T \mathbf{h}), \quad (2.12)$$

with the displacement gradients $\mathbf{H} = \text{Grad}[\mathbf{u}]$ and $\mathbf{h} = \text{grad}[\mathbf{u}]$ with respect to initial and current configuration, respectively. For small deformations high order terms can be neglected and strains \mathbf{E} , \mathbf{e} are written as

$$\boldsymbol{\epsilon} = \frac{1}{2}(\mathbf{H} + \mathbf{H}^T). \quad (2.13)$$

Making use of symmetry $(\bullet)^{sym} = \frac{1}{2}(\bullet + \bullet^T)$ the strain tensor $\boldsymbol{\epsilon}$ for small deformations comes out

$$\boldsymbol{\epsilon} = \mathbf{H}^{sym}. \quad (2.14)$$

2.2 Balance equations

In order to describe a mechanical system in a physically consistent fashion, general valid statements have to be fulfilled, namely balance equations.

2.2.1 Balance of mass

For all possible configurations *conservation of mass* (m) must be satisfied such that

$$m := \int_{\Omega_0} \rho_0(\mathbf{X}, t) \, d\mathcal{V} = \int_{\Omega_t} \rho(\mathbf{x}, t) \, d\nu \stackrel{!}{=} \text{const} > 0 \quad (2.15)$$

holds. Subsequently, making use of equation (2.3) and localizing leads to the local (point wise valid) mass balance relationship

$$\int_{\Omega_0} \rho_0(\mathbf{X}, t) \, d\mathcal{V} = \int_{\Omega_0} \rho(\mathbf{x}(\mathbf{X}, t), t) J(\mathbf{X}, t) \, d\mathcal{V}. \quad (2.16)$$

Considering a time dependent problem we need to derive the rate forms of equation (2.16) in material and spatial description

$$\begin{aligned} \overbrace{\dot{\rho}_0(\mathbf{X}) = \frac{D}{Dt} \rho_0(\mathbf{X}) = 0}^{\text{material rate}} &= \frac{D}{Dt} (\rho J) = \dot{\rho} J \\ &= \dot{\rho} J + \rho \dot{J}, \quad \text{with } \dot{J} = J \operatorname{div}[\dot{\mathbf{u}}] \\ &= \underbrace{\mathfrak{X}(\dot{\rho} + \rho \operatorname{div}[\dot{\mathbf{u}}])}_{\text{spatial rate}}. \end{aligned} \quad (2.17)$$

Finally, $\dot{\rho}$ can be derived in time and space, with $\dot{\rho}$ and ρ' evaluated at positions $\widehat{\mathbf{X}}$ and $\widehat{\mathbf{x}}$

$$\overbrace{\dot{\rho} := \frac{D\rho}{Dt} \Big|_{\mathbf{X}=\widehat{\mathbf{X}}}}^{\text{material}} = \overbrace{\frac{\partial \rho}{\partial t} \Big|_{\mathbf{x}=\widehat{\mathbf{x}}} + \operatorname{grad}[\rho] \cdot \dot{\mathbf{u}}}_{=:\rho'}^{\text{spatial}}, \quad (2.18)$$

and from product rule we get

$$\operatorname{div}[\rho \dot{\mathbf{u}}] = \operatorname{grad}[\rho] \cdot \dot{\mathbf{u}} + \rho \operatorname{div}[\dot{\mathbf{u}}] \quad (2.19)$$

such that in spatial (Eulerian) description equation (2.17) reads

$$\frac{\partial \rho}{\partial t} + \text{grad}[\rho] \cdot \dot{\mathbf{u}} + \rho \text{div}[\dot{\mathbf{u}}] = 0 \Leftrightarrow \rho' + \text{div}[\rho \dot{\mathbf{u}}] = 0, \quad (2.20)$$

which are commonly employed in *fluid dynamics*. Density must fulfill $\rho \stackrel{!}{>} 0$ for any material. For an incompressible fluid we observe a constant density throughout space $\text{grad}[\rho] \cdot \dot{\mathbf{u}} = 0$ and time $\dot{\rho} = 0$ and hence equation (2.20) simplifies to

$$\rho \text{div}[\dot{\mathbf{u}}] = \text{div}[\rho \dot{\mathbf{u}}] = 0. \quad (2.21)$$

2.2.2 Balance of momenta

For a body \mathcal{B} with a translational motion we define the *linear momentum* \mathbf{L}

$$\mathbf{L}(t) = \int_{\Omega_t} \rho \dot{\mathbf{u}} \, d\nu \quad (2.22)$$

and for a rotational motion relative to a fixed point \mathbf{x}_0 we define the *angular momentum* \mathbf{J}

$$\mathbf{J}(t) = \int_{\Omega_t} \mathbf{r} \times \rho \dot{\mathbf{u}} \, d\nu, \quad (2.23)$$

with $\mathbf{r}(\mathbf{x}) = \mathbf{x} - \mathbf{x}_0$. The fundamental axioms are called **balance of linear momentum** and **balance of angular momentum**. They evolve from the time derivatives of equations (2.22) and (2.23) reading

$$\dot{\mathbf{L}}(t) = \int_{\Omega} \rho \ddot{\mathbf{u}} \, d\nu = \mathbf{F}(t) \quad (2.24)$$

and

$$\dot{\mathbf{J}}(t) = \int_{\Omega} \mathbf{r} \times \rho \ddot{\mathbf{u}} \, d\nu = \mathbf{M}(t). \quad (2.25)$$

In terms of continuum mechanics these axioms are generalized equations of NEWTON's 1st and 2nd principle of motion, respectively. They equilibrate inertia forces of equations (2.24) and (2.25) to all forces \mathbf{F} and moments \mathbf{M} acting on the body.

The forces and moments can be split additively into portions acting on the surface Γ and the volume Ω of the current configuration:

$$\mathbf{F}(t) = \int_{\Gamma_t} \mathbf{t} \, da + \int_{\Omega_t} \mathbf{b} \, dv \quad (2.26)$$

$$\mathbf{M}(t) = \int_{\Gamma_t} \mathbf{r} \times \mathbf{t} \, da + \int_{\Omega_t} \mathbf{r} \times \mathbf{b} \, dv \quad (2.27)$$

Here, $\mathbf{b} = \rho \mathbf{g}$ is referred to as *body force*, representing for example gravity \mathbf{g} . According to CAUCHY'S **theorem** the CAUCHY traction vector \mathbf{t} can be evolved for both current and reference configuration to

$$\mathbf{t} = \boldsymbol{\sigma} \cdot \mathbf{n} \quad \text{and} \quad \mathbf{T} = \mathbf{P} \cdot \mathbf{N}, \quad (2.28)$$

respectively. Here $\boldsymbol{\sigma}$ is called CAUCHY (*true*) *stress tensor* and \mathbf{P} is known as 1st PIOLA-KIRCHHOFF (*nominal*) *stress tensor*. Both relate forces to an infinitesimal surface element in either the current configuration (da) or the reference configuration (dA):

$$\mathbf{t} \, da = \mathbf{T} \, dA. \quad (2.29)$$

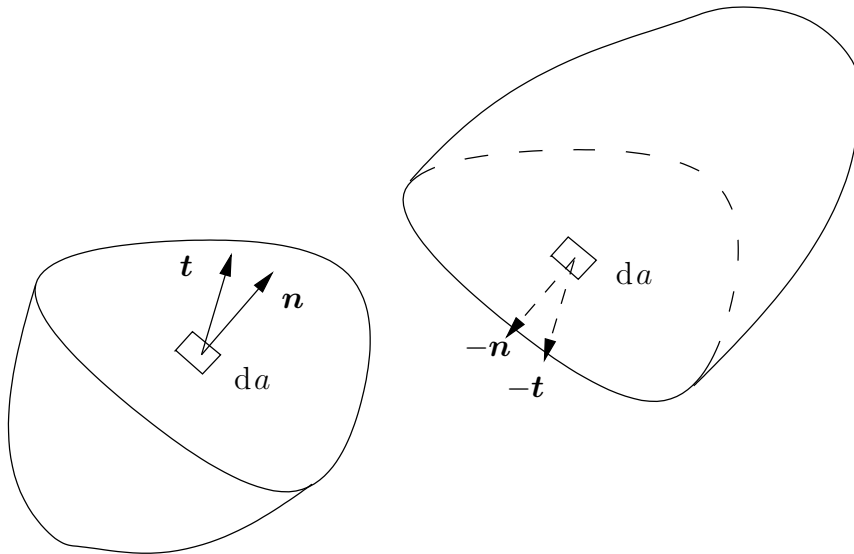


Figure 2.3: Cauchy stress inside a body.

In spatial description, introducing equation (2.28) into equations (2.26) and (2.27) the linear and angular momentum balance [eqs (2.24) and (2.25)] yields

$$\int_{\Omega_t} \rho \ddot{\mathbf{u}} \, d\nu = \int_{\Gamma_t} \boldsymbol{\sigma} \cdot \mathbf{n} \, da + \int_{\Omega_t} \mathbf{b} \, d\nu \quad (2.30)$$

and

$$\int_{\Omega_t} \mathbf{r} \times \rho \ddot{\mathbf{u}} \, d\nu = \int_{\Gamma_t} \mathbf{r} \times \boldsymbol{\sigma} \cdot \mathbf{n} \, da + \int_{\Omega_t} \mathbf{r} \times \mathbf{b} \, d\nu \quad (2.31)$$

and can be transformed to CAUCHY'S 1st **equation of motion** in spatial description. This is done by using the integral form of CAUCHY'S *theorem* [eqn (2.28)] and applying the divergence theorem

$$\int_{\Omega_t} \operatorname{div}[\bullet] \, d\nu = \int_{\Gamma_t} [\bullet] \cdot \mathbf{n} \, da \quad (2.32)$$

in such a way that we end up with the global and local form, of the CAUCHY'S 1st equation of motion

$$\begin{aligned} \int_{\Omega_t} (\operatorname{div}[\boldsymbol{\sigma}] + \mathbf{b} - \rho \ddot{\mathbf{u}}) \, d\nu &= \mathbf{0} \\ \operatorname{div}[\boldsymbol{\sigma}] + \mathbf{b} - \rho \ddot{\mathbf{u}} &= \mathbf{0}. \end{aligned} \quad (2.33)$$

In case of no acceleration ($\ddot{\mathbf{u}} = 0$) the above stated local form results in the equation for elasto-statics

$$\operatorname{div}[\boldsymbol{\sigma}] + \mathbf{b} = \mathbf{0}, \quad (2.34)$$

well-known as CAUCHY'S **equation of equilibrium**. CAUCHY'S 2nd **equation of motion** states that CAUCHY **stress tensor is symmetric**. Applying the divergence theorem from equation (2.32) to the angular momentum balance [eqn (2.31)] reads

$$\begin{aligned} \int_{\Omega_t} \mathbf{r} \times \rho \ddot{\mathbf{u}} \, d\nu &= \int_{\Omega_t} (\mathbf{r} \times \operatorname{div}[\boldsymbol{\sigma}] + \mathbf{s}) \, d\nu + \int_{\Omega_t} \mathbf{r} \times \mathbf{b} \, d\nu \\ \int_{\Omega_t} \mathbf{r} \times \underbrace{(\rho \ddot{\mathbf{u}} - \mathbf{b} - \operatorname{div}[\boldsymbol{\sigma}])}_{\stackrel{!}{=} 0 \text{ by [eqn(2.33)]}} \, d\nu &= \int_{\Omega_t} \mathbf{s} \, d\nu. \end{aligned} \quad (2.35)$$

Subsequently rewriting the last equation in index notation for an arbitrary volume leads to the statement

$$\begin{aligned}
0 = \mathbf{s} &= \varepsilon_{abc} \mathbf{e}_a \otimes \mathbf{e}_b \otimes \mathbf{e}_c : (\delta_{df} \mathbf{e}_d \otimes \mathbf{e}_f \cdot \sigma_{gh}^T \mathbf{e}_g \otimes \mathbf{e}_h) \\
&= \varepsilon_{abc} \sigma_{gh} \delta_{df} \delta_{fg} \delta_{bd} \delta_{ch} \\
&= \varepsilon_{abc} \sigma_{cb} \mathbf{e}_a \\
&= (\overset{!}{\sigma_{32} - \sigma_{23}}) \mathbf{e}_1 + (\overset{!}{\sigma_{13} - \sigma_{31}}) \mathbf{e}_2 + (\overset{!}{\sigma_{21} - \sigma_{12}}) \mathbf{e}_3
\end{aligned} \tag{2.36}$$

that demands CAUCHY's stress tensor being symmetric

$$\boldsymbol{\sigma} = \boldsymbol{\sigma}^T \tag{2.37}$$

in order to fulfill CAUCHY's 2nd equation of motion. In equation (2.36) the operator of permutation

$$\epsilon_{abc} := \begin{cases} 1; & a, b, c = (1, 2, 3), (2, 3, 1), (3, 1, 2) \\ -1; & a, b, c = (1, 3, 2), (3, 2, 1), (2, 1, 3) \\ 0; & a = b \text{ or } a = c \text{ or } b = c \end{cases} \tag{2.38}$$

and KRONECKER's delta

$$\delta_{ij} := \begin{cases} 1; & i = j \\ 0; & i \neq j \end{cases} \tag{2.39}$$

are used.

2.2.3 Balance of energy

Analogous to the transformation of **linear momentum balance** to CAUCHY's 1st equation of motion ([eqs (2.24) and (2.33)]) the **balance of mechanical power** can be evolved. Multiplying the external forces \mathbf{F} [eqn (2.26)] acting on a body with a velocity $\dot{\mathbf{u}}$

$$\mathcal{P}_{ext} := \mathbf{F}(t) \cdot \dot{\mathbf{u}} = \int_{\Gamma_t} \mathbf{t} \cdot \dot{\mathbf{u}} \, da + \int_{\Omega_t} \mathbf{b} \cdot \dot{\mathbf{u}} \, dv \tag{2.40}$$

and making use of the divergence theorem leads to

$$\mathcal{P}_{ext} = \int_{\Omega_t} \operatorname{div}[\boldsymbol{\sigma}^T \dot{\mathbf{u}}] \, dv + \int_{\Omega_t} \mathbf{b} \cdot \dot{\mathbf{u}} \, dv. \tag{2.41}$$

From the product rule we get an additive split of the 1st term on the right hand side and due to the symmetry of CAUCHY stress tensor the velocity gradient \mathbf{l}

$$\mathbf{l} := \operatorname{grad}[\dot{\mathbf{u}}] = \mathbf{d} + \boldsymbol{\omega}^0 \tag{2.42}$$

can be expressed by its symmetric part \mathbf{d} :

$$\mathcal{P}_{ext} = \int_{\Omega_t} (\operatorname{div}[\boldsymbol{\sigma}] \cdot \dot{\mathbf{u}} + \boldsymbol{\sigma} : \mathbf{d}) \, d\nu + \int_{\Omega_t} \mathbf{b} \cdot \dot{\mathbf{u}} \, d\nu. \quad (2.43)$$

Subsequently, expanding above equation via $\dot{\mathbf{L}} \cdot \dot{\mathbf{u}} - \dot{\mathbf{L}} \cdot \dot{\mathbf{u}} = 0$ reads

$$\mathcal{P}_{ext} = \int_{\Omega_t} (\rho \ddot{\mathbf{u}} \cdot \dot{\mathbf{u}} + \boldsymbol{\sigma} : \mathbf{d}) \, d\nu + \int_{\Omega_t} (\operatorname{div}[\boldsymbol{\sigma}] + \mathbf{b} - \rho \ddot{\mathbf{u}}) \cdot \dot{\mathbf{u}} \, d\nu, \quad (2.44)$$

where the 2nd term vanishes by virtue of equation (2.33). Finally, applying product to

$$\ddot{\mathbf{u}} \cdot \dot{\mathbf{u}} = \frac{1}{2} \left(\frac{\dot{\mathbf{u}} \cdot \dot{\mathbf{u}}}{\dot{\mathbf{u}} \cdot \dot{\mathbf{u}}} \right), \quad (2.45)$$

and introducing equation (2.40) into equation (2.44) the **balance of mechanical power** is obtained reading

$$\underbrace{\int_{\Gamma_t} \mathbf{t} \cdot \dot{\mathbf{u}} \, da + \int_{\Omega_t} \mathbf{b} \cdot \dot{\mathbf{u}} \, d\nu}_{\mathcal{P}_{ext}} = \underbrace{\frac{D}{Dt} \int_{\Omega_t} \frac{1}{2} \rho \dot{\mathbf{u}} \cdot \dot{\mathbf{u}} \, d\nu}_{\mathcal{K}} + \underbrace{\int_{\Omega_t} \boldsymbol{\sigma} : \mathbf{d} \, d\nu}_{\mathcal{P}_{int}}, \quad (2.46)$$

where the **kinetic energy** and **internal mechanical energy rates** are denoted by $\dot{\mathcal{K}}$ and \mathcal{P}_{int} , respectively. Here \mathcal{K} represents the energy stored due to velocity $\dot{\mathbf{u}}$, whereas the **internal mechanical power** (or **stress power**) \mathcal{P}_{int} is a consequence of deformation. It can be reformulated as follows

$$\begin{aligned} \mathcal{P}_{int} &= \boxed{\int_{\Omega_t} \boldsymbol{\sigma} : \mathbf{d} \, d\nu} = \boxed{\int_{\Omega_0} \boldsymbol{\tau} : \mathbf{d} \, d\nu} = \int_{\Omega_0} \boldsymbol{\tau} : \mathbf{l} \, d\nu = \int_{\Omega_0} \boldsymbol{\tau} \mathbf{F}^T : \dot{\mathbf{F}} \, d\nu \\ &= \boxed{\int_{\Omega_0} \mathbf{P} : \dot{\mathbf{F}} \, d\nu} = \int_{\Omega_0} \mathbf{F} \mathbf{S} : \dot{\mathbf{F}} \, d\nu = \int_{\Omega_0} \mathbf{S} : \mathbf{F}^T \dot{\mathbf{F}} \, d\nu \\ &= \boxed{\int_{\Omega_0} \mathbf{S} : \dot{\mathbf{E}} \, d\nu} \end{aligned} \quad (2.47)$$

Here $\boldsymbol{\tau}$, \mathbf{P} and \mathbf{S} denote the Kirchhoff, 1st and 2nd PIOLA-KIRCHHOFF stress tensors, respectively. Inside equation (2.47) the *work conjugate pairs* $(\boldsymbol{\sigma}, \mathbf{d})$, $(\boldsymbol{\tau}, \mathbf{d})$, $(\mathbf{P}, \dot{\mathbf{F}})$ and $(\mathbf{S}, \dot{\mathbf{E}})$ are obtained, where the operations

$$\begin{aligned} \boldsymbol{\tau} &= \mathbf{F} \mathbf{S} \mathbf{F}^T \\ \mathbf{S} &= \mathbf{F}^{-1} \boldsymbol{\tau} \mathbf{F}^{-T} \end{aligned} \quad (2.48)$$

are called **push-forward** and **pull-back**, respectively. Changing the configuration via $d\mathbf{v} = J d\mathcal{V}$ leads to

$$\boldsymbol{\tau} = J\boldsymbol{\sigma} \quad (2.49)$$

and hence [eqs (2.48) and (2.49)] rewrite

$$\begin{aligned} \mathbf{S} &= J\mathbf{F}^{-1}\boldsymbol{\sigma}\mathbf{F}^{-T} = \mathbf{F}^{-1}\boldsymbol{\tau}\mathbf{F}^{-T} = J\mathbf{F}^{-1}\mathbf{P} = \mathbf{S}^T \\ \boldsymbol{\sigma} &= J^{-1}\boldsymbol{\tau} = J^{-1}\mathbf{F}\mathbf{S}\mathbf{F}^T \end{aligned} \quad (2.50)$$

referred to as the **PIOLA transformation** and its inverse, respectively.

2.2.4 Thermomechanical balance equations

The *1st law of thermodynamics* states the thermal equilibrium by postulating that all energy within a system must be preserved. The *2nd law of thermodynamics* claims that a distinct direction of heat (or energy) transfer exists such that heat might only be transferred from high temperatures to low temperatures (but never reverse). It also puts restrictions on the nature of mechanical dissipation.

1st law of thermodynamics

The **balance of thermal energy** reads

$$\mathcal{P}_{int} + \mathcal{Q}_T = \dot{\mathcal{E}} = \frac{D\mathcal{E}(t)}{Dt} = \frac{D}{Dt} \int_{\Omega_t} e(\mathbf{x}, t) d\mathbf{v}, \quad (2.51)$$

where the **mechanical power**, **thermal power** and **internal energy** are denoted by \mathcal{P}_{int} , \mathcal{Q}_T and \mathcal{E} , respectively. Here $e(\mathbf{x}, t)$ denotes a *thermodynamic state variable* in current configuration. For the **thermal power** \mathcal{Q}_T a split is conducted

$$\mathcal{Q}_T = \int_{\Omega_t} r_T d\mathbf{v} - \int_{\Gamma_0} \mathbf{q}_T \cdot \mathbf{n} dA = \int_{\Omega_t} (r_T - \text{div}[\mathbf{q}_T]) d\mathbf{v}, \quad (2.52)$$

into an *internal heat source* r_T and a *heat flux* across the surface denoted by $q_{Tn} = -\mathbf{q}_T \cdot \mathbf{n}$. Introducing equation (2.51) into the mechanical balance equation (2.46) we obtain the identity

$$\begin{aligned} \dot{\mathcal{K}} + \dot{\mathcal{E}} &= \mathcal{P}_{ext} + \mathcal{Q}_T. \\ \frac{D}{Dt} \int_{\Omega_t} \left(\frac{1}{2} \rho \dot{\mathbf{u}}^2 + e \right) d\mathbf{v} &= \int_{\Gamma_t} \mathbf{t} \cdot \dot{\mathbf{u}} da + \int_{\Omega_t} \mathbf{b} \cdot \dot{\mathbf{u}} d\mathbf{v} + \\ &\quad \int_{\Omega_t} (\rho r - \text{div}[\mathbf{q}_T]) d\mathbf{v}, \end{aligned} \quad (2.53)$$

which leads to the **1st law of thermodynamics**

$$\begin{aligned} \frac{D}{Dt} \int_{\Omega_t} e \, d\nu &= \int_{\Omega_t} (\boldsymbol{\sigma} : \mathbf{d} - \operatorname{div}[\mathbf{q}_T] + \rho r) \, d\nu + \\ &\int_{\Omega_t} (\operatorname{div}[\boldsymbol{\sigma}^T] + \mathbf{b} - \rho \ddot{\mathbf{u}}) \cdot \dot{\mathbf{u}} \, d\nu, \end{aligned} \quad (2.54)$$

demonstrating **balance of energy**.

2nd law of thermodynamics

The **total production of entropy** \mathcal{G} accumulates the **rate of entropy** $\dot{\mathcal{S}}$ and the **rate of entropy input** $\tilde{\mathcal{Q}}$

$$\begin{aligned} \mathcal{G}(t) &= \frac{D}{Dt} \mathcal{S} - \tilde{\mathcal{Q}} \geq 0 \\ \text{or} \quad &= \frac{D}{Dt} \int_{\Omega_t} s(\mathbf{x}, t) \, d\nu + \int_{\Gamma_t} \mathbf{h} \cdot \mathbf{n} \, da - \int_{\Omega_t} \tilde{r} \, d\nu \geq 0 \end{aligned} \quad (2.55)$$

and states that entropy production can't be negative. Here $s(\mathbf{x}, t)$ denotes an *entropy state variable* with respect to the current configuration. In physics entropy is known as a concept to measure microscopic randomness and disorder quantitatively. From observation entropy quantities, namely *entropy flux* \mathbf{h} and *entropy source* \tilde{r} can be related to *heat flux* \mathbf{q}_T and *heat source* ρr by the inverse of the absolute temperature $\Theta^{-1}(\mathbf{x}, t)$, respectively.

$$\mathbf{h} = \frac{\mathbf{q}_T}{\Theta}, \quad \tilde{r} = \frac{r}{\Theta} \quad (2.56)$$

Combining equations (2.56) and (2.55) we obtain **CLAUSIUS-DUHEM inequality**

$$\int_{\Omega_t} \dot{s}(\mathbf{x}, t) \, d\nu + \int_{\Gamma_t} \frac{\mathbf{q}_T}{\Theta} \cdot \mathbf{n} \, da - \int_{\Omega_t} \frac{r}{\Theta} \, d\nu \geq 0. \quad (2.57)$$

Transforming the surface term while using both divergence theorem and product rule one may write

$$\int_{\Omega} (\dot{s} + (\operatorname{div}[\mathbf{q}_T] - r) \Theta^{-1} - \Theta^{-2} \mathbf{q}_T \cdot \operatorname{grad}[\Theta]) \, d\nu \geq 0, \quad (2.58)$$

where the integral cancels for an arbitrary body Ω bringing out the local form. This inequality can be rewritten in terms of *stress power* and *internal energy* introducing equation (2.54) and multiplying with Θ

$$\Theta \dot{s} + \underbrace{(\boldsymbol{\sigma} : \mathbf{d} - \dot{e})}_{=\text{div}[\mathbf{q}_T] - r} - \frac{1}{\Theta} \mathbf{q}_T \cdot \text{grad}[\Theta] \geq 0. \quad (2.59)$$

Furthermore rearranging and applying product rule to the 1st term on the left hand side gives

$$\frac{\text{D}}{\text{D}t} \underbrace{(\Theta s - e)}_{-\Psi :=} - \dot{\Theta} s + \boldsymbol{\sigma} : \mathbf{d} - \frac{1}{\Theta} \mathbf{q}_T \cdot \text{grad}[\Theta] \geq 0. \quad (2.60)$$

Here **HELMHOLTZ free energy function** $\Psi = \Psi(\Theta, s) = e - \Theta s$ can be identified which is expressed in terms of **LEGENDRE transformation**. For **isothermal conditions** ($\Theta = \text{const}$) the temperature remains constant throughout the body ($\text{grad}[\Theta] = 0$) and in time ($\dot{\Theta} = 0$) leading to

$$\begin{aligned} \dot{\Psi} &= \underbrace{\boldsymbol{\sigma} : \mathbf{d}}_{P_{int}} \\ \frac{\text{D}\Psi}{\text{D}t} &= \underbrace{\mathbf{P} : \dot{\mathbf{F}}}_{\dot{\Psi}} \end{aligned} \quad (2.61)$$

where the last column was obtained by virtue of the *work conjugated pairs*, cf. [eqn (2.47)]. Assuming a purely elastic material behavior, expanding the time derivatives on both sides

$$\frac{\partial \Psi}{\partial \mathbf{F}} : \dot{\mathbf{F}} \stackrel{!}{=} \mathbf{P} : \dot{\mathbf{F}} \quad (2.62)$$

we identify that $\Psi = \Psi(\mathbf{F})$. In other words Ψ must be a function of deformation \mathbf{F} . In case of an isotropic elastic response \mathbf{F} can be replaced by the invariants $I_{\mathbf{C}}^a, I_{\mathbf{b}}^a$; $a \in 1, 2, 3$ of the **CAUCHY-GREEN tensors** $\mathbf{C} = \mathbf{F}^T \mathbf{F}$, $\mathbf{b} = \mathbf{F} \mathbf{F}^T$ or its principal stretches λ_i , $i \in 1, 2, 3$, respectively:

$$\Psi(\mathbf{F}) = \Psi(\lambda_1, \lambda_2, \lambda_3) = \Psi(I_{\mathbf{C}}^1, I_{\mathbf{C}}^2, I_{\mathbf{C}}^3) = \Psi(I_{\mathbf{b}}^1, I_{\mathbf{b}}^2, I_{\mathbf{b}}^3) \quad (2.63)$$

Per definition the invariants are given in terms of **CAUCHY-GREEN tensors** or principle stretches

$$\begin{aligned} \underbrace{\overbrace{\text{tr}[\mathbf{C}]}^{I_{\mathbf{C}}^1 :=} \quad \underbrace{\text{tr}[\mathbf{b}]}^{I_{\mathbf{b}}^1 :=}}_{I_{\mathbf{C}}^2 :=} &= \underbrace{\lambda_1 + \lambda_2 + \lambda_3}_{I_{\mathbf{C}}^1 :=} = \underbrace{\text{tr}[\mathbf{b}]}_{I_{\mathbf{b}}^1 :=} \\ \underbrace{\frac{1}{2} (\text{tr}[\mathbf{C}]^2 - \text{tr}[\mathbf{C}^2])}_{I_{\mathbf{C}}^2 :=}} &= \underbrace{\lambda_1^2 \lambda_2^2 + \lambda_2^2 \lambda_3^2 + \lambda_3^2 \lambda_1^2}_{I_{\mathbf{C}}^2 :=} = \underbrace{\frac{1}{2} (\text{tr}[\mathbf{b}]^2 - \text{tr}[\mathbf{b}^2])}_{I_{\mathbf{b}}^2 :=} \\ \underbrace{\det[\mathbf{C}]}_{I_{\mathbf{C}}^3 :=} &= \underbrace{\lambda_1^2 \lambda_2^2 \lambda_3^2}_{I_{\mathbf{C}}^3 :=} = J^2 = \underbrace{\det[\mathbf{b}]}_{I_{\mathbf{b}}^3 :=} \end{aligned}$$

The eigenvalues λ_i^2 , $i \in 1, 2, 3$ and hence the principal stretches $\lambda_i \in 1, 2, 3$ of the CAUCHY-GREEN tensors \mathbf{C} and \mathbf{b}

$$\mathbf{C} := \sum_{i=1}^3 \lambda_i^2 \mathbf{N}_i \otimes \mathbf{N}_i, \quad \mathbf{b} := \sum_{i=1}^3 \lambda_i^2 \mathbf{n}_i \otimes \mathbf{n}_i \quad (2.64)$$

can be calculated by spectral decomposition. As previously defined we may interchange the *work conjugated pairs* in equation (2.62), with e.g. $(\mathbf{S}, \dot{\mathbf{E}})$

$$\mathbf{S} = \frac{\mathrm{D}\Psi}{\mathrm{D}\mathbf{E}} = 2 \frac{\mathrm{D}\Psi}{\mathrm{D}\mathbf{C}} = 2 \sum_{a=1}^3 \frac{\partial \Psi}{\partial I_{\mathbf{C}}^a} \frac{\partial I_{\mathbf{C}}^a}{\partial \mathbf{C}} \quad (2.65)$$

and hence obtain the 2nd PIOLA-KIRCHHOFF stress \mathbf{S} from the 1st derivative of Ψ and further can compute the CAUCHY stress $\boldsymbol{\sigma}$ via inverse PIOLA *transformation* [eqn (2.50)]:

$$\boldsymbol{\sigma} = J^{-1} \mathbf{F} \mathbf{S} \mathbf{F}^T = 2J^{-1} \sum_{a=1}^3 \frac{\partial \Psi}{\partial I_{\mathbf{C}}^a} \mathbf{F} \frac{\partial I_{\mathbf{C}}^a}{\partial \mathbf{C}} \mathbf{F}^T = 2J^{-1} \sum_{a=1}^3 \frac{\partial \Psi}{\partial I_{\mathbf{b}}^a} \mathbf{b} \frac{\partial I_{\mathbf{b}}^a}{\partial \mathbf{b}}, \quad (2.66)$$

where the last term on the right side can be evolved via

$$\underbrace{\mathbf{F} \left[\frac{\partial I_{\mathbf{C}}^1}{\partial \mathbf{C}} \right] \mathbf{F}^T}_{=1} = \mathbf{b}, \quad \underbrace{\mathbf{F} \left[\frac{\partial I_{\mathbf{C}}^2}{\partial \mathbf{C}} \right] \mathbf{F}^T}_{=I_{\mathbf{C}}^1 - \mathbf{C}} = I_{\mathbf{C}}^1 \mathbf{b} - \mathbf{b}^2, \quad \underbrace{\mathbf{F} \left[\frac{\partial I_{\mathbf{C}}^3}{\partial \mathbf{C}} \right] \mathbf{F}^T}_{=I_{\mathbf{C}}^2 \mathbf{C}^{-1}} = I_{\mathbf{C}}^2 \mathbf{1} \quad (2.67)$$

$$\mathbf{F} \mathbf{1} \mathbf{F}^T = \mathbf{b}, \quad \mathbf{F} \mathbf{C} \mathbf{F}^T = (\mathbf{F} \mathbf{F}^T)^2 = \mathbf{b}^2, \quad \mathbf{F} \mathbf{C}^{-1} \mathbf{F}^T = \mathbf{1}.$$

The elasticity tensor \mathbb{C} is derived from the 2nd derivative of Ψ

$$\mathbb{C} = \frac{\partial \mathbf{S}}{\partial \mathbf{E}} = \frac{\partial^2 \Psi}{\partial \mathbf{E} \partial \mathbf{E}} = 4 \frac{\partial^2 \Psi}{\partial \mathbf{C} \partial \mathbf{C}}. \quad (2.68)$$

2.3 Constitutive solid equations

Constitutive equations are mathematical models of materials to depict the physical behavior. They can be classified according to the physical phenomenon, mechanical or thermal. Such a general distinction can be made according to the size of displacement and strain. Hence theories for small (linear) and large (finite) displacements and strains exist, e.g. *linear elastic material* and *hyper elastic material*. In case of elastic solids prominent examples are steel undergoing little strains and rubber experiencing finite strains as a consequence of applied forces. General principles to systematically develop material models are

- **Determinism:** A point's current stress state belongs clearly to the history of a body's motion,
- **Local action:** A point's stress state only depends on the history of motion of its near neighborhood,
- **Frame-Indifference** also referred to as **material objectivity** demands a constitutive equation to be mathematically formulated such that it is independent to the reference frame's position and its motion at a time t ,
- **Compatibility with the balance relations** may not be violated by any constitutive equation,

where further reference and a more detailed list are given by Haupt [34].

2.3.1 Linear elastic material

For an elastic homogeneous body \mathcal{B} under isothermal conditions and assuming small deformations equations (2.62) and (2.68) can be used to obtain the 2nd PIOLA-KIRCHHOFF stress tensor \mathbf{S} and the elasticity tensor \mathbb{C} , respectively. With the strain energy function Ψ

$$\Psi = \frac{\lambda}{2} \text{tr}^2[\boldsymbol{\epsilon}] + G \text{tr}[\boldsymbol{\epsilon}^T \boldsymbol{\epsilon}] \quad (2.69)$$

and making use of equation (2.66) CAUCHY stress tensor reads

$$\boldsymbol{\sigma} = 2G\boldsymbol{\epsilon} + \lambda \text{tr}[\boldsymbol{\epsilon}]\mathbf{1}. \quad (2.70)$$

The elasticity tensor \mathbb{C} can be computed according to equation (2.68)

$$\mathbb{C} = 2G\mathbb{I}_{iklm} + \lambda\delta_{ik}\delta_{lm}, \quad (2.71)$$

with

$$\mathbb{I}_{iklm} = \frac{1}{2} (\delta_{ii} \delta_{km} + \delta_{im} \delta_{kl}) . \quad (2.72)$$

The constitutive response prescribed by these equations is referred to as **HOOKE'S law**. Here the LAMÉ constants λ , μ and the bulk modulus K read

$$\lambda := \frac{\nu E}{(1 + \nu)(1 - 2\nu)}, \quad G := \frac{E}{2(1 + \nu)} \quad \text{and} \quad K := \frac{3\lambda + 2\mu}{3},$$

where E and ν denote **YOUNG'S** modulus and **POISSON'S** ratio, respectively.

2.3.2 Hyperelastic material

A material is designated *hyper elastic* if its constitutive equation capturing the deformation behavior can be expressed by a **strain energy function** Ψ . For a rubber like material a possible strain energy function reads

$$\Psi(I_C^1, I_C^3) = \underbrace{\frac{G}{2}(I_C^1 - 3)}_{w(I_C^1)} + \underbrace{\frac{K}{4}(J^2 - 1) - \frac{K}{2}\ln[J]}_{u(J)} \quad (2.73)$$

which is known as **NEO-HOOKE** material. Setting Poisson's ratio to $\nu = 0.5$ enforces $K \rightarrow \infty$. Hence incompressible material behavior ($J = 1$) will be compelled, as it can be observed for rubber or fluids.

To obtain the 2nd **PIOLA-KIRCHHOFF** stress tensor by means of the strain energy function stated in [eqn (2.73)] we make use of equations (2.65) and (2.66)

$$\begin{aligned} \mathbf{S} &= \underbrace{G J^{-\frac{2}{3}} \left(\mathbf{1} - \frac{1}{3} I_C^1 \mathbf{C}^{-1} \right)}_{=: \mathbb{P}[\mathbf{1}]} + \underbrace{\frac{K}{2} (J^2 - 1) \mathbf{C}^{-1}}_{\mathbf{S}_{vol}} \\ \boldsymbol{\sigma} &= J^{-1} \mathbf{F} \left[\underbrace{G J^{-\frac{2}{3}} \left(\mathbf{1} - \frac{1}{3} I_C^1 \mathbf{C}^{-1} \right)}_{\mathbf{S}_{dev}} + \underbrace{\frac{K}{2} (J^2 - 1) \mathbf{C}^{-1}}_{\mathbf{S}_{vol}} \right] \mathbf{F}^T \\ &= G J^{-\frac{5}{3}} \left(\mathbf{b} - \frac{1}{3} \text{tr}[\mathbf{b}] \mathbf{1} \right) + \frac{K}{2} (J - J^{-1}) \mathbf{1} \end{aligned} \quad (2.74)$$

and deriving the elasticity tensor in material description we refer to [eqn (2.68)]

$$\begin{aligned} \mathbb{C} = & \overbrace{-\frac{2}{3}G \left[\mathbf{C}^{-1} \otimes \mathbf{S}_{vol} + \mathbf{S}_{vol} \otimes \mathbf{C}^{-1} + J^{-\frac{2}{3}} \text{tr}[C] \left(\frac{1}{3} \mathbf{C}^{-1} \otimes \mathbf{C}^{-1} - \mathbb{I}_{\mathbf{C}^{-1}} \right) \right]}^{\mathbb{C}_{dev}} \\ & + \overbrace{K \left[J^2 \mathbf{C}^{-1} \otimes \mathbf{C}^{-1} - (J^2 - 1) \mathbb{I}_{\mathbf{C}^{-1}} \right]}^{\mathbb{C}_{vol}}, \end{aligned} \quad (2.75)$$

with

$$\mathbb{I}_{\mathbf{C}^{-1}ABCD} = \frac{\partial \mathbf{C}_{AB}^{-1}}{\partial \mathbf{C}_{CD}} = -\mathbf{C}_{AC}^{-1} \mathbf{C}_{BD}^{-1} = \frac{1}{2} (\mathbf{C}_{AC}^{-1} \mathbf{C}_{BD}^{-1} + \mathbf{C}_{AD}^{-1} \mathbf{C}_{BC}^{-1}). \quad (2.76)$$

The transformation to the spatial description is defined by $\mathfrak{c}_{iklm} = \mathbf{F}_{iA} \mathbf{F}_{lC} \mathbf{F}_{mD} \mathbf{F}_{kB} \mathbb{C}_{ABCD}$ and hence \mathfrak{c} reads

$$\begin{aligned} \mathfrak{c} = & \overbrace{-\frac{2}{3}G \left[\mathbf{1} \otimes \boldsymbol{\tau}_{vol} + \boldsymbol{\tau}_{vol} \otimes \mathbf{1} + J^{-\frac{2}{3}} \frac{1}{3} \text{tr}[\mathbf{b}] (\mathbf{1} \otimes \mathbf{1} - \mathbb{I}) \right]}^{\mathfrak{c}_{dev}} \\ & + \overbrace{K \left[J^2 \mathbf{1} \otimes \mathbf{1} - (J^2 - 1) \mathbb{I} \right]}^{\mathfrak{c}_{vol}}. \end{aligned} \quad (2.77)$$

The spatial quantity \mathfrak{c} will prove useful in the Finite Element Method framework.

Chapter 3

REYNOLDS equation

In order to solve lubricated interface problems a constitutive equation is developed to capture the lubrication physics, which is subject to the continuity equation. The starting point for interface flow considerations is the mass balance together with the NAVIER-STOKES equations. The former is also known as the continuity equation statement [33, 83]. The NAVIER-STOKES equations can be derived from an infinitesimal volume element and capture fluid behavior in general. The fluid flux of the steady state REYNOLDS equation can be derived from the NAVIER-STOKES equations or directly from the infinitesimal volume element (as it will be done in this work) under certain assumptions, as shown in table 3.1. Developing

- (i) thin channel fluid flow, bounded by two surfaces in relative motion,
 - (ii) no fluid flow (velocity) across the fluid channel,
 - (iii) NEWTONIAN fluid,
 - (iv) incompressible fluid,
 - (v) body forces and inertia effects are negligible,
 - (vi) negligible pressure change across the fluid channel,
 - (vii) perfect stick of fluid molecules on solids,
 - (viii) density is constant across the fluid channel.
- 3D \rightarrow 2D flow

Table 3.1: REYNOLDS *assumptions*.

REYNOLDS equation demands to satisfy CAUCHY's 1st **equation of motion** [eqn (2.33)]

$$\operatorname{div}[\boldsymbol{\sigma}] + \mathbf{b} - \rho \ddot{\mathbf{u}} = \mathbf{0}.$$

Hence all forces (*surface forces*, *inertia forces* and *body forces*) acting on an infinitesimal fluid element (fig 3.1) have to be discussed. Further on the effect of

cavitation will be taken into account introducing a constraint condition acting on the fluid pressure p .

Inertia and body forces

REYNOLDS assumption tab 3.1_(v) demands the inertia and body forces to be negligible. This can be verified by comparing the viscous terms to both inertia and body terms. Therefore a dimensionless analysis of full NAVIER-STOKES equation [33, p.182] delivers estimates (e.g. \mathcal{R} , \mathcal{F}_n , $\frac{\mathcal{R}}{\mathcal{F}}$) to appraise *inertia*, *viscous* and *gravity terms* against each other. Starting with the REYNOLDS number

$$\mathcal{R} = \frac{\text{inertia}}{\text{viscous}} = \frac{\rho^c \dot{u}_i^c l_i^c}{\mu_0^c} \quad (3.1)$$

the requirement on the modified REYNOLDS number

$$\mathcal{R}_i = \mathcal{R} \left(\frac{h^c}{l_i^c} \right)^2 \ll 1 \quad (3.2)$$

states that inertia is negligible if the inequality holds. FROUDE number appraises *inertia vs. gravity*

$$\mathcal{F}_n := \frac{\text{inertia}}{\text{gravity}} = \frac{\dot{u}_i^c}{\sqrt{g l_i^c}} \quad (3.3)$$

where g denotes gravity acceleration. Subsequently combining FROUDE and REYNOLDS number

$$\frac{\mathcal{R}_i}{\mathcal{F}_n^2} = \frac{\text{gravity}}{\text{viscous}} = \frac{\rho^c g [h^c]^2}{\mu_0^c \dot{u}_i^c} \ll 1 \quad (3.4)$$

enables to estimate the influence of *gravity* and *viscous terms* onto the fluid flow.

Viscous force

The CAUCHY stress can be transformed into a volumetric and shear part

$$\boldsymbol{\sigma} = \frac{1}{3} \text{tr}[\boldsymbol{\sigma}] \mathbf{I} + \boldsymbol{\tau} . \quad (3.5)$$

The first assumption in table 3.1 pictures a setting where two plates under relative motion form a thin fluid flow channel as shown in figure 3.2. The stress

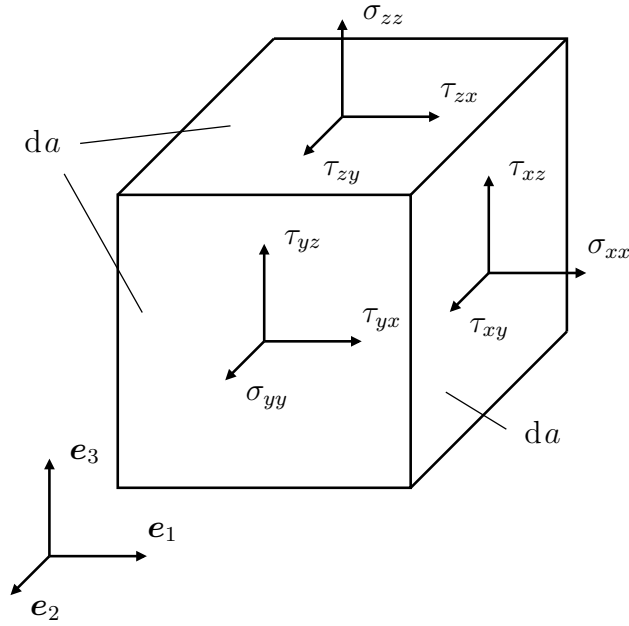


Figure 3.1: External positive quantities are shown, namely the normal stresses σ_{ij} , $i = j$ and shear stresses τ_{ij} , $i \neq j$, with $i, j \in \{1, 2, 3\}$. To achieve a clear arrangement the negative quantities have been omitted.

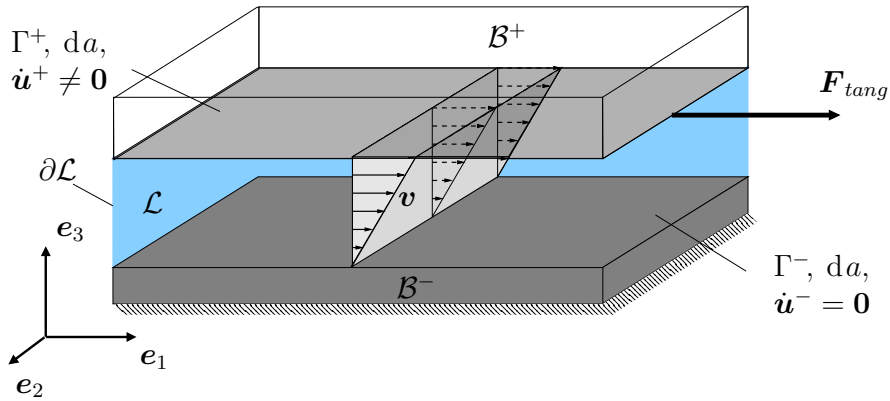


Figure 3.2: Fluid velocity profile $\mathbf{v}(z)$ between two plates under relative translational motion caused by a force $\mathbf{F}_{tang} \propto \boldsymbol{\tau}$.

components σ_{33} couple the fluid to the boundaries of the adjacent solid bodies (\mathcal{B}^+

and \mathcal{B}^-). The netforce the fluid applies equals

$$\mathbf{F}_{norm} = - \int_{\Gamma^+} \sigma_{33} \mathbf{n}^+ da - \int_{\Gamma^-} \sigma_{33} \mathbf{n}^- da, \quad (3.6)$$

where $(\bullet)^+$ and $(\bullet)^-$ denote that quantities belong to the positive or negative surfaces, respectively. Assuming an incompressible fluid [tab 3.1(iv)] the normal stress components equal the hydrostatic fluid pressure

$$\sigma_{ii} = -p \quad (\text{no sum}). \quad (3.7)$$

The solid body boundaries, its normals and velocities are denoted by Γ , \mathbf{n} and $\dot{\mathbf{u}}$, respectively, while the lubrication domain and its in/out flow boundaries are denoted via \mathcal{L} and $\partial\mathcal{L}$. Since the lubrication domain \mathcal{L} shares the same boundary with either the upper solid \mathcal{B}^+ or lower solid \mathcal{B}^- the solid boundary notation is adopted $\Gamma^{+/-}$ for the fluid. The fluid velocity is denoted by \mathbf{v} . Shear stresses $\boldsymbol{\tau}$ acting in-plane direction cause deviatoric distortions of the fluid. From angular momentum balance [eqn (2.37)] it follows that CAUCHY stress tensor is symmetric and hence

$$\boldsymbol{\tau}_{12} = \boldsymbol{\tau}_{21}, \quad \boldsymbol{\tau}_{13} = \boldsymbol{\tau}_{31}, \quad \boldsymbol{\tau}_{23} = \boldsymbol{\tau}_{32}, \quad (3.8)$$

holds. **Newton's postulate** relates shear stresses $\boldsymbol{\tau}$ to the fluid velocity profile (or *velocity gradient*) $\text{grad}[\mathbf{v}]$ via the fluid absolute viscosity μ . For water the absolute viscosity $\mu := \frac{\boldsymbol{\tau}}{\text{grad}[\mathbf{v}]}$ [Ns/m²] is a proportionality constant leading to a linear velocity profile between adjacent surfaces. Such a fluid is referred to as a **NEWTONIAN** fluid, cf. tab 3.1(iii). However in general $\mu(p)$ is not a constant in lubrication models, but a function of the pressure.

Since the CAUCHY stress tensor is symmetric, $\text{grad}[\mathbf{v}]$ may be replaced by its symmetric part \mathbf{d} . Postulating that no fluid flows across the channel ($v_3 = 0$) exists (tab 3.1(ii)) we obtain

$$\begin{aligned} \boldsymbol{\tau}_{31} &= \mu \left(\frac{\partial v_1}{\partial x_3} + \frac{\partial v_3}{\partial x_1} \right), \\ \boldsymbol{\tau}_{32} &= \mu \left(\frac{\partial v_2}{\partial x_3} + \frac{\partial v_3}{\partial x_2} \right), \end{aligned} \quad (3.9)$$

where solely velocity derivatives $\frac{\partial v_i}{\partial x_3}$ across the fluid flow remain. In order to show that the remaining shear component is negligible

$$\boldsymbol{\tau}_{21} = \mu \underbrace{\left(\frac{\partial v_1}{\partial x_2} + \frac{\partial v_2}{\partial x_1} \right)}_{\mathbf{d}} \approx 0, \quad (3.10)$$

a comparison of the velocity derivatives ($\text{grad}[\mathbf{v}] = \frac{\partial v_i}{\partial x_i}$) along and across the fluid flow is mandatory

$$\begin{aligned} \frac{\partial v_i}{\partial x_i} = \mathcal{O}\left(\frac{v_i^c}{l_i^c}\right), \quad \frac{\partial v_i}{\partial x_3} = \mathcal{O}\left(\frac{v_i^c}{h}\right) &\xRightarrow{h^c \ll l_i^c} \frac{\partial v_i}{\partial x_i} \ll \frac{\partial v_i}{\partial x_3}, \quad i \in \{1, 2\} \\ \frac{\partial^2 v_i}{\partial x_i^2} = \mathcal{O}\left(\frac{v_i^c}{[l_i^c]^2}\right), \quad \frac{\partial^2 v_i}{\partial x_3^2} = \mathcal{O}\left(\frac{v_i^c}{[h^c]^2}\right) &\xRightarrow{[h^c]^2 \ll [l_i^c]^2} \frac{\partial^2 v_i}{\partial x_i^2} \ll \frac{\partial^2 v_i}{\partial x_3^2} \end{aligned} \quad (3.11)$$

and shows that components along the fluid flow are negligible in case of a thin channelled flow $h^c \ll l^c$. Here characteristic quantities¹ are denoted by superscript c , the index $i \in 1, 2, 3$ denotes directions x, y, z of a Cartesian bases system. Further on l_i^c denotes the characteristic length $i \in \{1, 2\}$ of the flow problem, whereas $l_3^c = h^c$ denoted the gap height. Also the 2nd derivative in equation (3.11) $\frac{\partial^2 v_i}{\partial x_3^2}$ can not be omitted.

Momentum balance

If the above stated criteria are fulfilled we may use the linear momentum balance equation (2.33) and neglect *inertia* $\rho \dot{\mathbf{u}}$ and *body forces* \mathbf{b}

$$\text{div}[\boldsymbol{\sigma}] + \boldsymbol{\mathcal{B}} - \rho \boldsymbol{v} = 0 \quad (3.12)$$

Simply the surface stresses ([eqs (3.7) and (3.9)]) must be introduced into equation (3.12) for $i \in 1, 2$ directions to obtain the well-known reynolds equation

$$\frac{\partial \sigma_{ii}}{\partial x_i} + \frac{\partial \tau_{3i}}{\partial x_3} = -\frac{\partial p}{\partial x_i} + \frac{\partial}{\partial x_3} \left(\mu \frac{\partial v_i}{\partial x_3} \right) = 0 \quad (3.13)$$

Whereas $\frac{\partial \sigma_{33}}{\partial x_3} = 0$ by virtue of assumption tab 3.1_(vi) ($v_3 \approx 0$). Subsequently integrating the equation twice w.r.t. x_3 gives

$$v_i = \frac{x_3^2}{2\mu} \frac{\partial p}{\partial x_i} + \frac{\tilde{A} x_3}{\mu} + \tilde{B} \leftarrow \begin{cases} \overbrace{x_3^- = 0, v_i = \dot{u}_i^-}^{\text{no-slip bc (tab 3.1(vii))}} \\ x_3^+ = h, v_i = \dot{u}_i^+ \end{cases} \quad (3.14)$$

where \tilde{A}, \tilde{B} are integration constants which can be evaluated for the upper \bullet^+ and lower \bullet^- surfaces:

$$\begin{aligned} \dot{u}_i^- &= \frac{x_3^2}{2\mu} \frac{\partial p}{\partial x_i} + \frac{\tilde{A} x_3}{\mu} + \tilde{B} \quad \Leftrightarrow \quad \tilde{B} = \dot{u}_i^- \\ \dot{u}_i^+ &= \frac{h^2}{2\mu} \frac{\partial p}{\partial x_i} + \frac{\tilde{A} h}{\mu} + \dot{u}_i^- \quad \Leftrightarrow \quad \tilde{A} = \frac{\mu}{h} \left[\dot{u}_i^+ - \dot{u}_i^- - \frac{h^2}{2\mu} \frac{\partial p}{\partial x_i} \right]. \end{aligned} \quad (3.15)$$

¹An expection to this notation is the COUETTE flux \mathbf{q}^c .

Inserting \tilde{A}, \tilde{B} into equation (3.13) gives

$$v_i = \left[\frac{(x_3^2 - x_3 h)}{2\mu} \frac{\partial p}{\partial x_i} + \frac{x_3}{h} \dot{u}_i^+ + \dot{u}_i^- \left(\frac{h - x_3}{h} \right) \right] \quad (3.16)$$

stating the *fluid velocity* w.r.t. $i \in 1, 2$ directions. Equation 3.16 has to satisfy the mass balance.

Mass balance

Integrating equation (2.20) w.r.t. the height reads

$$0 = \int_0^h (\dot{\rho} + \text{div}[\rho \mathbf{v}]) dz, \quad (3.17)$$

where ρ represents a mean density across the height (tab 3.1_(viii)) and $\text{div}[\bullet]$ operates in the plane of flow [eqn (3.16)]. Assuming incompressibility (tab 3.1_(iv)) cancels $\dot{\rho}$ in above equation. If we now apply

$$\int_0^h \frac{\partial}{\partial \mathbf{x}} [f(x, y, z)] dz = -f(x, y, h) \frac{\partial h}{\partial \mathbf{x}} + \frac{\partial}{\partial \mathbf{x}} \left(\int_0^h [f(x, y, z)] dz \right) \quad (3.18)$$

on the divergence term in equation (3.17), we obtain

$$\begin{aligned} \int_0^h \text{div}[\rho \mathbf{v}] dz &= -(\rho v_i)_{z=h} \frac{\partial h}{\partial x_i} + \frac{\partial}{\partial x_i} \rho \left(\int_0^h v_i dz \right) + \int_0^h \rho v_3 dz, \quad i \in 1, 2 \\ &= -\rho \dot{u}_i^+ \frac{\partial h}{\partial x_i} + \frac{\partial}{\partial x_i} \rho \left(\int_0^h v_i dz \right) + \rho (v_3^+ - v_3^-), \end{aligned} \quad (3.19)$$

with

$$\rho v_3^+ = \rho \frac{dh}{dt} = h \frac{d\rho}{dt} \quad \text{and} \quad v_3^- = 0 \quad (3.20)$$

Here v_3^+ and $h\dot{\rho}$ in the next equation cancel by virtue of a static problem, yielding

$$0 = \cancel{h\dot{\rho}} - \cancel{\rho \dot{u}_i^+} \frac{\partial h}{\partial x_i} + \text{div} \left[\underbrace{\int_0^h \rho v_i dz}_{q_i} \right] \quad i \in 1, 2. \quad (3.21)$$

Since the upper surface is flat and the lower surface rough and stationary, we assume the change of gap height (along the x and y directions) is negligible, such that the 2nd term in above equation drops. Now, $\dot{\mathbf{m}}$ and \mathbf{q} denote the mass flow rate and fluid flux, respectively. Consequently one obtains the a balance law for \mathbf{q}

$$\operatorname{div}[\mathbf{q}] = 0, \quad (3.22)$$

where using equation (3.16)

$$\begin{aligned} q_i = \frac{\dot{m}_i}{\rho} &= \int_0^h h^3 \left(\frac{1}{3} - \frac{1}{2} \right) \frac{1}{2\mu} \frac{\partial p}{\partial x_i} + \frac{\dot{u}_i^+ h}{2} + \frac{\dot{u}_i^- h}{2} dz \\ &= -\frac{h^3}{12\mu} \underbrace{\frac{\partial p}{\partial x_i}}_{=:g_i} + \underbrace{\left(\frac{\dot{u}_i^+ + \dot{u}_i^-}{2} \right)}_{=: \dot{u}_i^r} h \quad \begin{array}{l} \nearrow \\ 0 \leftarrow \mathcal{B}^- \text{ fixed to } \dot{u}_i^- = 0 \end{array} \\ &= -\underbrace{\frac{h^3}{12\mu} g_i}_{q_i^p} + \underbrace{\dot{u}_i^r h}_{q_i^c} \implies \boxed{\mathbf{q} = -\frac{h^3}{12\mu} \mathbf{g} + \dot{\mathbf{u}}^r h}. \end{aligned} \quad (3.23)$$

The mass balance [eqn (3.22)] and REYNOLDS equation 3.23 will be the starting point of the Lubrication Finite Element Framework discussed in chapter 5.

Cavitation constraint

Experiments have shown, that fluids are not able to carry significant tensile forces which is manifested by the effect of cavitation, meaning that air saturated in the water dispenses and bubbles form, which leads to a loss of load carrying capacity. It occurs when the pressure inside the fluid drops below the ambient (or saturated gaseous) pressure of the fluid. Within a journal bearing this happens in stream direction shortly behind the smallest gap for diverging surfaces. The above introduced REYNOLDS equation assumes the so called SOMMERFELD condition where the diverging region is fully occupied by the lubricant which leads to sub ambient pressure and therefore an unphysical situation. In order to encompass the real physics of lubricants a couple of cavitation algorithms have been suggested in literature [73]. The GÜMBEL (or half SOMMERFELD) condition simply neglects the sub-ambient pressures but does not ensure mass conservation. In order to satisfy mass conservation the SWIFT-STIEBER condition was introduced reading

$$p \stackrel{!}{=} p^{amb}, \quad \mathbf{g} \stackrel{!}{=} 0 \quad (3.24)$$

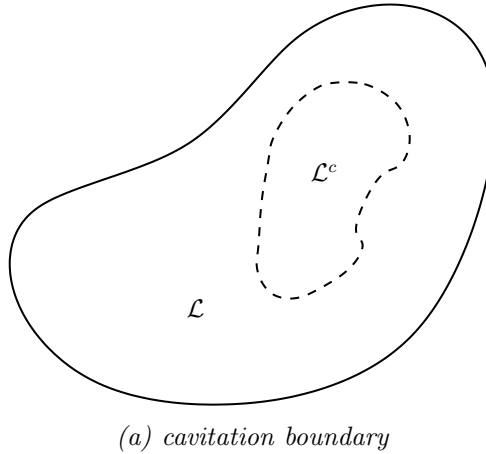


Figure 3.3: Cavitation region \mathcal{L}^c in a fluid domain \mathcal{L} .

on the cavitation boundary, see figure 3.3. This is the most commonly used constraint due to its good agreement with experimental results and robustness in numerical applications. Nonetheless the exact lubrication physics allowing sub cavitation regions – which have been observed in experiments – are captured by FLOBERG (or COYEN - ELROD) condition [Elrod [29]], but cause some numerical hassle. Qualitative pressure distributions of the SWIFT-STIEBER and FLOBERG conditions are shown in figure 3.4. In order to circumvent numerical problems and due to its wide acceptance the SWIFT-STIEBER condition is chosen in order to represent cavitation, cf. Szeri [73], Yang and Laursen [86]. Furthermore this condition is easy to implement in terms of a constraint formulation where only the pressure needs to be penalized and the pressure gradient is automatically zero (cf. equation (3.23)).

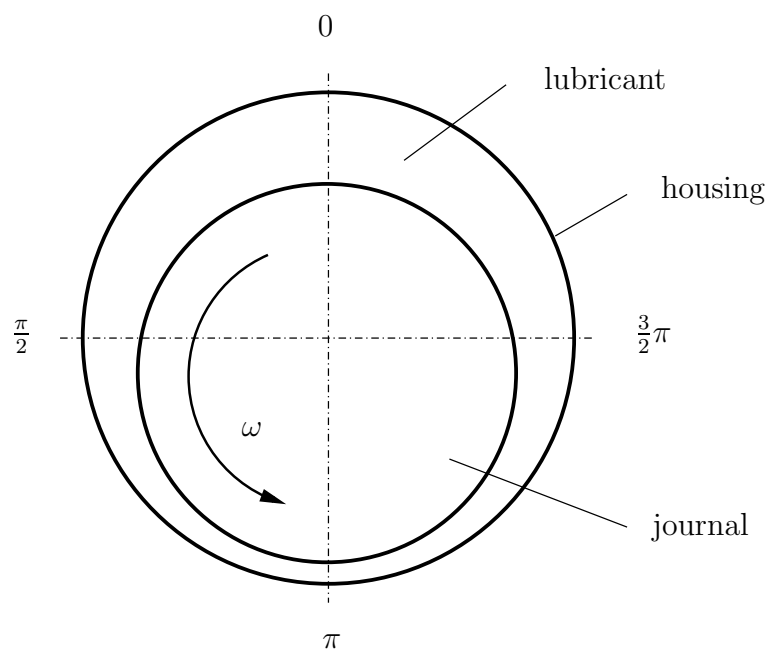
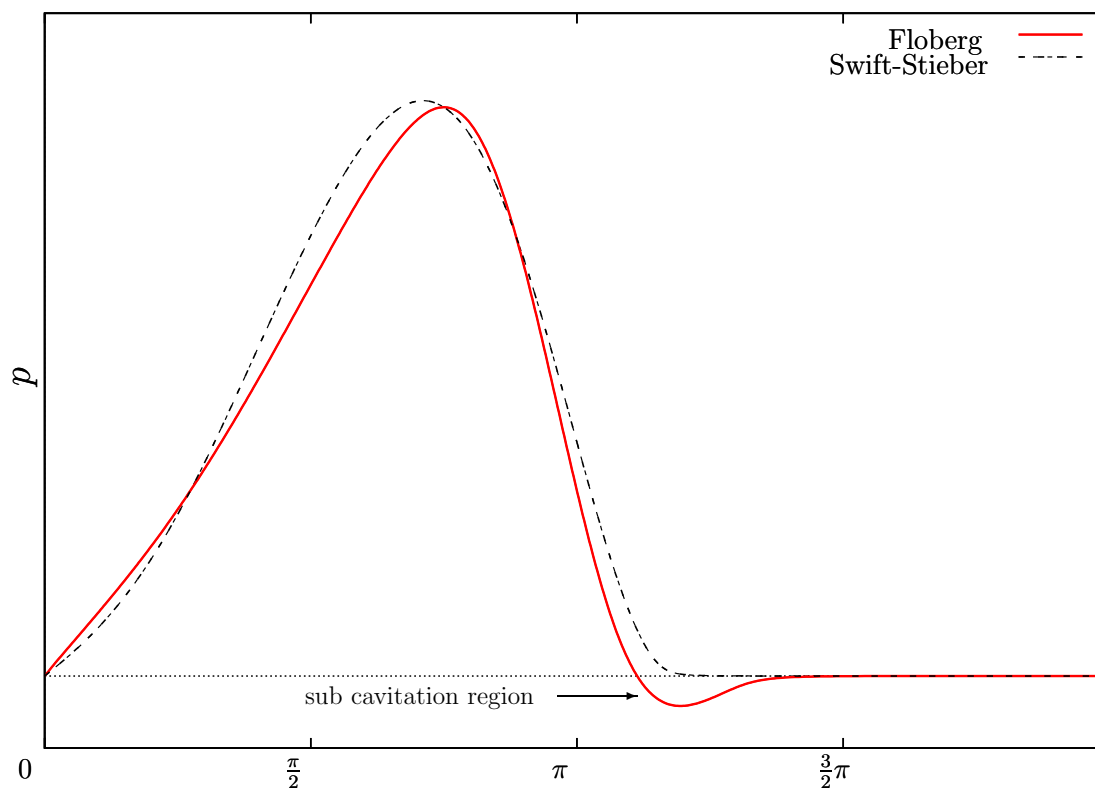
(a) *eccentric journal in housing*(b) *pressure plot*

Figure 3.4: Qualitative pressure plots for a journal bearing subject to Floberg and Swift-Stieber cavitation constraint conditions.

Chapter 4

Finite element method

In order to solve the **Boundary Value Problem** for a solid type mechanical problem

$$\text{static} \left\{ \begin{array}{ll} \text{subject to} & \text{div}[\boldsymbol{\sigma}] + \mathbf{b} = 0 \\ \text{and} & \mathbf{u} = \bar{\mathbf{u}} \\ & \mathbf{t} = \boldsymbol{\sigma} \cdot \mathbf{n} = \bar{\mathbf{t}} \end{array} \right. \begin{array}{l} , \text{ in } \Omega \\ , \text{ on } \Gamma^u \\ , \text{ on } \Gamma^\sigma \end{array} \} \text{(BC)} \quad (4.1)$$

previously derived constitutive equation for a hyper-elastic material must be introduced [eqn (2.74)]. Further on additional information are needed and hence prescribed by **boundary conditions** (BC). In case of a **static** computation the problem is time-independent. Further the surface Γ is subdivided into a **displacement boundary** Γ^u (or **Dirichlet boundary**) and a **traction boundary** Γ^σ (or **Neumann boundary**) satisfying $\Gamma^u \cup \Gamma^\sigma = \Gamma$ and $\Gamma^u \cap \Gamma^\sigma = \emptyset$, stating that the Dirichlet or Neumann boundary conditions must be prescribed on every point Γ , cf. figure 4.1. Above **BVP** is stated in its **strong form** meaning that a solution consists of every point $\mathbf{x} \in \Omega$ which allows an analytical solution for just a few restricted problems. However reformulating these equations via **variational principles**¹ is discussed in section 4.1 and delivers the so called **weak form**, where the solution is obtained as an integral average over the entire domain Ω . Furthermore, applying the **finite element method** extends the applicability to a multitude of problems and will be elucidated in the subsequent sections.

4.1 Variational formulation

Basis of **virtual work principles** are balance equations, like above stated set of equations (4.1). Subsequently scalar multiplying equation (4.1)₁ by a vector valued

¹Reduces the order of shapefunctions.

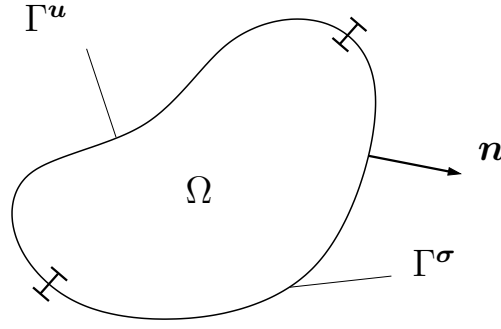


Figure 4.1: Disjoint surface classification for the solid problem into either displacement boundary Γ^u or a traction boundary Γ^σ , where \mathbf{n} denotes the surface normal on the current configuration.

test function (or **weighting function**) $\hat{\boldsymbol{\eta}}$ (with $\hat{\boldsymbol{\eta}} = 0$ on Γ^u) and integrating over the entire domain Ω leads to the weighted residual Form:

$$\begin{aligned} \mathcal{F}(\mathbf{u}, \hat{\boldsymbol{\eta}}) &= \int_{\Omega_t} (\text{div}[\boldsymbol{\sigma}] + \mathbf{b}) \cdot \hat{\boldsymbol{\eta}} \, d\nu = 0 \quad , \text{ in } \Omega \\ \text{subject to} \quad &\mathbf{u} = \bar{\mathbf{u}}, \quad \hat{\boldsymbol{\eta}} = 0 \quad , \text{ on } \Gamma^u \\ \text{and} \quad &\mathbf{t} = \boldsymbol{\sigma} \cdot \mathbf{n} = \bar{\mathbf{t}} \quad , \text{ on } \Gamma^\sigma \quad , \end{aligned} \quad (4.2)$$

stated in current configuration. Applying integration-by-parts and divergence theorem leads to

$$\int_{\Gamma} (\boldsymbol{\sigma} \cdot \mathbf{n}) \cdot \hat{\boldsymbol{\eta}} \, da - \int_{\Omega_t} \boldsymbol{\sigma} : \text{grad}[\hat{\boldsymbol{\eta}}] \, d\nu + \int_{\Omega_t} \mathbf{b} \cdot \hat{\boldsymbol{\eta}} \, d\nu = 0 \quad , \quad (4.3)$$

by making use of CAUCHY *theorem* [eqn (2.28)]. Besides the symmetry of CAUCHY stress tensor we may use the symmetric part of $\text{grad}[\hat{\boldsymbol{\eta}}]$ such that the former equation reads

$$\begin{aligned} \int_{\Gamma^\sigma} \mathbf{t} \cdot \hat{\boldsymbol{\eta}} \, da + \int_{\Gamma^u} \mathbf{t} \cdot \hat{\boldsymbol{\eta}} \, da - \int_{\Omega_t} \boldsymbol{\sigma} : \text{grad}^{sym}[\hat{\boldsymbol{\eta}}] \, d\nu + \int_{\Omega_t} \mathbf{b} \cdot \hat{\boldsymbol{\eta}} \, d\nu &= 0 \\ &\quad \nearrow 0, \text{ via (4.2)}_2 \\ \int_{\Gamma^\sigma} \mathbf{t} \cdot \hat{\boldsymbol{\eta}} \, da + \int_{\Omega_t} \mathbf{b} \cdot \hat{\boldsymbol{\eta}} \, d\nu - \int_{\Omega_t} \boldsymbol{\sigma} : \text{grad}^{sym}[\hat{\boldsymbol{\eta}}] \, d\nu &= 0 \quad . \end{aligned} \quad (4.4)$$

This equation is referred to as *the principle of virtual work*, due to equivalence with the *mechanical power* [eqn (2.46)]. In order to omit rigid body motions *displacement* (or *essential*) boundary conditions on Γ^u are mandatory, however *traction* (or *natural*) boundary conditions on Γ^σ are not obligatory.

4.2 Linearization

In general most physical behavior is subject to nonlinear relations as it can be observed for former derived constitutive equations. Both solid and lubrication constitutive equations depend non-linearly on \mathbf{u} . Further, the lubricant depends on the pressure p . Those nonlinear problems can be solved by use of iterative solution procedures like the **Newton-Raphson** algorithm (fig 4.6) resting upon a Taylor expansion of a C^1 -continuous equation $\mathcal{F}(\mathbf{u})$ writing

$$\mathcal{L}_{\mathcal{F}} = \mathcal{F}(\hat{\mathbf{u}} + \Delta\mathbf{u}) = \mathcal{F}(\hat{\mathbf{u}}) + \Delta\mathcal{F}(\hat{\mathbf{u}}, \Delta\mathbf{u}) + \mathbf{R} = 0, \quad (4.5)$$

where $\Delta\mathcal{F}(\hat{\mathbf{u}}, \Delta\mathbf{u})$ denotes the linear incremental growth at a position $\mathcal{F}(\hat{\mathbf{u}})$ and \mathbf{R} denotes the residual, measuring the error from the exact solution, cf (fig 4.2). In order to afford a solution $\Delta\mathcal{F}(\hat{\mathbf{u}}, \Delta\mathbf{u})$, $\mathcal{F}(\hat{\mathbf{u}})$ must be linearized according to

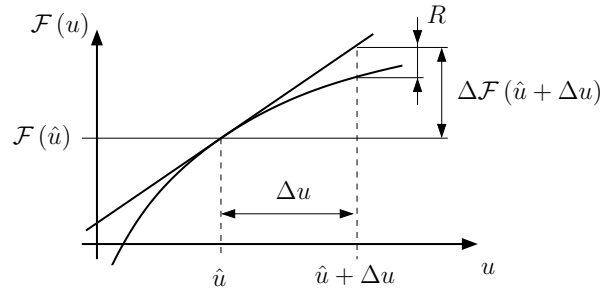


Figure 4.2: Diagram of the linearisation procedure at a fixed time t for a function $\mathcal{F}(u)$ depending on a scalar variable u .

Gateaux's derivative:

$$\Delta\mathcal{F}(\hat{\mathbf{u}}, \Delta\mathbf{u}) = \left. \frac{d\mathcal{F}(\hat{\mathbf{u}} + \gamma\Delta\mathbf{u})}{d\gamma} \right|_{\gamma=0}. \quad (4.6)$$

In equation (4.4) CAUCHY stress $\boldsymbol{\sigma}$ depends on \mathbf{u} such that we must linearize the third term. Rearranging equation (4.4) and expressing it in terms of 2nd PIOLA-KIRCHHOFF stress tensor via equations (2.3) and (2.50) leads to

$$\underbrace{\int_{\Omega_0} \delta\mathbf{E} : \mathbf{S} \, d\mathcal{V} - \int_{\Omega_0} \hat{\boldsymbol{\eta}} \cdot \mathbf{B} \, d\mathcal{V} - \int_{\Gamma_0^\sigma} \hat{\boldsymbol{\eta}} \cdot \mathbf{T} \, dA}_{\mathcal{F}(\mathbf{u})} + \underbrace{\int_{\Omega_0} (\delta\mathbf{E} : \Delta\mathbf{S} + \Delta\delta\mathbf{E} : \mathbf{S}) \, d\mathcal{V}}_{\Delta\mathcal{F}(\mathbf{u}, \Delta\mathbf{u})} = 0, \quad (4.7)$$

with

$$\begin{aligned} \text{grad}[\widehat{\boldsymbol{\eta}}] &= \text{Grad}[\widehat{\boldsymbol{\eta}}] \mathbf{F}^{-1} = \boldsymbol{\delta} \mathbf{F} \mathbf{F}^{-1}, & \boldsymbol{\delta} \mathbf{E} &= \frac{1}{2} (\mathbf{F}^T \boldsymbol{\delta} \mathbf{F} + \boldsymbol{\delta} \mathbf{F} \mathbf{F}^T) \stackrel{\mathbf{S}=\mathbf{S}^T}{=} \mathbf{F}^T \boldsymbol{\delta} \mathbf{F}, \\ \text{grad}[\Delta \mathbf{u}] &= \text{Grad}[\Delta \mathbf{u}] \mathbf{F}^{-1} = \Delta \mathbf{F} \mathbf{F}^{-1} & \text{and} & \quad \Delta \boldsymbol{\delta} \mathbf{E} = \Delta \mathbf{F}^T \boldsymbol{\delta} \mathbf{F}. \end{aligned} \quad (4.8)$$

The variation of the *Green-Lagrange* strain tensor can be simplified as $\boldsymbol{\delta} \mathbf{E} = \mathbf{F}^T \boldsymbol{\delta} \mathbf{F}$ in case of scalar product with the symmetric tensor \mathbf{S} . Furthermore the 2nd PIOLA-KIRCHHOFF stress needs to be linearized with respect to \mathbf{u}

$$\Delta \mathbf{S}(\mathbf{u} + \Delta \mathbf{u}) = \left. \frac{d\Delta \mathbf{S}(\mathbf{u} + \gamma \Delta \mathbf{u})}{d\gamma} \right|_{\gamma=0} = \frac{\partial \mathbf{S}}{\partial \mathbf{E}} \frac{\partial \mathbf{E}}{\partial \mathbf{u}} \Delta \mathbf{u} = \mathbb{C} : \Delta \mathbf{E}, \quad (4.9)$$

where $\frac{\partial \mathbf{S}}{\partial \mathbf{E}} = \mathbb{C}$ [eqn (2.68)] denotes the spacial linear elasticity tensor and \mathbf{E} denotes the GREEN-LAGRANGE strain tensor referring to the material description. However if \mathbb{C} and $\frac{\partial \mathbf{E}}{\partial \mathbf{u}}$ prescribe nonlinear behavior we identify these terms as representing **material** and **geometric nonlinearity**, respectively.

Linearizing the symmetric GREEN-LAGRANGE tensor [eqn (2.11)] leads to

$$\Delta \mathbf{E} = \frac{1}{2} (\mathbf{F}^T \Delta \mathbf{F} + \Delta \mathbf{F} \mathbf{F}^T) \stackrel{\mathbf{S}=\mathbf{S}^T}{=} \mathbf{F}^T \Delta \mathbf{F}. \quad (4.10)$$

Since we want to express equation (4.7) with respect to the current configuration, $\mathbf{S}, \boldsymbol{\delta} \mathbf{E}, \Delta \boldsymbol{\delta} \mathbf{E}$ and $\Delta \mathbf{S}$ need to be transformed to the current configuration via equations (2.3) and (2.50),

$$\boldsymbol{\delta} \mathbf{e} := \mathbf{F}^{-T} \boldsymbol{\delta} (\mathbf{F}^T \mathbf{e} \mathbf{F}) \mathbf{F}^{-1} = \mathbf{F}^{-T} \boldsymbol{\delta} \mathbf{E} \mathbf{F}^{-1}, \quad (4.11)$$

and

$$\Delta \boldsymbol{\delta} \mathbf{e} := \mathbf{F}^{-T} \Delta (\mathbf{F}^T \boldsymbol{\delta} \mathbf{e} \mathbf{F}) \mathbf{F}^{-1} = \mathbf{F}^{-T} \Delta \boldsymbol{\delta} \mathbf{E} \mathbf{F}^{-1}, \quad (4.12)$$

respectively.

The push-forward of $\Delta \mathbf{S}$ defines

$$\Delta \boldsymbol{\tau} := \mathbf{F} (\Delta \mathbf{S}) \mathbf{F}^T = \mathbf{F} (\mathbb{C} : \Delta \mathbf{E}) \mathbf{F}^T = J \boldsymbol{\alpha} : \text{grad}[\Delta \mathbf{u}], \quad (4.13)$$

while making use of equations (4.9), (4.10) and

$$\begin{aligned} \mathbf{F} (\mathbb{C} : \Delta \mathbf{E}) \mathbf{F}^T &= F_{aA} \mathbb{C}_{ABCD} F_{cC} \frac{\partial u_c}{\partial x_d} F_{dD} \\ &= J \boldsymbol{\alpha}_{abcd} \frac{\partial u_c}{\partial x_d} \\ &= J \boldsymbol{\alpha} : \text{grad}[\Delta \mathbf{u}]. \end{aligned} \quad (4.14)$$

Changing the configuration of $\Delta\boldsymbol{\tau}$ [eqn (4.13)] via equations (2.3) and (2.50) yields

$$\Delta\boldsymbol{\sigma} = \boldsymbol{\varepsilon} : \text{grad}[\Delta\mathbf{u}] , \quad (4.15)$$

such that the linearized virtual work [eqn (4.7)] transforms to

$$\begin{aligned} & \int_{\Gamma^\sigma} \widehat{\boldsymbol{\eta}} \cdot \mathbf{t} \, da + \int_{\Omega_t} \widehat{\boldsymbol{\eta}} \cdot \mathbf{b} \, dv - \int_{\Omega_t} \text{grad}[\widehat{\boldsymbol{\eta}}] : \boldsymbol{\sigma} \, dv \\ & + \underbrace{\int_{\Omega_t} (\text{grad}[\widehat{\boldsymbol{\eta}}] : \text{grad}[\Delta\mathbf{u}] \boldsymbol{\sigma} + \text{grad}[\widehat{\boldsymbol{\eta}}] : \boldsymbol{\varepsilon} : \text{grad}[\Delta\mathbf{u}]) \, dv}_{\Delta\mathcal{F}(\mathbf{u}, \Delta\mathbf{u})} = 0 . \end{aligned} \quad (4.16)$$

4.3 Discretization

Due to the fact that the linearized form of the variational formulation can't be solved analytically we discretize the domain Ω into n_e **finite elements** Ω_e (see figure 4.3):

$$\begin{aligned} \Omega & \approx \bigcup_{e=1}^{n_e} \Omega_e \\ \int_{\Omega_t} f(\mathbf{X}) \, dv & \approx \bigcup_{e=1}^{n_e} \int_{\Omega_e} f(\mathbf{X}) \, dv . \end{aligned} \quad (4.17)$$

The displacements \mathbf{u} and the variation $\widehat{\boldsymbol{\eta}}$ inherit the same discretization. Within any finite element n Ansatz-functions are used to interpolate them from their nodal valued \mathbf{u}_I and $\widehat{\boldsymbol{\eta}}_I$ via

$$\begin{aligned} \mathbf{u} & \approx \sum_I^n N_I \mathbf{u}_I \quad , \quad \boldsymbol{\eta} \approx \sum_I^n N_I \boldsymbol{\eta}_I \\ \mathbf{u}_{,X} & \approx \sum_I^n N_{I,X} \mathbf{u}_I \quad , \quad \mathbf{u}_{,x} \approx \sum_I^n N_{I,x} \mathbf{u}_I . \end{aligned} \quad (4.18)$$

In order to reduce computational costs, the Ansatz-functions N_I and its derivatives in initial configuration $N_{I,X}$ and current configuration $N_{I,x}$ will be derived with respect to a new reference domain, namely the **master element**. For a one dimensional problem they write according figure 4.4, where N_I^1 denotes linear and N_I^2 quadratic order shape functions evaluated at a node I. For higher dimensional problems shape functions can be constructed via a product rule

$$2\text{D}: N_I(\xi_1, \xi_2) = N_I^1(\xi_1) N_I^2(\xi_2) , \quad 3\text{D}: N_I(\xi_1, \xi_2, \xi_3) = N_I^1(\xi_1) N_I^2(\xi_2) N_I^3(\xi_3) \quad (4.19)$$

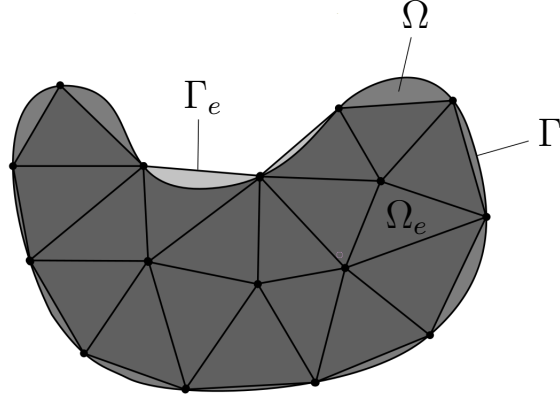


Figure 4.3: Discretization of domain Ω into finite elements Ω_e , where the boundaries are denoted by Γ and Γ_e for the real and discretized surfaces, respectively.

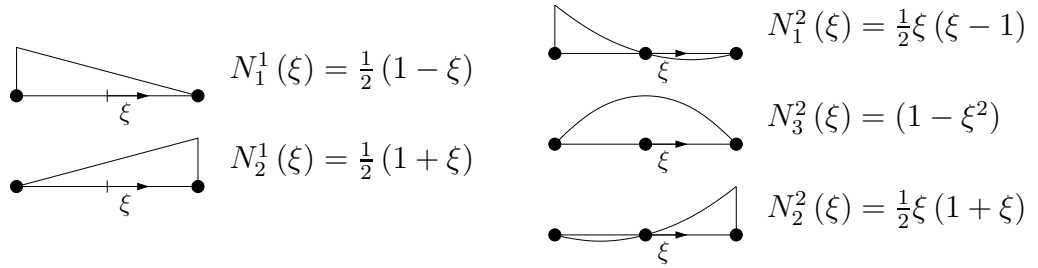


Figure 4.4: Linear order N_I^1 and quadratic order N_I^2 one dimensional shape-functions at nodes I .

However, they can be mapped to the initial and current configurations via the iso-parametric concept and its crucial operations

$$\mathbf{X} \approx \sum_I^n N_I \mathbf{X}_I \quad , \quad \mathbf{x} \approx \sum_I^n N_I \mathbf{x}_I$$

$$\mathbf{J} = \mathbf{X}_{,\xi} = \frac{d\mathbf{X}}{d\xi} \approx \sum_I^n \mathbf{X}_I \otimes \frac{\partial N_I}{\partial \xi} \quad , \quad \mathbf{j} = \mathbf{x}_{,\xi} = \frac{d\mathbf{x}}{d\xi} \approx \sum_I^n \mathbf{x}_I \otimes \frac{\partial N_I}{\partial \xi} \quad , \quad (4.20)$$

also shown in figure 4.5.

The mapping of the derivatives of the Ansatz-functions from the reference configuration to the initial ($N_{I,\mathbf{x}}$) and the current configuration ($N_{I,\mathbf{X}}$) is achieved by applying product rule. Hence we obtain the partial derivatives of ξ with respect

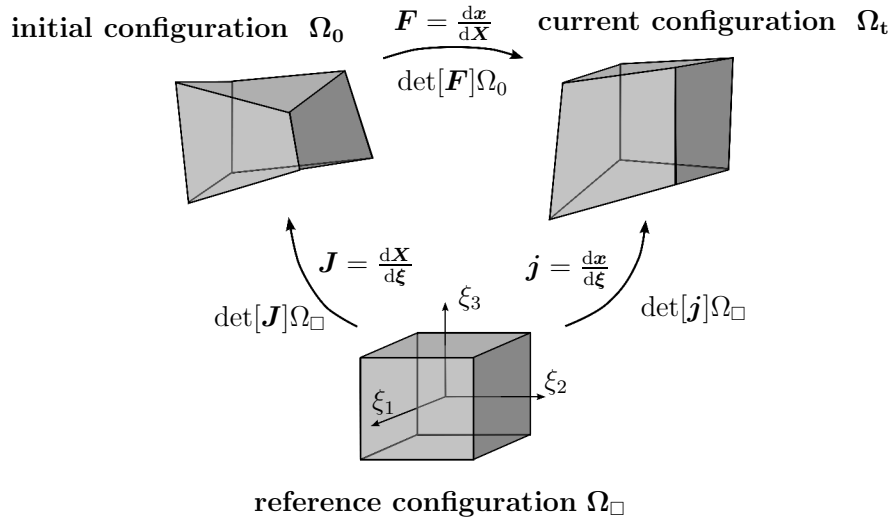


Figure 4.5: Iso-parametric concept showing the transformations between the initial configuration, current configuration and reference configuration.

to the initial and current configurations being the transpose inverse of the above defined Jacobians J and j , respectively:

$$\begin{aligned}
 N_{I,X} &= \frac{dN_I}{d\mathbf{X}} = \frac{\partial \boldsymbol{\xi}^T}{\partial \mathbf{X}} \frac{\partial N_I}{\partial \boldsymbol{\xi}} = \mathbf{J}^{-T} \frac{\partial N_I}{\partial \boldsymbol{\xi}} \\
 N_{I,x} &= \frac{dN_I}{d\mathbf{x}} = \frac{\partial \boldsymbol{\xi}^T}{\partial \mathbf{x}} \frac{\partial N_I}{\partial \boldsymbol{\xi}} = \mathbf{j}^{-T} \frac{\partial N_I}{\partial \boldsymbol{\xi}}
 \end{aligned} \tag{4.21}$$

Transforming the integration from initial or current configuration into the reference configuration reads

$$\begin{aligned}
 \int_{\Omega_e} f(\mathbf{X}) \Omega_e &= \int_{\Omega_{\square}} f(\boldsymbol{\xi}) \det[\mathbf{j}(\boldsymbol{\xi})] \Omega_{\square} \\
 &= \int_{-1}^1 \int_{-1}^1 \int_{-1}^1 f(\xi_1, \xi_2, \xi_3) \det[\mathbf{j}] d\xi_1 d\xi_2 d\xi_3 \\
 &\approx \sum_{gp=1}^{n_{gp}} f(\xi_1^{gp}, \xi_2^{gp}, \xi_3^{gp}) \det[\mathbf{j}(\xi_1^{gp}, \xi_2^{gp}, \xi_3^{gp})] w^{gp}, \tag{4.22}
 \end{aligned}$$

where the third term represents GAUSS integration scheme, approximating the analytical solution at the GAUSS points positions $(\bullet)^{gp}$ and their corresponding weightings w^{gp} .

Subsequently we rewrite [eqn (4.16)] in index notation

$$\begin{aligned}
0 &= \int_{\Gamma^\sigma} \hat{\eta}_r t_r \, da + \int_{\Omega_t} \hat{\eta}_r b_r \, dv - \int_{\Omega_t} \hat{\eta}_{r,s} \sigma_{rs} \, dv \\
&+ \int_{\Omega_t} (\hat{\eta}_{r,s} : \Delta u_{r,u} \sigma_{us} + \hat{\eta}_{r,s} : \mathcal{C}_{rstu} : \Delta u_{t,u}) \, dv
\end{aligned} \tag{4.23}$$

and discretizing leads to

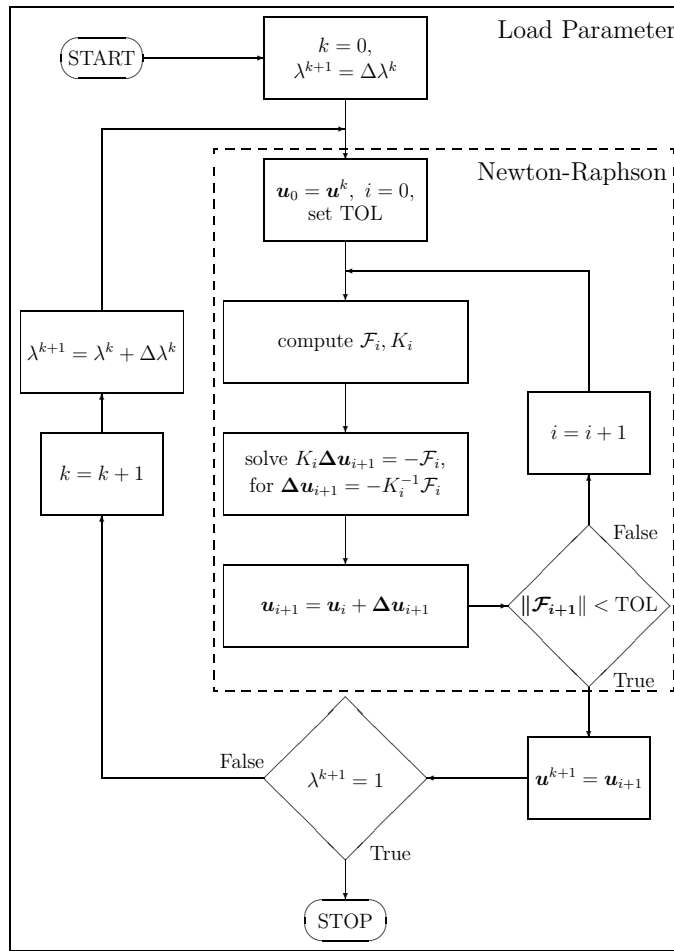
$$\begin{aligned}
0 &= \sum_J \hat{\eta}_{Jr} \left[\underbrace{\int_{\Gamma^\sigma} N_J t_r \, da + \int_{\Omega_t} N_J b_r \, dv}_{F^{ext}} - \underbrace{\int_{\Omega_t} N_{J,s} \sigma_{rs} \, dv}_{F^{int}} \right] \\
&+ \sum_J \hat{\eta}_{Jr} \sum_I \left[\underbrace{\int_{\Omega_t} (N_{J,s} N_{I,u} \delta_{rt} \sigma_{us} + N_{J,s} \mathcal{C}_{rstu} N_{I,u}) \, dv}_K \right] \Delta u_{It} \\
\Leftrightarrow \sum_J K_{IJab} \Delta u_b^J &= F_{Ia}^{ext} - F_{Ia}^{int} .
\end{aligned} \tag{4.24}$$

4.4 Solving nonlinear problems numerically

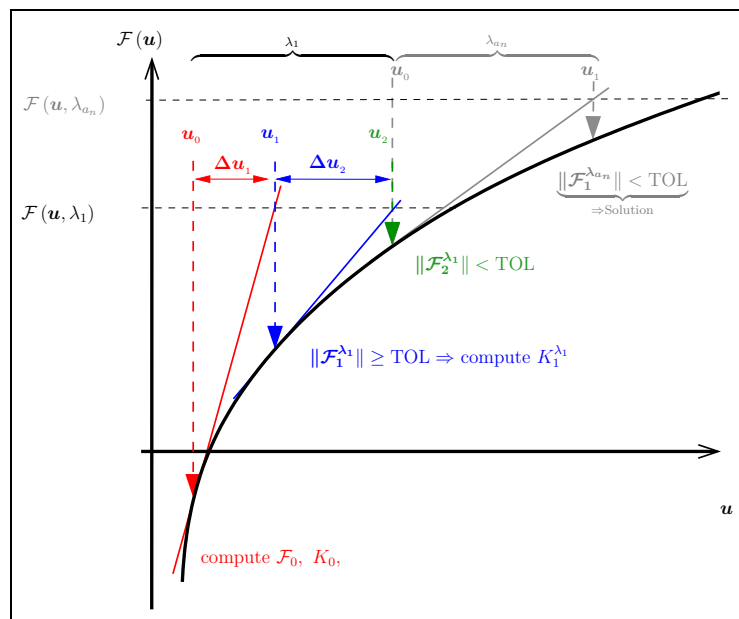
Subsequently one can solve above stated problem by applying an iterative NEWTON-RAPHSON solver which is constructed from equation (4.5)

$$\begin{aligned}
\mathcal{F}(u_{i+1}) &= \mathcal{F}(u_i) + \underbrace{\Delta \mathcal{F}(u_i)}_{=: \mathbf{K}(u_{i+1})} \Delta \mathbf{u}_n \stackrel{!}{=} 0 \\
\mathbf{K}(u_i) \Delta \mathbf{u}_{i+1} &= -\mathcal{F}(u_i) \quad \text{subject to } \|\mathcal{F}(u_{i+1})\| \stackrel{!}{=} 0 \\
&= \mathbf{F}^{ext} - \mathbf{F}^{int} ,
\end{aligned} \tag{4.25}$$

where \mathbf{F}^{ext} is controlled by a loadfactor $\lambda : 0 \rightarrow 1$. The work principle of a NEWTON-RAPHSON solver is shown in figure 4.6 for a scalar valued function.



(a) flowchart



(b) diagram

Figure 4.6: Iterative solution of Newton-Raphson algorithm with load scaling via load parameter λ .

Chapter 5

Finite element framework for elasto-hydrodynamic lubrication

In tensor notation REYNOLDS **Boundary Value Problem (BVP)** [eqs (3.22) and (3.23)] reads

$$\begin{aligned}
 & -\operatorname{div}[\mathbf{q}] = 0 && \text{in } \mathcal{L} \\
 & \mathbf{q} = \underbrace{-\frac{h^3}{12\mu}\mathbf{g}}_{\mathbf{q}^p} + \underbrace{h\dot{\mathbf{u}}^r}_{\mathbf{q}^c} \\
 & \text{subject to } && p = \hat{p} && \text{on } \partial\mathcal{L}^p \\
 & \text{and } && -\mathbf{q} \cdot \mathbf{n} := \hat{q}_n && \text{on } \partial\mathcal{L}^q,
 \end{aligned} \tag{5.1}$$

where (analogously to the solid problem, in chapter 4) the lubricant boundary $\partial\mathcal{L}$ is split into a pressure boundary $\partial\mathcal{L}^p$ and a flux boundary $\partial\mathcal{L}^q$, cf (fig 5.1). Here, the constitutive dependence $\mathbf{q} = \mathbf{q}(h, p, \mathbf{g}, \dot{\mathbf{u}}^r)$ holds where p is the fluid pressure and $\mathbf{g} = \operatorname{grad}[p]$ its surfacial gradient, evaluated in curvilinear coordinates, $\dot{\mathbf{u}}^r$ is the relative velocity between the adjacent surfaces and h is the distance between those surfaces (see also figure 7.5). For future reference, the flux has also been additively decomposed as

$$\mathbf{q} = \mathbf{q}^p + \mathbf{q}^c \tag{5.2}$$

into the POISEUILLE term \mathbf{q}^p which generally depends nonlinearly on the pressure p and the linear COUETTE term \mathbf{q}^c . Within the POISEUILLE term, a possible nonlinearity arises from the relation $\mu(p) = \mu_0 \cdot e^{\alpha p}$, namely BARUS equation holds. The dynamic viscosity μ_0 has to be chosen for an isothermal scenario at zero pressure. For water and low working pressures the pressure-viscosity coefficient α remains zero [69] (p.21, table 2.3). It is remarked that the derivation of the REYNOLDS equation was recently revisited in Rajagopal and Szeri [59] with a

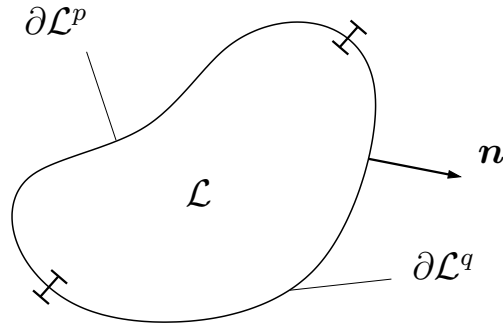


Figure 5.1: Disjoint surface classification for lubrication problem into: pressure boundary $\partial\mathcal{L}^p$ and flux boundary $\partial\mathcal{L}^q$, where \mathbf{n} denotes the surface normal on the current configuration.

pressure dependent viscosity and an augmented formulation was obtained. Nevertheless, the commonly accepted convention of employing BARUS viscosity for low working pressures in the classical equation is followed in the present work.

Since the solids are prescribed in material (or LAGRANGE) description and the fluid is given with respect to the spacial (or EULER) description¹ a mesh may be introduced with respect to the material (or LAGRANGE) description. This means that both bodies being in relative motion against another are kept fixed, whereas their relative motion $\dot{\mathbf{u}}^r$ is introduced directly to the lubrication equations COUETTE term \mathbf{q}^c , see [eqn (5.1)]. This setting is referred to as *Arbitrary Lagrangian Eulerian* description (ALE) and enables an efficient treatment of time consuming problems (e.g. solutions for high velocity $\dot{\mathbf{u}}^r$ driven flow problems). In case of transient finite deformation problems mesh distortion decreases the solution accuracy such that a mesh remapping becomes mandatory, where additional relative (or “convective”) velocity terms arise from the different flow and mesh velocities. A detailed overview of time dependent ALE-formulations covering different flow-type problems can be found in [17, 26, 38]. However in the present static problem those terms do not sprout due to a fixed lubrication domain (or mesh) in space. However a special finite element according to Curnier and Taylor [24] is introduced as shown in figure 5.2. This element consists of three adjoined surfaces, where the upper Γ^+ and lower surface Γ^- transfer the lubricant hydrostatic pressure p to the solid bodies via their normals $\mathbf{n}^{+/-}$. In contrast to the other surfaces the middle surface is fixed in displacement \mathbf{u} and stores the lubricant hydrostatic pressure in an additional degree of freedom at its nodes.

¹Fluid flows through a mesh fixed in space.

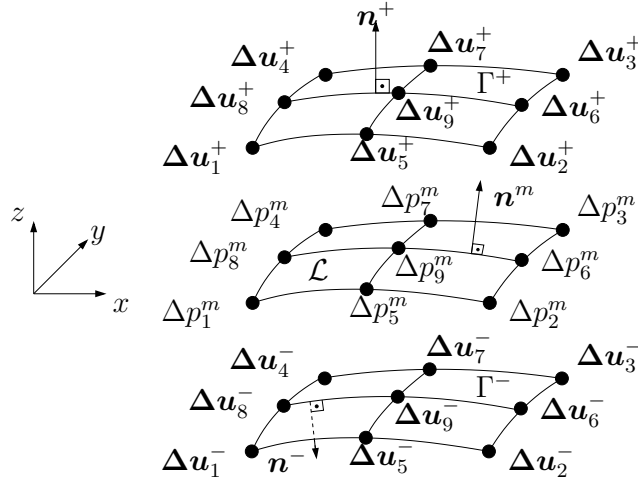


Figure 5.2: Finite element with additional middle nodes.

5.1 Variational formulation

The basis of a **variational formulation** is the above stated BVP, which is multiplied by vector valued test functions $\widehat{\boldsymbol{\eta}}^g := \text{grad}[\widehat{\eta}^p]$, $\widehat{\boldsymbol{\eta}}^u$ and a scalar test function $\widehat{\eta}^p$ leading to

$$\begin{aligned} \mathcal{F}^L(\mathbf{u}, p) = & - \underbrace{\int_{\mathcal{L}^m} \frac{h^3}{12\mu} \widehat{\boldsymbol{\eta}}^g \cdot \mathbf{g} \, da + \int_{\mathcal{L}^m} \frac{h \dot{\mathbf{u}}^r}{2} \cdot \widehat{\boldsymbol{\eta}}^g \, da + \int_{\partial \mathcal{L}^m} \widehat{q}_n \widehat{\boldsymbol{\eta}}^g \, dl}_{=: \mathcal{F}^F(\mathbf{u}, p)} \quad \begin{matrix} 0, \text{ on } \partial \mathcal{L}^p \\ \end{matrix} \quad (5.3) \\ & - \underbrace{\int_{\mathcal{L}^-} p \mathbf{n}^- \cdot \widehat{\boldsymbol{\eta}}^u \, da - \int_{\mathcal{L}^+} p \mathbf{n}^+ \cdot \widehat{\boldsymbol{\eta}}^u \, da}_{=: \mathcal{F}^C(\mathbf{u}, p)} + \underbrace{\int_{\mathcal{L}^m} \widehat{\eta}^p \in_C \{p - p^{amb}\} \, da}_{=: \mathcal{F}^{Cav}(p)}, \end{aligned}$$

where $\mu(p)$ denotes the fluid viscosity and $h(\mathbf{u})$ denotes the gap height. They read

$$\mu(p) = \mu_0 e^{\alpha p}, \quad (5.4)$$

namely BARUS equation, and

$$\begin{aligned} h(\mathbf{u}) &= (\mathbf{x}^+ + \mathbf{u}^+ - \mathbf{x}^- - \mathbf{u}^-) \cdot \mathbf{n}^m, \\ \mathbf{n}^m &= \frac{1}{\|\mathbf{X}_{,\epsilon} \times \mathbf{X}_{,\mu}\|_2} (\mathbf{X}_{,\epsilon} \times \mathbf{X}_{,\mu}), \end{aligned} \quad (5.5)$$

respectively. Here the normal vector \mathbf{n}^m is constructed on the fixed mid plane \mathcal{L} . Hence \mathbf{n}^m does not depend on displacements \mathbf{u} .

To couple the fluid's internal pressure p to the lower Γ^- and upper Γ^+ surfaces, normal vectors \mathbf{n}^- and \mathbf{n}^+ on both surfaces are introduced. The normal vectors are not normalized due to the fact that $\|\mathbf{n}^-\| = \|J\|$ such that we may write

$$\begin{aligned} \mathbf{n}^- &= - \overbrace{(\mathbf{X}^- + \mathbf{u}^-)_{,\epsilon}}^{x_{,\epsilon}^- :=} \times \overbrace{(\mathbf{X}^- + \mathbf{u}^-)_{,\mu}}^{x_{,\mu}^- :=} \\ \mathbf{n}^+ &= - \overbrace{(\mathbf{X}^+ + \mathbf{u}^+)_{,\epsilon}}^{x_{,\epsilon}^+ :=} \times \overbrace{(\mathbf{X}^+ + \mathbf{u}^+)_{,\mu}}^{x_{,\mu}^+ :=} \end{aligned} \quad (5.6)$$

5.2 Linearization

The lubrication formulation in weak form writes as $\mathcal{F}^L(\mathbf{u}, p) = \mathcal{F}^C(\mathbf{u}, p) + \mathcal{F}^F(\mathbf{u}, p)$ where $\mathcal{F}^F(\mathbf{u}, p)$ and $\mathcal{F}^C(\mathbf{u}, p)$ denote the fluid and coupling terms, respectively. Both terms are nonlinear functions of displacements \mathbf{u} and pressure p , cf. [eqn (5.3)]. In order to take into account the effect of cavitation, $\mathcal{F}^{\text{cav}}(p)$ penalizes the pressure to be larger than the ambient pressure p^{amb} . To solve this problem $\mathcal{F}^L(\mathbf{u}, p)$ must be linearized and discretized according to displacement and pressure:

$$\begin{aligned} \mathcal{L}_{\mathcal{F}^L} &:= \mathcal{F}^L(\mathbf{u}, p) + \frac{d\mathcal{F}^L}{d\mathbf{u}} \Delta \mathbf{u} + \frac{d\mathcal{F}^L}{dp} \Delta p \\ &= \left[\frac{d\mathcal{F}^F}{d\mathbf{u}} + \frac{d\mathcal{F}^C}{d\mathbf{u}} \right] \Delta \mathbf{u} + \left[\frac{d\mathcal{F}^F}{dp} + \frac{d\mathcal{F}^C}{dp} \right] \Delta p \\ &= \left[\frac{\partial \mathcal{F}^F}{\partial h} \frac{\partial h}{\partial \mathbf{u}} + \frac{\partial \mathcal{F}^C}{\partial \mathbf{n}} \frac{\partial \mathbf{n}}{\partial \mathbf{u}} \right] \Delta \mathbf{u} + \left[\frac{\partial \mathcal{F}^F}{\partial p} + \frac{\partial \mathcal{F}^F}{\partial \mu} \frac{\partial \mu}{\partial p} + \frac{\partial \mathcal{F}^C}{\partial p} \right] \Delta p \end{aligned} \quad (5.7)$$

Linearization of \mathcal{F}^L with respect to \mathbf{u}

The fluid part inherits the height which depends on \mathbf{u} . Therefore $\frac{\partial \mathcal{F}^F(\mathbf{u}, p)}{\partial \mathbf{u}} = \frac{\partial \mathcal{F}^F(\mathbf{u}, p)}{\partial h} \frac{\partial h}{\partial \mathbf{u}}$ has to be solved. Here $\frac{\partial h}{\partial \mathbf{u}}$ has to be derived separately for the upper and lower boundary. For simplicity the mid nodes are kept constant resulting in a normal vector \mathbf{n}^m which is not depending on the displacement

$$\frac{\partial \mathcal{F}^F}{\partial h} \frac{\partial h}{\partial \mathbf{u}^\pm} = \int_{\mathcal{L}^m} \overbrace{\left(\frac{3h^2}{12\mu} \hat{\boldsymbol{\eta}}^g \cdot \mathbf{g} - \dot{\mathbf{u}}^r \cdot \hat{\boldsymbol{\eta}}^g \right)}^{\frac{\partial \mathcal{F}^F}{\partial h}} \overbrace{\left(\pm \Delta \mathbf{u}^\pm \cdot \mathbf{n}^m \right)}^{\frac{\partial h}{\partial \mathbf{u}^\pm}}. \quad (5.8)$$

Evaluating the coupling part between solid and lubricant demands to consider that the normal vectors $\mathbf{n}^{-/+}$ within the contact formulations for the lower and upper

surfaces depend on displacements $\mathbf{u}^{-/+}$. And hence $\frac{\partial \mathcal{F}^C}{\partial \mathbf{n}} \frac{\partial \mathbf{n}}{\partial \mathbf{u}^-}$ and $\frac{\partial \mathcal{F}^C}{\partial \mathbf{n}} \frac{\partial \mathbf{n}}{\partial \mathbf{u}^+}$ read

$$\begin{aligned} \frac{d\mathcal{F}^C}{du_j} &= \mp \int_{\mathcal{L}^{-/+}} p \widehat{v}_i \delta_{ij} e_{jst} \left(\Delta u_{s,\epsilon}^{-/+} x_{t,\mu}^{-/+} + x_{s,\epsilon}^{-/+} \Delta u_{t,\mu}^{-/+} \right) da \\ &= \mp \int_{\mathcal{L}^{-/+}} p \widehat{v}_j \left(e_{jst} \Delta u_{s,\epsilon}^{-/+} x_{t,\mu}^{-/+} + e_{jmn} x_{m,\epsilon}^{-/+} \delta_{sn} \Delta u_{s,\mu}^{-/+} \right) da \end{aligned} \quad (5.9)$$

Linearization of \mathcal{F}^L with respect to \mathbf{p}

The fluid part assembles to

$$\begin{aligned} \frac{d\mathcal{F}^L}{dp} &= \int_{\mathcal{L}^m} \left[\overbrace{\frac{h^3}{12\mu} \widehat{\boldsymbol{\eta}}^g \cdot \text{grad}[\Delta p]}^{\frac{\partial \mathcal{F}^F}{\partial p}} - \overbrace{\frac{h^3}{12\mu^{\frac{2}{3}}} \widehat{\boldsymbol{\eta}}^g \cdot \text{grad}[p]}^{\frac{\partial \mathcal{F}^F}{\partial \mu}} \overbrace{\mu_1 \kappa \Delta p}^{\frac{\partial \mu}{\partial p}} \right] da \\ &= \int_{\mathcal{L}^m} \left[\frac{h^3}{12\mu} \widehat{\eta}_{,j}^p \underbrace{\Delta p_{,j}}_{\delta_{ij} \Delta p_{,i}} - \mu_1 \kappa \frac{h^3}{12\mu^{\frac{2}{3}}} \widehat{\eta}_{,j}^p p_{,j} \Delta p_{,i} \right] da, \end{aligned} \quad (5.10)$$

where the viscosity μ depends on the pressure. Furthermore the coupling part can be computed directly

$$\begin{aligned} \frac{\partial \mathcal{F}^C}{\partial p} &= \left[- \int_{\mathcal{L}^-} \mathbf{n}^- \cdot \widehat{\boldsymbol{\eta}}^u da - \int_{\mathcal{L}^+} \mathbf{n}^+ \cdot \widehat{\boldsymbol{\eta}}^u da \right] \Delta p \\ &= \left[- \int_{\mathcal{L}^-} n_i^- \widehat{\eta}_i^u da - \int_{\mathcal{L}^+} n_i^+ \widehat{\eta}_i^u \Delta p da \right] \end{aligned} \quad (5.11)$$

At last the cavitation constraint needs to be linearized and writes

$$\begin{aligned} \frac{d\mathcal{F}^{Cav}}{dp} &= \overbrace{\left. \frac{\partial \mathcal{F}^{Cav}(p+\gamma \Delta p)}{\partial \gamma} \right|_{\gamma=0}} \\ &= \left[- \int_{\mathcal{L}^m} \widehat{\eta}^p \epsilon_C \{(p + \gamma \Delta p) - p_a\} da \right]_{\gamma=0} \\ &= \left[- \int_{\mathcal{L}^m} \widehat{\eta}^p \epsilon_C \Delta p da \right] \end{aligned} \quad (5.12)$$

5.3 Discretization

Aiming at a numerical solution demands a discretization of the linearized elasto-hydrodynamic lubrication equations making use of the iso-parametric concept (sec

4.3), being subject to curvilinear coordinates. Similar to the solid problem [eqn (4.17)] the lubrication domain \mathcal{L} accumulates according to

$$\mathcal{L} \approx \bigcup_{e=1}^{n_e} \mathcal{L}_e$$

$$\int_{\mathcal{L}} f(\mathbf{X}) \, da \approx \bigcup_{e=1}^{n_e} \int_{\mathcal{L}_e} f(\mathbf{X}) \, d\mathcal{L}_e \quad (5.13)$$

and also GAUSS integration can be adopted. Further on quadratic shape functions for a two dimensional problem read

$$N_I(\xi_1, \xi_2) = \frac{1}{4} (\xi_1^2 + \xi_{1I}\xi_1) (\xi_2^2 + \xi_{2I}\xi_2) \leftarrow \text{Edge-Nodes:}(I=1,2,3,4)$$

$$N_I(\xi_1, \xi_2) = \frac{1}{2} \xi_{1I}^2 (\xi_1^2 + \xi_{1I}\xi_1) (1 - \xi_2^2)$$

$$+ \frac{1}{2} \xi_{2I}^2 (\xi_2^2 + \xi_{2I}\xi_2) (1 - \xi_1^2) \leftarrow \text{Mid-Nodes:}(I=5,6,7,8)$$

$$N_I(\xi, \eta) = (1 - \xi_1^2) (1 - \xi_2^2) \leftarrow \text{Center-Node:}(I=9), \quad (5.14)$$

according to figure 4.4 and equation (4.19). The node order is shown in figure 5.3.

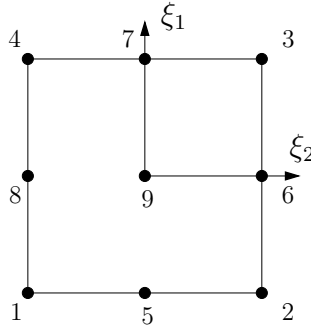


Figure 5.3: Two dimensional quadratic master element.

Local Cartesian basis

In order to prescribe a two dimensional REYNOLDS flow within a three dimensional space a special mapping of the shape functions needs to be introduced. Therefore a formulation introduced by Wagner and Gruttmann [82] for finite rotation shell-type problems is used.

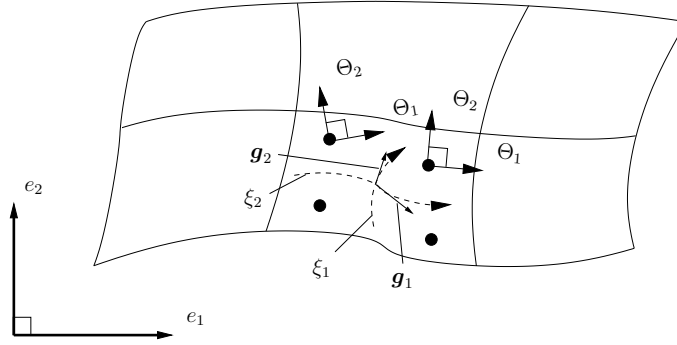


Figure 5.4: Finite rotation formulation for shell elements.

Figure 5.4 shows all quantities necessary to derive a sufficient mapping for the shape functions derivatives ($N_{I,\alpha} = J_{\alpha\beta}^{-1} N_{I,\xi\beta}$). In order to obtain the Jacobian of mapping we start with the parametrized coordinates² from which the local base vectors are computed

$$\begin{aligned}
 \mathbf{g}_1 &= \sum_{I=1}^{nel} N_{I,\xi_1} \mathbf{x}_I, \\
 \mathbf{g}_2 &= \sum_{I=1}^{nel} N_{I,\xi_2} \mathbf{x}_I, \\
 \mathbf{g}_3 &= \frac{(\mathbf{g}_1 \times \mathbf{g}_2)}{\|\mathbf{g}_1 \times \mathbf{g}_2\|_2}.
 \end{aligned} \tag{5.15}$$

Note that ($\mathbf{g}_1 \cdot \mathbf{g}_2 \neq 0$, $\mathbf{g}_2 \cdot \mathbf{g}_3 = 0$ and $\mathbf{g}_1 \cdot \mathbf{g}_3 = 0$) holds demonstrating a non-cartesian system. A cartesian local base is constituted as follows

$$\begin{aligned}
 \mathbf{a}_1 &= \frac{\mathbf{g}_1}{\|\mathbf{g}_1\|}, \\
 \mathbf{a}_3 &= \mathbf{g}_3, \\
 \mathbf{a}_2 &= \mathbf{a}_3 \times \mathbf{a}_1.
 \end{aligned} \tag{5.16}$$

In order to use above stated basis vectors the shape-function derivatives and hence the transformation matrix \mathbf{J} needs to be obtained with respect to the local carte-

²These coordinates move with the surface, figuratively they are scratched into the element surface.

sian base coordinates³ θ_β

$$\begin{aligned} \mathbf{g}_\alpha &= N_{I,\xi_\alpha} \mathbf{x}_I \\ \mathbf{x}_{,\xi_\alpha} &= \underbrace{\frac{\partial \mathbf{x}}{\partial \Theta_\beta}}_{\mathbf{a}_\beta} \underbrace{\frac{\partial \Theta_\beta}{\partial \xi_\alpha}}_{\mathbf{J}_{\beta\alpha}} \Leftrightarrow \frac{\partial \mathbf{x}}{\partial \xi_\alpha} = \mathbf{J}_{\alpha\beta} \mathbf{x}_{,\beta}, \quad \alpha, \beta \in 1, 2, \end{aligned} \quad (5.17)$$

which can be scalar multiplied by \mathbf{a}_γ to obtain the Jacobian matrix

$$\begin{aligned} \mathbf{g}_\alpha &= \mathbf{a}_\beta \mathbf{J}_{\beta\alpha} \\ \mathbf{g}_\alpha \cdot \mathbf{a}_\gamma &= \underbrace{\mathbf{a}_\beta \cdot \mathbf{a}_\gamma}_{=\delta_{\beta\gamma}} \mathbf{J}_{\beta\alpha} \\ \mathbf{g}_\alpha \cdot \mathbf{a}_\gamma \delta_{\beta\gamma} &= \mathbf{J}_{\beta\alpha} \\ \mathbf{g}_\alpha \cdot \mathbf{a}_\beta &= \mathbf{J}_{\beta\alpha} \\ \mathbf{J} &= \begin{bmatrix} \mathbf{g}_1 \cdot \mathbf{a}_1 & \mathbf{g}_2 \cdot \mathbf{a}_1 \\ \mathbf{g}_1 \cdot \mathbf{a}_2 & \mathbf{g}_2 \cdot \mathbf{a}_2 \end{bmatrix} \end{aligned} \quad (5.18)$$

and its determinant

$$\begin{aligned} \det \mathbf{J} &= J_{11} J_{22} - J_{12} J_{21} \\ &= (\mathbf{g}_1 \cdot \mathbf{a}_1)(\mathbf{g}_2 \cdot \mathbf{a}_2) - (\mathbf{g}_1 \cdot \mathbf{a}_2)(\mathbf{g}_2 \cdot \mathbf{a}_1). \end{aligned} \quad (5.19)$$

With \mathbf{J} it is now possible to compute the derivatives of N_I making use of equation (5.17)

$$N_{I,\alpha} = J_{\alpha\beta}^{-1} N_{I,\xi_\beta}, \quad \alpha, \beta \in 1, 2. \quad (5.20)$$

Furthermore, quantities transferred from a global cartesian to the local curvilinear base system call for a segregate treatment as it is compulsory for the relative velocity $\dot{u}_i^r \rightarrow \dot{u}_\alpha^r$ where subscript α denotes a description with respect to curvilinear coordinates. Since the relative velocity $\dot{\mathbf{u}}^r$ is expressed with respect to a global Cartesian basis's system \mathbf{e}_i ($i \in 1, 2, 3$)

$$\dot{\mathbf{u}}^r = \sum_{i=1}^{ndm} \dot{u}_i^r \mathbf{e}_i, \quad (5.21)$$

but is to be introduced into equation (5.3) assuming curvilinear coordinates on the element level - one has to write the relative velocity in terms of

$$\dot{u}_\alpha^r = \dot{u}_i^r (\mathbf{e}_i \cdot \mathbf{a}_\alpha), \quad (5.22)$$

³Introduced at the GAUSS points.

such that equations (5.8) and (5.23) modify. In order to evaluate the dot products in equation (5.23), the local Cartesian basis $(\mathbf{a}_1, \mathbf{a}_2, \mathbf{a}_3)$ is employed [eqn (5.16)] such that we are able to eliminate the metric tensor components. Now proceeding with the discretization of the right hand side leads to

$$\begin{aligned}
\mathcal{G}^L &= \overbrace{\sum_J \left[\int_{\mathcal{L}^m} \frac{h^3}{12\mu} N_{J,\alpha} \widehat{\eta}_J^p p_{,\alpha} \, da - \int_{\mathcal{L}^m} h \dot{u}_\alpha^r N_{J,\alpha} \widehat{\eta}_J^p \, da - \int_{\partial\mathcal{L}^m} q_n N_J \widehat{\eta}_J^p \, dl \right]}^{=: \mathcal{G}^F(\mathbf{u}, p)} \\
&\quad + \overbrace{\sum_J \left[- \int_{\mathcal{L}^-} p n_j^- N_J \widehat{\eta}_{Jj}^u \, da - \int_{\mathcal{L}^+} p n_j^u N_J \widehat{\eta}_{Jj}^u \, da \right]}^{=: \mathcal{G}_j^C(\mathbf{u}, p)} \\
&\quad + \overbrace{\sum_J \left[- \int_{\mathcal{L}^m} \widehat{\eta}_J^p N_{J \in C} \{p - p_a\} \, da \right]}^{=: \mathcal{G}^{Cav}(p)} \\
&= \sum_J \widehat{\eta}_J^p \left[\int_{\mathcal{L}^m} \frac{h^3}{12\mu} N_{J,\alpha} p_{,\alpha} \, da - \int_{\mathcal{L}^m} h \dot{u}_\alpha^r N_{J,\alpha} \, da - \int_{\partial\mathcal{L}^m} q_n N_J \, dl \right] \\
&\quad + \sum_J \widehat{\eta}_{Jj}^u \left[- \int_{\mathcal{L}^-} p n_j^- N_J \, da - \int_{\mathcal{L}^+} p n_j^u N_J \, da \right], \tag{5.23}
\end{aligned}$$

with $\alpha \in 1, 2$ and $j \in 1, 2, 3$. Here \mathcal{G} denotes discretized terms.

Discretization of fluid parts

Inserting $\widehat{\eta}_{\alpha 1}^p = N_{J,\alpha 1} \widehat{\eta}_J^p$ and $\Delta p_{,\alpha 2} = N_{I,\alpha 2} \Delta p_I$ into (5.10) the discretized formula equals

$$\begin{aligned}
\frac{d\mathcal{G}^F}{dp} &= \sum_I \sum_J \left[\int_{\mathcal{L}^m} \left[\frac{h^3}{12\mu} N_{J,\alpha 1} \widehat{\eta}_J^p \delta_{\alpha 2 \alpha 1} N_{I,\alpha 2} \Delta p_I - \mu_1 \frac{h^3}{12\mu} N_{J,\alpha 1} \widehat{\eta}_J^p p_{,\alpha 1} N_{I,\alpha 2} \Delta p_I \right] da \right] \\
&= \sum_I \sum_J \widehat{\eta}_J^p \left[\int_{\mathcal{L}^m} \frac{h^3}{12\mu} N_{I,\alpha 2} (N_{J,\alpha 2} - \mu_1 N_{J,\alpha 1} p_{,\alpha 1}) \, da \right] \Delta p_I \tag{5.24}
\end{aligned}$$

Using shape-functions $\widehat{\eta}_{\alpha 1}^p = N_{J,\alpha 1} \widehat{\eta}_J^p$ and $\Delta u_i^{+/-} = N_I \Delta u_{Ii}^{+/-}$ in (5.8) one obtains

$$\begin{aligned}
\frac{\partial \mathcal{G}^F}{\partial u_i} &= \pm \sum_I \sum_J \left[\int_{\mathcal{L}^m} \left(\frac{3h^2}{12\mu} N_{J,\alpha 1} \widehat{\eta}_J^p p_{,\alpha 1} N_I \Delta u_{Ii}^{+/-} \mathbf{n}_i^m - \dot{u}_{\alpha 1}^r N_{J,\alpha 1} \widehat{\eta}_J^p N_I \Delta u_{Ii}^{+/-} \mathbf{n}_i^m \right) da \right] \\
&= \pm \sum_I \sum_J \widehat{\eta}_J^p \left[\int_{\mathcal{L}^m} N_{J,\alpha 1} N_I \mathbf{n}_i^m \left(\frac{h^2}{4\mu} p_{,\alpha 1} - \dot{u}_{\alpha 1}^r \right) \, da \right] \Delta u_{Ii}^{+/-} \tag{5.25}
\end{aligned}$$

where \mathbf{u}^+ is valid at nodes $I, J := 9, \dots, 12$ and \mathbf{u}^- is valid at nodes $I, J := 1, \dots, 4$. The nodal normal vectors for height computation are built at the mid nodes $T = 5, \dots, 8$:

$$n_i^m = \frac{1}{\left\| \sum_T e_{ijk} N_{T,\epsilon} X_{Tj} N_{T,\mu} X_{Tk} \right\|_2} \left(\sum_T e_{ijk} N_{T,\epsilon} X_{Tj} N_{T,\mu} X_{Tk} \right) \quad (5.26)$$

Discretization of contact parts

Introducing $\hat{\eta}_i^u = N_J \hat{\eta}_{Ji}^u$ and $\Delta p = N_I \Delta p_I$

$$\begin{aligned} \frac{\partial \mathcal{G}^C}{\partial p} &= \sum_I \sum_J \left[- \int_{\mathcal{L}^-} n_i^- N_J \hat{\eta}_{Ji}^u N_I \, da - \int_{\mathcal{L}^+} n_i^u N_J \hat{\eta}_{Ji}^u N_I \, da \right] \Delta p_I \\ &= \sum_I \sum_J \hat{\eta}_{Ji}^u \left[- \int_{\mathcal{L}^-} n_i^- N_J N_I \, da - \int_{\mathcal{L}^+} n_i^u N_J N_I \, da \right] \Delta p_I \end{aligned} \quad (5.27)$$

Introducing shape functions $\hat{\eta}_j^u = N_J \hat{\eta}_{Jj}^u$, $\Delta u_{s,\epsilon}^{-/+} = N_{I,\epsilon} \Delta u_{Is}^{-/+}$ and $\Delta u_{s,\mu}^{-/+} = N_{I,\mu} \Delta u_{Is}^{-/+}$ leads to

$$\begin{aligned} \frac{\partial \mathcal{G}^C}{\partial u_j^{-/+}} &= \mp \int_{\mathcal{L}^{-/+}} p N_J \hat{\eta}_{Jj}^u \left(e_{jst} N_{I,\epsilon} \Delta u_{Is}^{-/+} x_{t,\mu}^{-/+} + e_{jgn} x_{g,\epsilon}^{-/+} \delta_{sn} N_{I,\mu} \Delta u_{Is}^{-/+} \right) da \\ &= \mp \sum_I \sum_J \hat{\eta}_{Jj}^u \left[p N_J \left(e_{jst} N_{I,\epsilon} x_{t,\mu}^{-/+} + e_{jgn} x_{g,\epsilon}^{-/+} \delta_{sn} N_{I,\mu} \right) da \right] \Delta u_{Is}^{-/+} \end{aligned} \quad (5.28)$$

Discretization of constraint part

$$\frac{d\mathcal{G}^{Cav}}{dp} = - \sum_I \sum_J \hat{\eta}_{Jj}^p \left[\int_{\mathcal{L}^m} N_I N_J \epsilon_C \, da \right] \Delta p_I \quad (5.29)$$

This leads to the following linear system of equations according the finite element introduced in figure 5.2:

$$\begin{pmatrix} \frac{\partial \mathcal{G}^{C-}}{\partial \mathbf{n}^-} \frac{\partial \mathbf{n}^-}{\partial \mathbf{u}^-} & 0 & \frac{\partial \mathcal{G}^{C-}}{\partial p^m} \\ 0 & \frac{\partial \mathcal{G}^{C+}}{\partial \mathbf{n}^+} \frac{\partial \mathbf{n}^+}{\partial \mathbf{u}^+} & \frac{\partial \mathcal{G}^{C+}}{\partial p^m} \\ \frac{\partial \mathcal{G}^F}{\partial h} \frac{\partial h}{\partial \mathbf{u}^-} & \frac{\partial \mathcal{G}^F}{\partial h} \frac{\partial h}{\partial \mathbf{u}^+} & \frac{\partial \mathcal{G}^F}{\partial p^m} + \frac{\partial \mathcal{G}^F}{\partial \mu} \frac{\partial \mu}{\partial p^m} + \frac{\partial \mathcal{G}^{Cav}}{\partial p^m} \end{pmatrix} \begin{pmatrix} \Delta \mathbf{u}^- \\ \Delta \mathbf{u}^+ \\ \Delta p^m \end{pmatrix} = - \begin{pmatrix} \mathcal{G}^{C-} \\ \mathcal{G}^{C+} \\ \mathcal{G}^F + \mathcal{G}^{Cav} \end{pmatrix} \quad (5.30)$$

Chapter 6

Macroscale numerical examples

In order to demonstrate the finite element framework a three way comparison of computational results for a journal bearing with input parameters shown in table 6.1 is discussed. Based on these parameters both *inertia forces*

$$\mathcal{R}_i = \frac{(10^3)(4.7)(1.41)}{10^{-3}} \left(\frac{0.00005}{1.41} \right)^2 \approx 0.0083 \ll 1 \quad (6.1)$$

and *body forces*

$$\frac{\mathcal{R}_i}{\mathcal{F}_n^2} = \frac{(10^3)(9.81)(0.00005)^2}{(10^{-3})(4.7)} \approx 0.005 \ll 1 \quad (6.2)$$

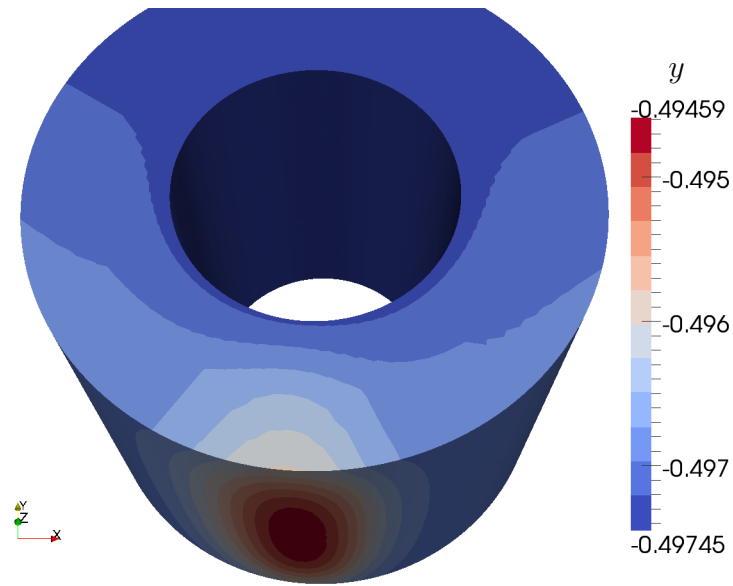
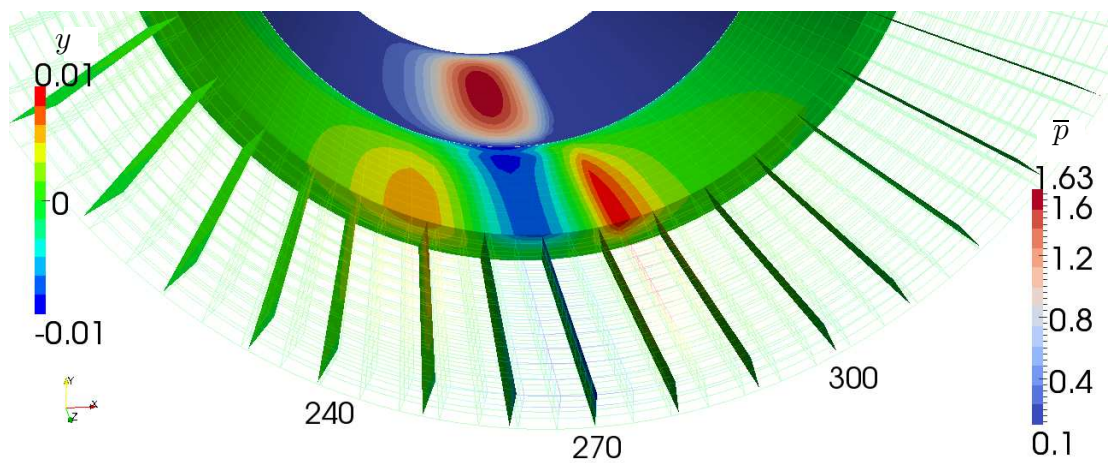
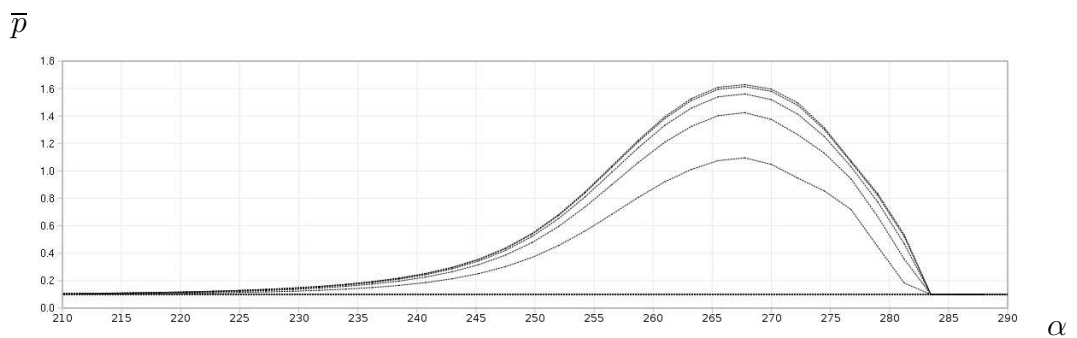
are negligible according to equations (3.3) and (3.4). Here the gap height for a centered journal is uniformly $h^c = 0.5mm$. A pressure distribution being able to carry the journal occurs for a non-conformal flow-channel with a gap height of approximately $h^c = 0.05mm$, such that within this high pressure region - the region of interest - both *body forces* and *gravity forces* are negligible.

Results in figure 6.1 and figure 6.2 are subject to quadratic shape functions, whereas figure 6.3 shows computational results with linear shape functions being used. Further figure 6.1 and figure 6.3 regard the effect of cavitation via the penalty method, however figure 6.2 does not, such that the pressure drops below the ambient pressure $p_a = 0.1$ MPa. Furthermore within the finite lubrication regime a spike (2nd pressure maximum) occurs due to a rubber bulge behind the pressure maximum for figure 6.1 (not shown due to oscillations) [[73],p.410] and [[33],Chapter 18]. For quadratic shape-functions high pressure plots display strong oscillations (not shown), which also have been observed by Yang and Laursen [86]. Furthermore, Heinrich and Zienkiewicz [35] state that oscillations in flow problems arise from dominant contributing 1st derivative terms and that a special “up winding“ procedure on the choice of the weighting functions circumvents these oscillations. Presently, for high pressures p , the POISEUILLE term of the REYNOLDS

equation may be responsible for a similar effect and a "upwinding" procedure or alternatively a mixed formulation employing 2nd order shapefunctions for the displacement unknowns and 1st order shapefunctions for the pressure unknowns may alleviate the undesirable oscillations.

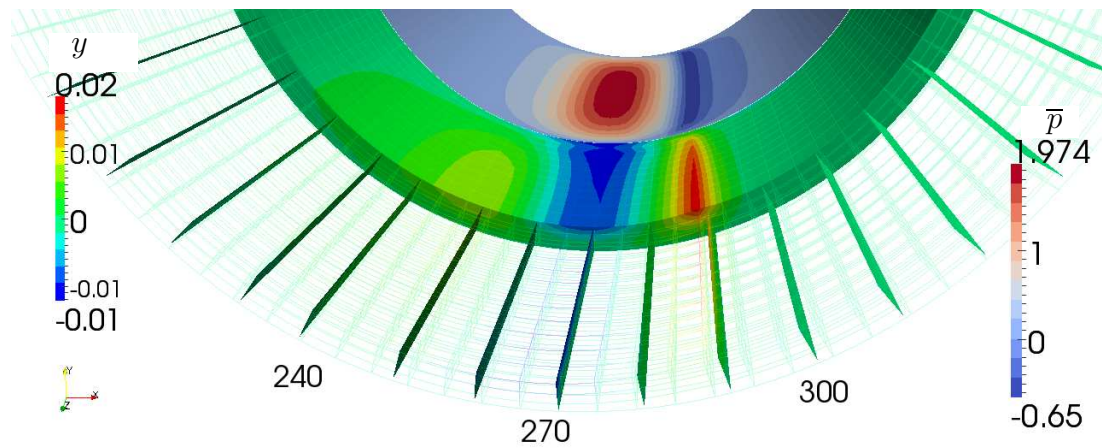
Table 6.1: Material parameters employed are summarized.

	Order of shape functions			$1_{a,2b,c}$
Sleeve (Neo Hook)	Young's Modulus	[N/mm ²]	E	475.0
	Poisons Ratio		ν	0.499
	Cylinder dimensions	[mm]	$\varnothing^o \times \varnothing^i \times \text{width}$	490x451x100
	Number of quadratic Elements		$\varnothing^o \times \varnothing^i \times \text{width}$	80x24x3
Journal	Young's Modulus	[N/mm ²]	E	50000.0
	Poisons Ratio		ν	0.3
	Cylinder dimensions	[mm]	$\varnothing^o \times \varnothing^i \times \text{width}$	450x240x100
	Number of Elements		$\varnothing^o \times \varnothing^i \times \text{width}$	160x48x6 _a ,80x24x3 _{b,c}
LUBRICANT (Water)	Rel. vel. (journal - sleeve)	[mm/s]	$\bar{\mathbf{u}}^r$	2356.0
	Viscosity (at 20°C)	[MPa s]	η	$1.0 \cdot 10^{-9}$
	pressure-viscosity coefficient	[Pa ⁻¹]	α	0.0
	ambient-pressure	[MPa]	\bar{p}_a	0.1
	cavitation penalty parameter	[MPa]	ϵ_C	0.0 _c ,1.0e ⁶ _{a,b}
	Number of Elements		$\varnothing^o \times \varnothing^i \times \text{width}$	160x48x1 _a ,80x24x1 _{b,c}

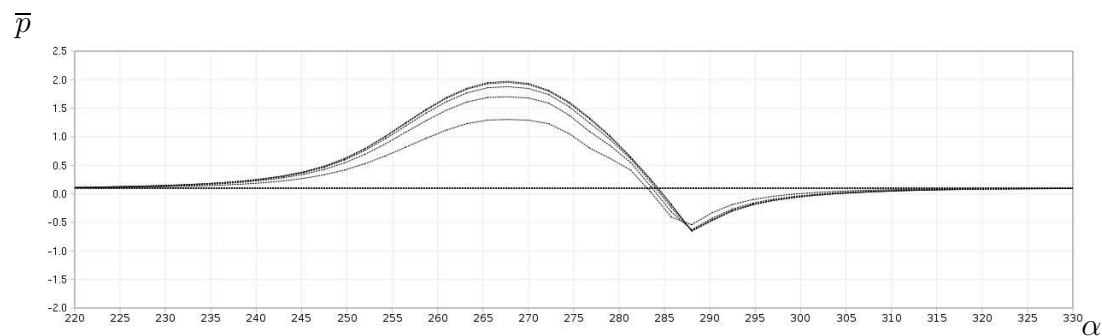
(a) journal y -displacement causes lubricant pressure(b) sleeve y -displacement caused by lubricant pressure

(c) pressure plot

Figure 6.1: Computation making use of quadratic shapefunctions and regarding cavitation. a) Side view on journal bearing b) Close up view on sleeve y -displacement (foreground) scaled by a factor of five, for a better illustration the pressure distribution is shifted to the background the journal is hidden.



(a) sleeve y -displacement caused by lubricant pressure



(b) pressure plot

Figure 6.2: Computation making use of quadratic shapefunctions - neglecting cavitation. a) Side view on journal bearing b) Close up view on sleeve y -displacement (foreground) scaled by a factor of five, for a better illustration the pressure distribution is shifted to the background the journal is hidden.

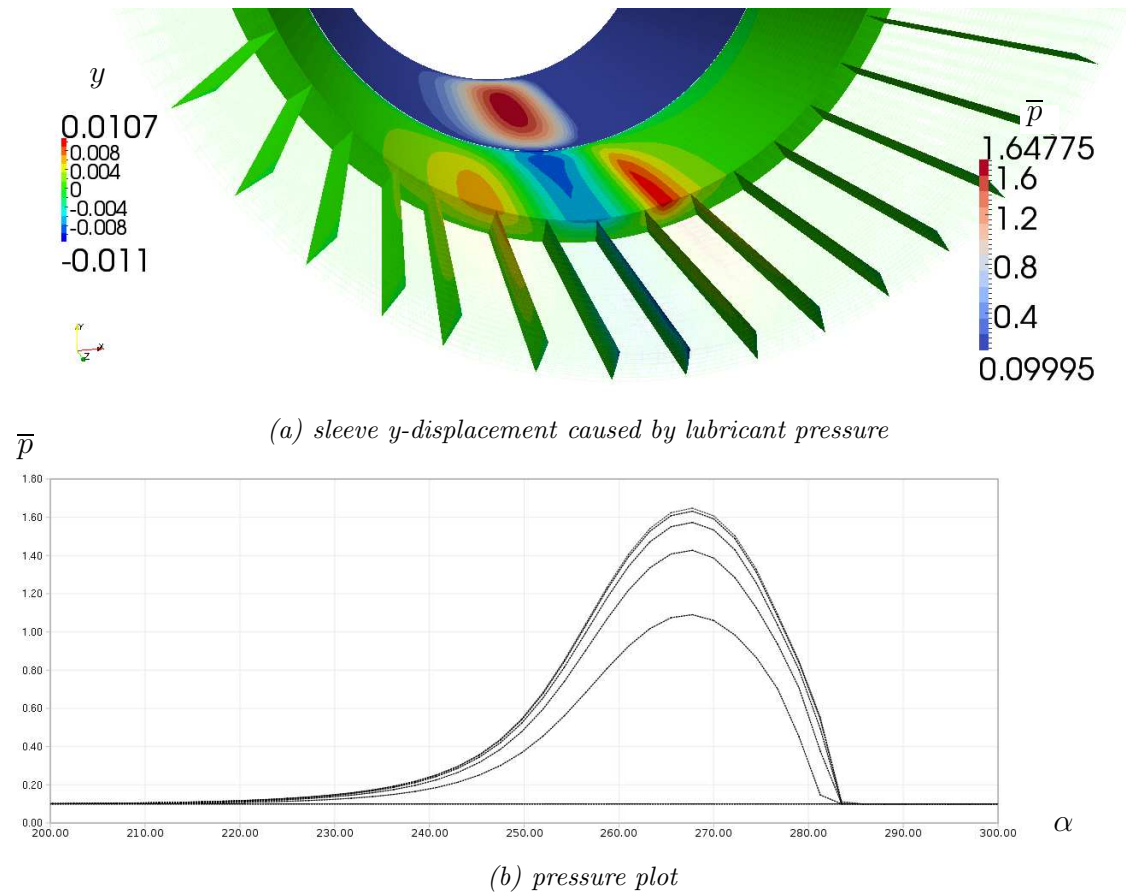


Figure 6.3: Computation making use of linear shapefunctions and regarding cavitation. a) Side view on journal bearing b) Close up view on sleeve y-displacement (foreground) scaled by a factor of five, for a better illustration the pressure distribution is shifted to the background the journal is hidden.

Chapter 7

Microscale test procedure

7.1 Homogenization fundamentals

In order to prescribe material behavior from our macroscopic point of view, constitutive equations e.g. for solid materials (sec 2.3) relate stress to strain. These equations are used for several materials - like concrete, steel and others - based on the assumption that a body's volume is occupied by a homogenous material. But analyzing the material's microstructure reveals a complete heterogeneous composition, such that above assumption is violated. A tension test on a composite bar (fig 7.1) illustrates the displacement response for a two phase material bar. If the bar consists of half one phase and half the other, the displacement response is piecewise smooth, assuming a linearly elastic response. Now refining previous distribution we obtain a displacement field of many piecewise smooth lines which can be well-approximated by a single line. At last the phase distribution is refined such that we can not distinguish between the approximated and real displacement field. See for example [7, 12, 22, 37, 75, 79, 89].

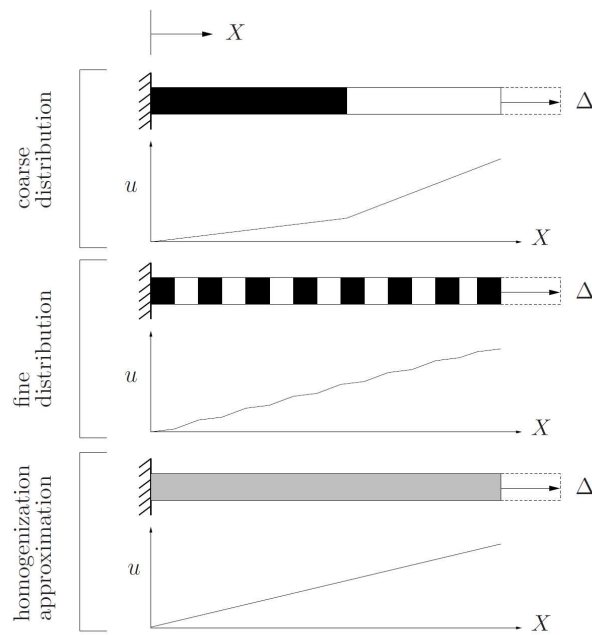


Figure 7.1: One-dimensional Composite bar, from [75].

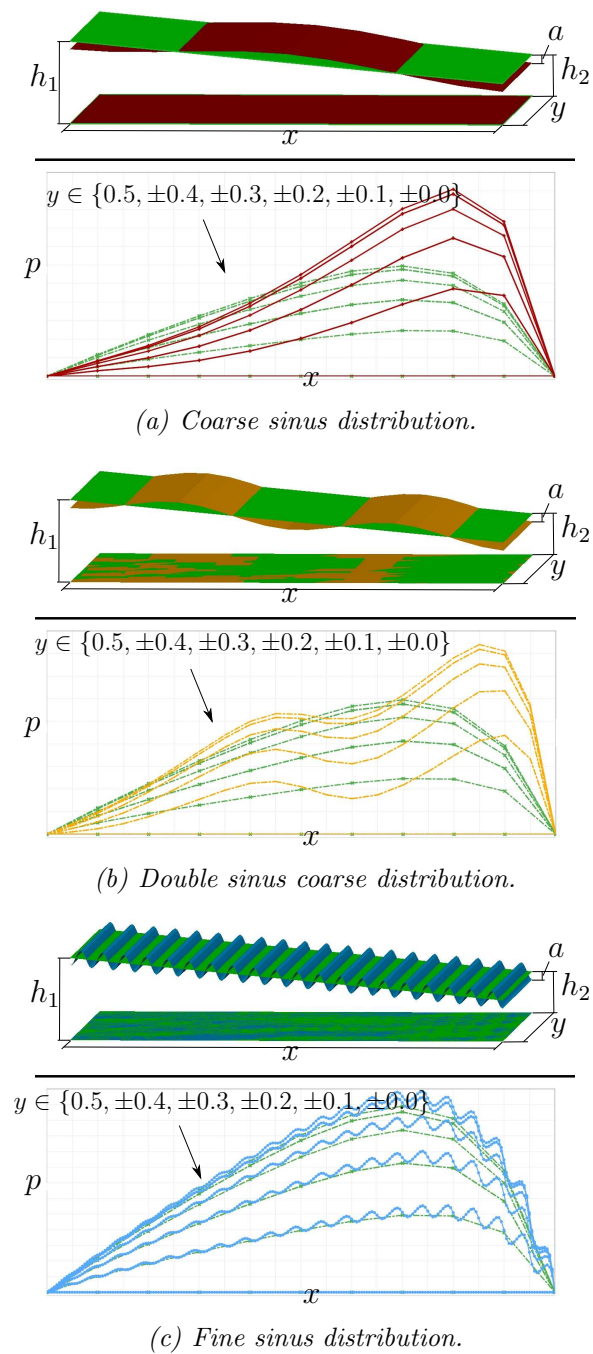


Figure 7.2: Three-dimensional flow over rough surfaces. Height components are scaled by a factor of five.

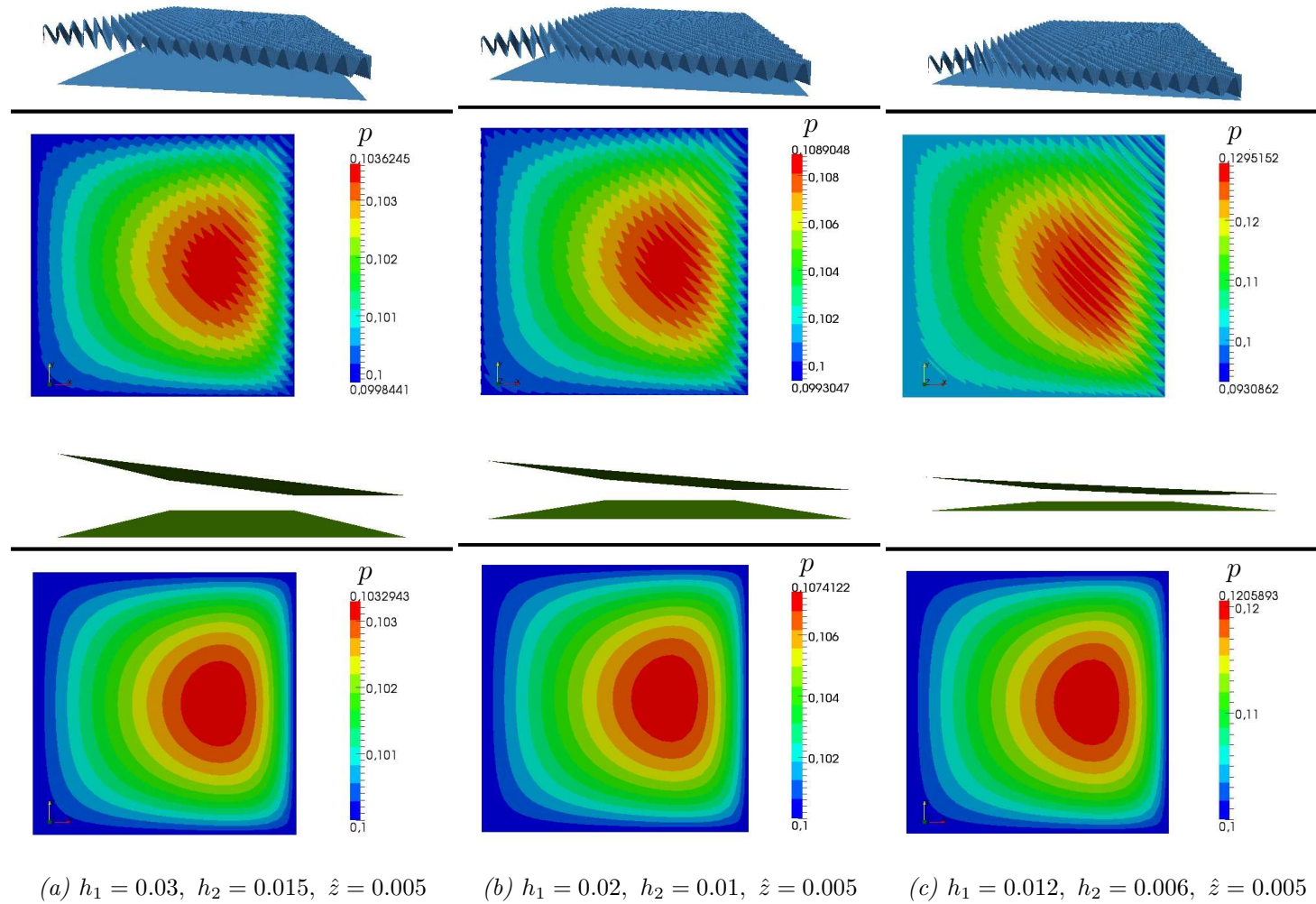


Figure 7.3: Three-dimensional flow over skew rough surfaces. Height components are scaled by a factor of five.

In case of lubrication problems inhomogeneity arises from surface roughness, which can be elucidated on a simple flow test (fig 7.2) made up in the same fashion as it was done for the composite bar (fig 7.1). Assume a flow between two flat plates forming a slider bearing, whereas the upper one is fixed and inclined such that the inlet is denoted by h_1 and the outflow lies at h_2 . The lower surface moves with a relative velocity in tangential positive x -direction carrying over the fluid. Furthermore the bearing surrounding pressure is assumed to be constant and can be identified at the base of the pressure axis p in the plots. Outcome of this test is a smooth parabolic pressure response along the flow direction x for different cross sections¹, with a maximum at position $x = 0.8$. This result can be considered homogeneous. Now a bunch of new tests is introduced where the upper inclined surface is superimposed by a sinusoidal roughness having the same amplitude but varying wavelength. Comparing the pressure distribution for a single sinus surface roughness to the flat surface test shows a strong deviation in magnitude and shape (fig 7.2_a) stating a strong heterogeneous response. However in figure 7.2_b a double sinus roughness is chosen which also gives a heterogeneous pressure distribution but being a bit closer to the flat surface result (in terms of homogeneity). At last the number of sinusoid's is increased to twenty ending up in a pressure distribution that renders the homogenous parabolic chart qualitatively well (fig 7.2_c), besides a few oscillations. It is readily conceivable that for decreasing roughness wavelength the homogeneous limit will be reached, which is not known and is not necessarily equivalent to the mean surface being used for the homogeneous slider bearing example. Subsequently another test with an oblique roughness superimposed on the inclined surface was carried out showing that the result of a flat surface is not necessarily the homogeneous limit of a heterogeneous surface, see figure 7.3.

The goal of homogenization is to use a homogeneous material description that approximates the behavior of a heterogeneous problem. Hence it follows up the question to determine the **macroscopic properties** of such a *macroscale* homogeneous material from the *microscale* heterogeneous problem. To obtain such properties from the microscale an *appropriate sample* being subject to *appropriate boundary conditions* is mandatory and hence must be identified.

All of the investigations to be performed in this study employ micro structures that may be classified as being in the REYNOLDS roughness regime, together with gap heights where roughness effects are significant. The roughness classification goes back to the work of Elrod [28] and verifies the assumption regarding the validity of the REYNOLDS equation on the microscale within the micro mechanical analysis. The investigations of Mitsuya and Fukui [52] indicate that, the roughness

¹Pressure plots are taken along the x -direction at different width positions $y \in \{0.5, \pm 0.4, \pm 0.3, \pm 0.2, \pm 0.1, \pm 0.0\}$. The arrow assigns high pressure plots to the center and low ones to the side.

wavelength to mean film thickness ratio should be approximately five or larger if this assumption is to hold. Otherwise, the Stokes roughness regime becomes dominant and a direct solution of the Stokes equation is suggested, although alternative limit equations have also been obtained in the mathematical literature [9]. In the case of dynamic effects, a reversion to the original NAVIER-STOKES equation may be required within the homogenization framework, which may also be necessary in the case of near-contact situations where the gap height to combined roughness ratio is very small [25]. In the other extreme of this ratio, roughness effects are negligible. They become dominant in the vicinity of a gap to combined roughness ratio of the order of ten and below [54].

Appropriate sample

This identification procedure aims to find a sufficient *representative volume element* (RVE) being the grounding of micro mechanical analysis. In case of microscopically heterogeneous but macroscopically homogeneous problems the question arises how to obtain the macroscopic homogeneous “material” parameters from a microscopically heterogeneous problem. Due to limited computational power (or time) the sample being investigated should deliver an appropriate result but needs to be chosen as small as possible. For realistic surfaces the smallest sample size has to be obtained by *sample enlargement* and hence monitoring the flow response (e.g. flux \mathbf{q}) whilst varying the sample size. An adequate sample size is obtained if

$$\left| \frac{\mathbf{q}^{j+1} - \mathbf{q}^j}{\mathbf{q}^j} \right| < \text{TOL} , \quad (7.1)$$

for a given tolerance TOL. Here increasing j denotes increasing the sample size. Furthermore the flow scatter response for small sample sizes can be filtered to extract the mean

$$\langle\langle \mathbf{q} \rangle\rangle = \frac{1}{M} \sum_{I=1}^M \mathbf{q}_I . \quad (7.2)$$

This is called *ensemble averaging*. Here M denotes the number of samples and \mathbf{q}_I denotes the result from the I^{th} sample. Equation 7.2 should be used in equation (7.1) in order to smoothen convergence with increasing sample size. At convergence the sample will approximate the *representative surface element* (RSE) which is ideally infinitely large.

In the case of periodic surfaces however an exact RSE is identified as a unit cell. Recalling the flow problem the unitcell will be prescribed by a sin wave ($0 \rightarrow 2\pi$). In the remaining part of the thesis we will work with such periodic surfaces.

7.2 Lubricant homogenization methodology

7.2.1 Interface testing procedure

Solving the REYNOLDS equation for a macroscale lubrication problem while taking into effect surficial microscopic roughness that is several orders of length scales smaller demands a very fine mesh resolution and hence prohibitive computational times. To reduce the work load, a homogenization scheme is introduced. The basic idea is outlined in figure 7.4, where a mass balance

$$-\text{div}[\bar{\mathbf{q}}] = 0 \quad (7.3)$$

has to be solved on the macroscale, but a constitutive equation $\bar{\mathbf{q}}$ prescribing the flux over a rough surface is not represented by the classical REYNOLDS flux. Hence an explicit constitutive equation $\bar{\mathbf{q}}$ is not known. Rather, the *homogenized macroscopic flux* $\bar{\mathbf{q}}$ is extracted from a rough microscale problem that is associated with the macroscale interface at each numerically relevant point, e.g. the integration point. This interface sample problem will be solved as follows:

1. compute macroscale variables from a flat surface macroscale problem, using the mass balance (regarding cavitation in [eqn (5.3)] but without substituting the REYNOLDS flux form)
2. where cavitation does not occur, pass macroscale variables to the microscale and incorporate them as boundary conditions on the test sample,
3. solve a rough surface microscale problem, using REYNOLDS equation [eqn (5.3)] (neglecting cavitation), for the local flux \mathbf{q} ,
4. compute the macroscale flux $\bar{\mathbf{q}}$ by surface averaging the local flux and pass it to the macroscale,
5. solve the macroscale problem using the macroscale flux $\bar{\mathbf{q}}$, which now includes the effects of surface roughness to the macroscale.

This procedure is referred to as the *micromechanical test*. To any position in the lubricant at the macroscopic scale such a micro mechanical test is attached. Within the finite element framework, this is done naturally at the Gauss points. Unlike the classical homogenization's setting for the REYNOLDS equation, however, it is not sufficient to solve these attached problems only once in a pre-processing step. Rather, they must be solved simultaneously throughout the macroscopic deformations steps. This is the typical FE^2 framework for the computational homogenization of heterogeneous media – see earlier cited references.

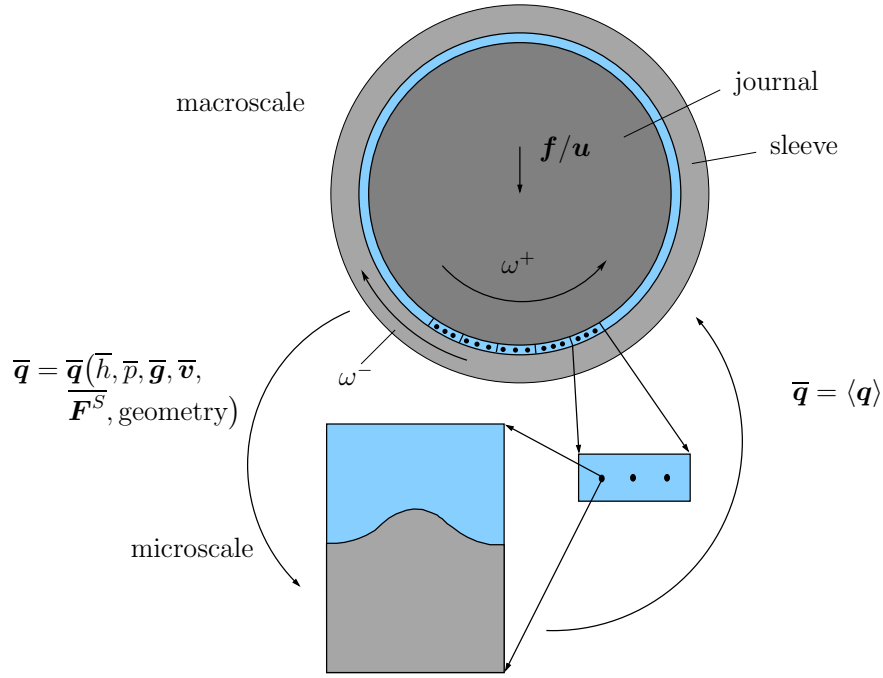


Figure 7.4: Micro-macro loop with parameter interface between macroscale to micro-mechanical test procedure.

The validity of the proposed multiscale analysis framework is assessed through the following conditions:

$$\begin{aligned}
 \bar{\sigma} &= \mathcal{O}(\bar{h}) \ll \bar{c} \\
 \sigma &= \mathcal{O}(h) \ll c \\
 c &\ll \bar{c}
 \end{aligned}
 \tag{7.4}$$

Equations (7.4)_{1,2} ensure that a lubrication formulation holds on the *macroscale* as well as on the *microscale*, respectively. Here $\bar{\sigma}$ and σ denote the standard deviations of roughness whereas the representative length of the flowpath is given via \bar{c} and c for the macroscopic and microscopic problems, respectively. Finally, (7.4)₃ is required to justify the separation of scales that is essential for scale-independent homogenization [Stupkiewicz [71] pp. 9-14]. The separation of scales also justifies the split of the micro mechanical testing procedure, which is the subject of the next section.

7.2.2 Two-Phase micro mechanical test

The introduced *micromechanical test* can be split into a (i) *mechanical phase* followed by a (ii) *lubrication phase* through which an efficient numerical treatment of the homogenization problem can be achieved. This procedure is visualized in figure 7.5. For a typical *micromechanical test*, computational times of 331 s for the *mechanical phase* and 0.12s for the *lubrication phase* can be achieved. This is more than 1.6 times faster compared to a coupled computation time of 554s. This split is exact to within a separation of scales assumption [Temizer and Wriggers [78, section 3]]. If not employed, the solution of the coupled problem, which is now numerically more expensive, would additionally require an explicit satisfaction of (7.4)₃ by choosing the sample small in terms of absolute length scale. When not appropriately chosen, the sample size can influence the macroscopic flux for a given set of boundary conditions. However, such a sample size dependence is not allowed when a separation of scales is admitted. Consequently, the split of the testing procedure ensures an automatic satisfaction of this condition, which is demonstrated in comparison charts (fig 7.6) and (fig 7.7). In both parameter studies, where the gap height \bar{h} or the pressure gradient $\bar{\mathbf{g}}$ are varied, the decoupled computational results remain constant with increasing *sample size* (number of tiles or wave length). However all coupled computations show a strong dependence on varying *sample size* for either increasing the number of tiles or increasing the wave length. The solid deformations in figure 7.8 reports the deformations to the analysis is reported in figure 7.6. For a pressure gradient ($\mathbf{g} = -10^{\text{N/mm}}$) caused deformation one would expect a negative inclined wedge-like deformation of the solid block. But here the viewer observes a bulge at the right side of all solid blocks, which are caused by the periodic boundary conditions, see section 7.2.3. Furthermore the z -displacements at the leading and trailing edges (w.r.t. the x -axes) deviate for different sample sizes (number of tiles t), which causes the varying flux with increasing sample size. This variation is unphysical within a *separation of scales assumption* and is avoided by the *two-phase* setup.

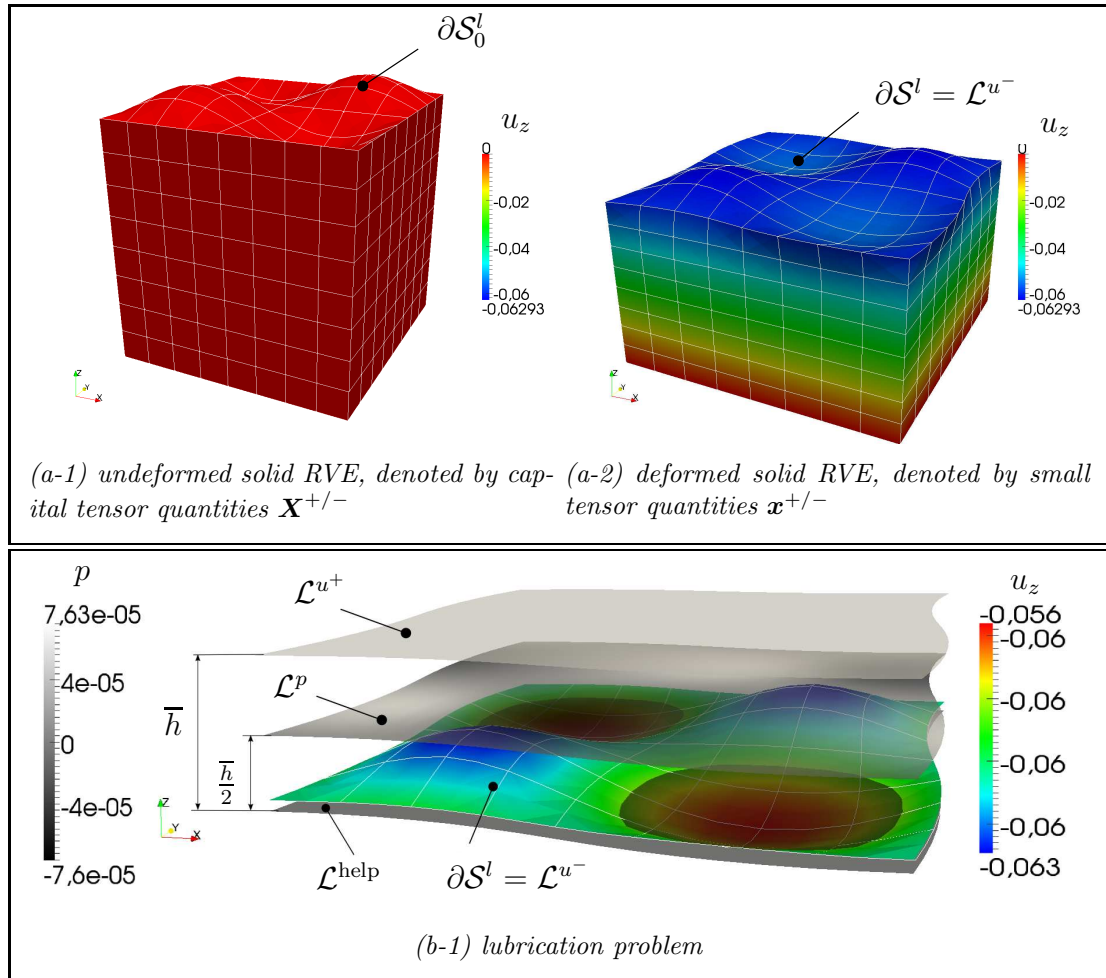
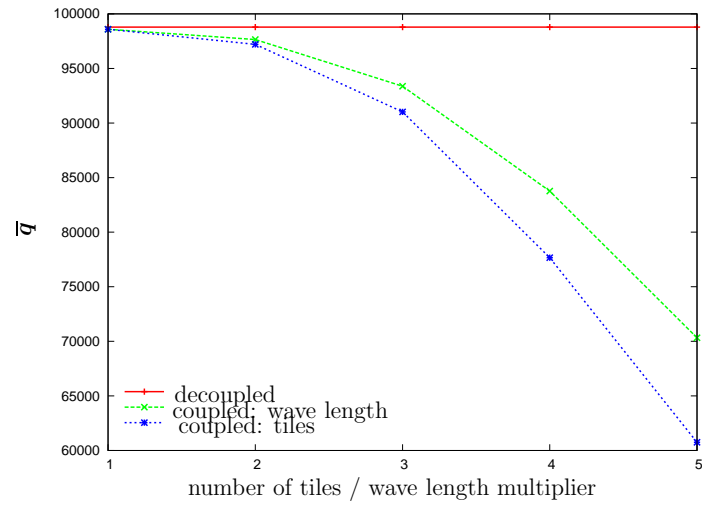
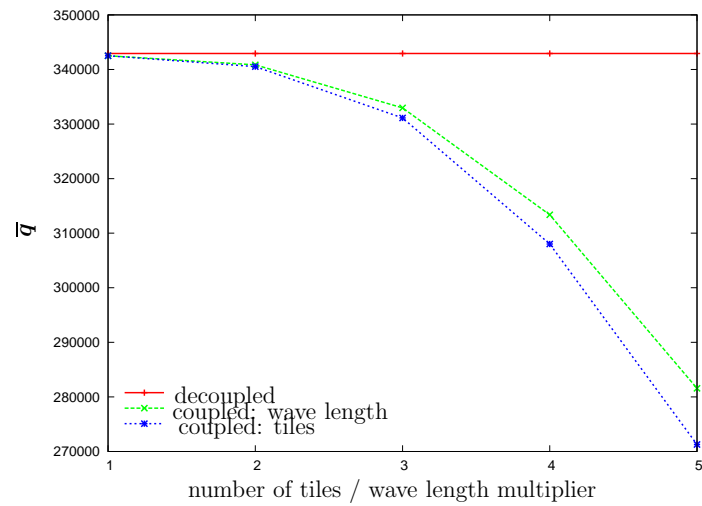
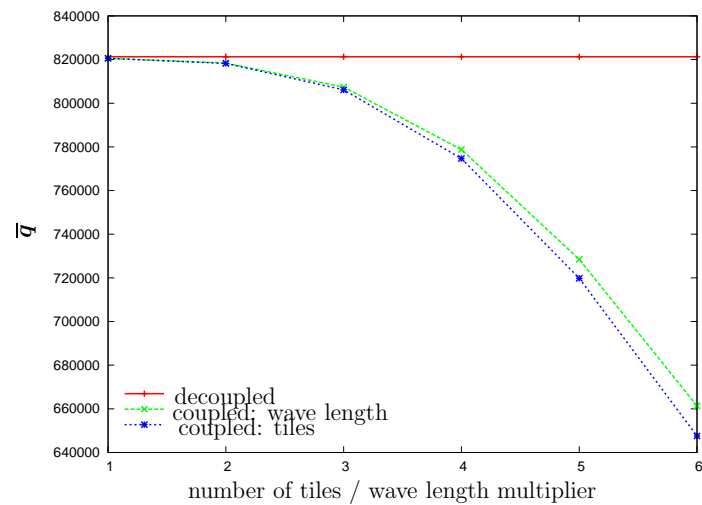
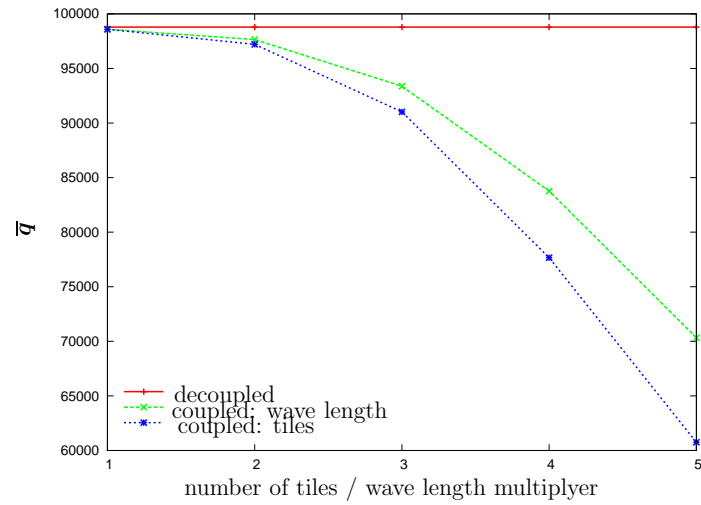
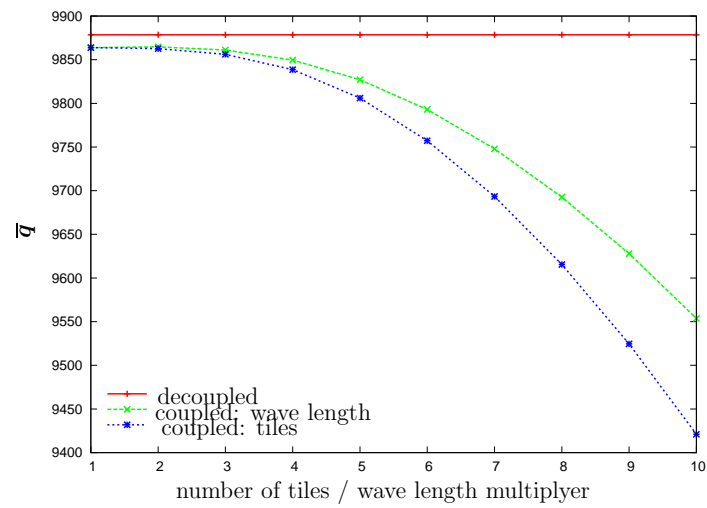
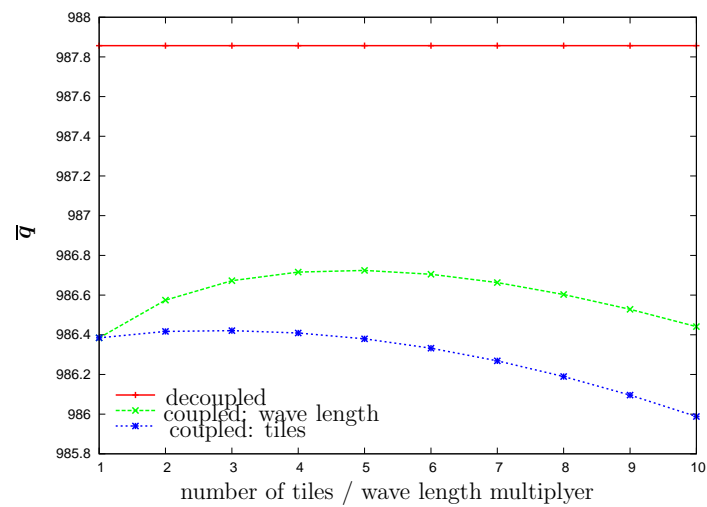


Figure 7.5: Micromechanical split: (a) mechanical phase, subject to $\mathbf{x}^+ - \mathbf{x}^- = \overline{\mathbf{F}^S}(\mathbf{X}^+ - \mathbf{X}^-)$ and (b) lubrication phase, subject to $p^+ - p^- = \hat{\mathbf{g}} \cdot (\mathbf{x}^+ - \mathbf{x}^-)$

(a) $\bar{h} = 0.05\text{mm}$ (b) $\bar{h} = 0.075\text{mm}$ (c) $\bar{h} = 0.1\text{mm}$ **Figure 7.6:** Varying the gap height h , here $\bar{g} = -10\text{N}/\text{mm}$.

(a) $\bar{g} = -10 \text{ N/mm}$ (b) $\bar{g} = -1 \text{ N/mm}$ (c) $\bar{g} = -0.1 \text{ N/mm}$ Figure 7.7: Varying the pressure gradient \bar{g} , here $\bar{h} = 0.05 \text{ mm}$.

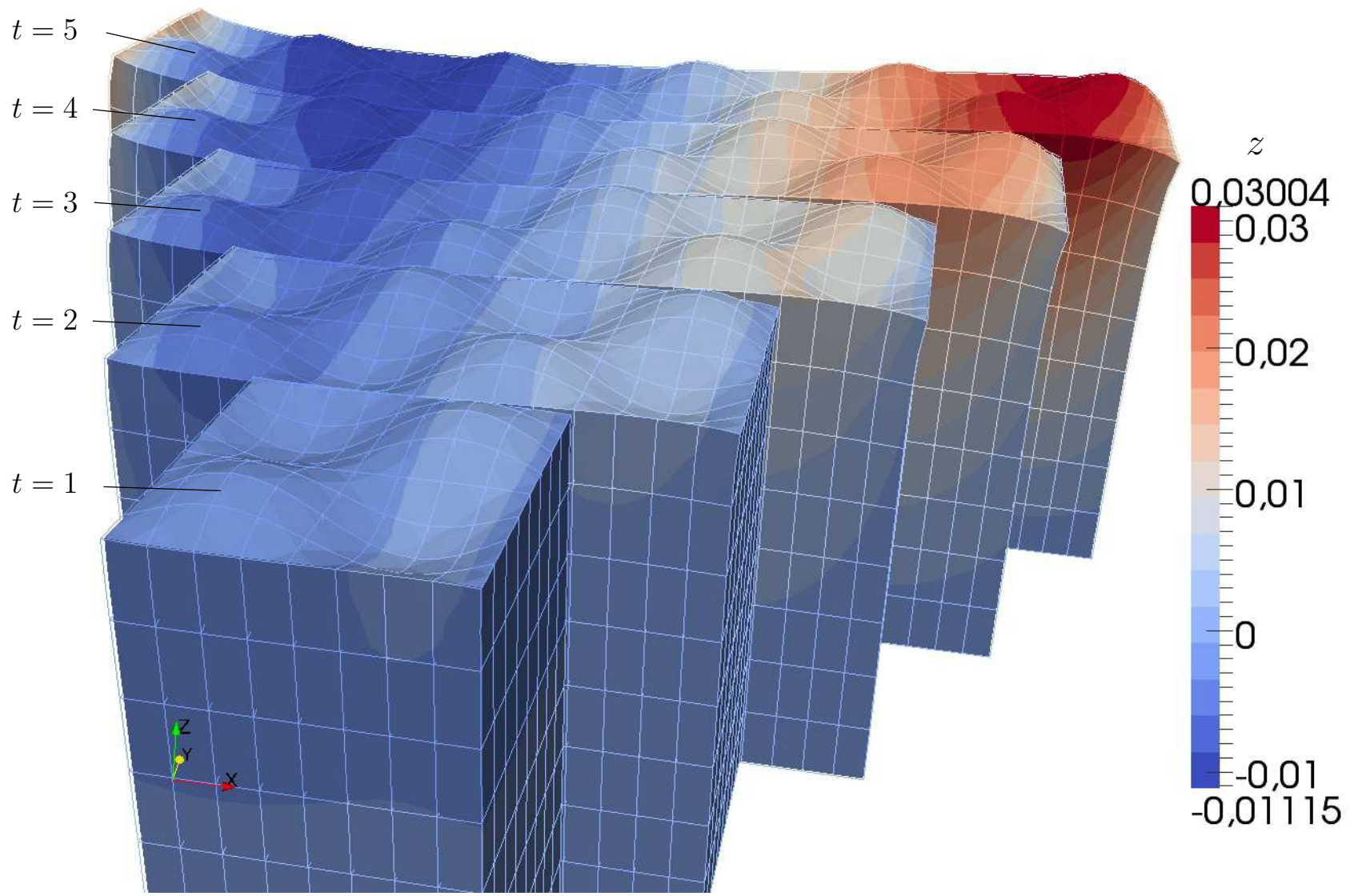


Figure 7.8: Displacements in z direction for increasing number of tiles t .

Within the mechanical phase a purely mechanical problem undergoing finite deformations will be solved. The deformation is induced by:

- the macroscopic fluid pressure ($\bar{p} \approx \text{const}$) acting as a follower load (subject to being linearized) on the top surface \mathcal{S}_0^l of the *Representative Surface Element (RSE)*,
- the macroscale deformation $\bar{\mathbf{F}}^S = \mathbf{1} + \bar{\mathbf{H}}^S$ (applied to the side surfaces $\partial\mathcal{S}^{+/-}$ of the RSE; see sec 7.2.3 and figure 7.9 and Stupkiewicz [71], Temizer and Wriggers [77]), and
- the chosen geometry (roughness) of top surface $\partial\mathcal{S}_0^l$.

Outcome is a deformed surface \mathcal{L}^{u^-} . Employing a constant pressure within the mechanical phase agrees with the asymptotic expansion analysis of Bayada et al. [11] and is consistent with the separation of scales.

Subsequently, the *lubrication phase* can be constructed using the deformed surface \mathcal{L}^{u^-} , see figure 7.5b. In order to form a thin channel, a flat surface \mathcal{L}^{u^+} is placed at a distance \bar{h} above the mean plane of the rough surface \mathcal{L}^{u^-} . For this purpose, introducing

$$\langle \bullet \rangle = \frac{1}{A_0} \int_{\mathcal{L}^{u^-}} \bullet \, da \quad \longrightarrow \quad \bar{h} = \langle h \rangle, \quad \bar{z} = \langle z \rangle, \quad (7.5)$$

at position \bar{z} a flat surface \mathcal{L}^{help} is placed with respect to which the top surface \mathcal{L}^{u^+} is at an average distance \bar{h} with respect to the rough surface \mathcal{L}^{u^-} .

Due to computational reasons (fig 5.2) an intermediate surface \mathcal{L}^p is introduced to compute and store the lubricant local pressure p . The lubrication problem is subject to the following restrictions:

- the top surface is forced to be under tangential motion $\bar{\mathbf{u}}^r$ but \mathcal{L}^{u^-} is fixed and
- the macroscopic pressure gradient $\bar{\mathbf{g}}$ acts on \mathcal{L}^i , see sec 7.2.3 and (fig 7.9).

The former assumption is particularly convenient because it allows a static analysis and is a common starting point in many works [1, 2, 4, 11, 15, 18, 28, 41, 42, 62]. In contrast to this setting, two rough surfaces moving against another or accounting for tangential contact demands a time dependent analysis [49, 52, 55, 72, 80].

Since the pressure distribution is not constant throughout the microscale for a rough surface, \mathbf{g} and \mathbf{q} are of “fast varying” character and hence they must be averaged [eqn (7.5)] before passing them to the macroscale:

$$\bar{\mathbf{g}} = \langle \mathbf{g} \rangle, \quad \bar{\mathbf{q}} = \langle \mathbf{q} \rangle. \quad (7.6)$$

7.2.3 Boundary conditions

At each Gauss point the global variables $(\bar{h}, \bar{p}, \bar{\mathbf{g}}, \bar{\mathbf{u}}^r, \bar{\mathbf{F}}^S, \text{geometry})$ are passed to the micromechanical test procedure, where they are incorporated as boundary conditions. They satisfy the following aspects:

- deliver the exact homogenized response from a unit-cell if the microstructure is periodic [(fig 8.2), Temizer [76]] and
- the macroscopic quantities that appear in the boundary conditions are recovered by surface averaging [sec 7.2.2 Temizer [76]], in particular $\bar{\mathbf{g}} = \langle \mathbf{g} \rangle$.

In the *mechanical phase*, at the bottom layer ∂S_0^r all nodal movements are restricted in the z -direction. Additionally one of these nodes $x \in \partial S_0^r \setminus \partial S_0^i$ has to be fixed in all directions to avoid rigid body motions. On the side surfaces ∂S_0^i periodic boundary conditions are imposed to transfer global deformations to the *microscale* (see equation (7.7) and figure 7.9_a). On the rough surface ∂S_0^l traction boundary conditions are applied as a non-conservative loading, cf. equation (7.8).

$$\mathbf{x}^+ - \mathbf{x}^- = \bar{\mathbf{F}}^S (\mathbf{X}^+ - \mathbf{X}^-) \quad \text{and} \quad \mathbf{t}^+ = -\mathbf{t}^-, \text{ on } \partial S^i = \partial S^- \cup \partial S^+ \quad (7.7)$$

$$\mathbf{t} = -\bar{p}\mathbf{n} \quad , \text{ on } \partial S^l \quad (7.8)$$

Within the *lubrication phase* periodic boundary conditions are used to obtain the pressure distribution on the middle plane nodes. Therefore the side nodes of the middle plane are restricted as follows:

$$p^+ - p^- = \bar{\mathbf{g}} \cdot (\mathbf{x}^+ - \mathbf{x}^-) \quad \text{and} \quad q_n^+ = -q_n^-, \text{ on } \partial \mathcal{L}^i = \partial \mathcal{L}^{p^-} \cup \partial \mathcal{L}^{p^+} \quad (7.9)$$

All remaining degrees of freedom on the surface $\partial \mathcal{L} \setminus \partial \mathcal{L}^i$ are restricted to no displacement and zero pressure, see figure 7.9_b.

7.2.4 Identification of macroscopic quantities

From section 7.2.2 it is known that surface averaging microscopic local quantities gives us macroscopic values and hence the macroscopic flux is identified as $\bar{\mathbf{q}} = \langle \mathbf{q} \rangle$. To study weather a macroscopic constitutive equation can be identified the flux $\bar{\mathbf{q}}$ is decompose additively for observation purposes as suggested in section 8

$$\bar{\mathbf{q}} = \bar{\mathbf{q}}^p + \bar{\mathbf{q}}^c \quad , \quad \begin{cases} \bar{\mathbf{q}}^p = \langle \mathbf{q}^p(h, p, \mathbf{g}) \rangle \\ \bar{\mathbf{q}}^c = \langle \mathbf{q}^c(h, \bar{\mathbf{u}}^r) \rangle \end{cases} \quad (7.10)$$

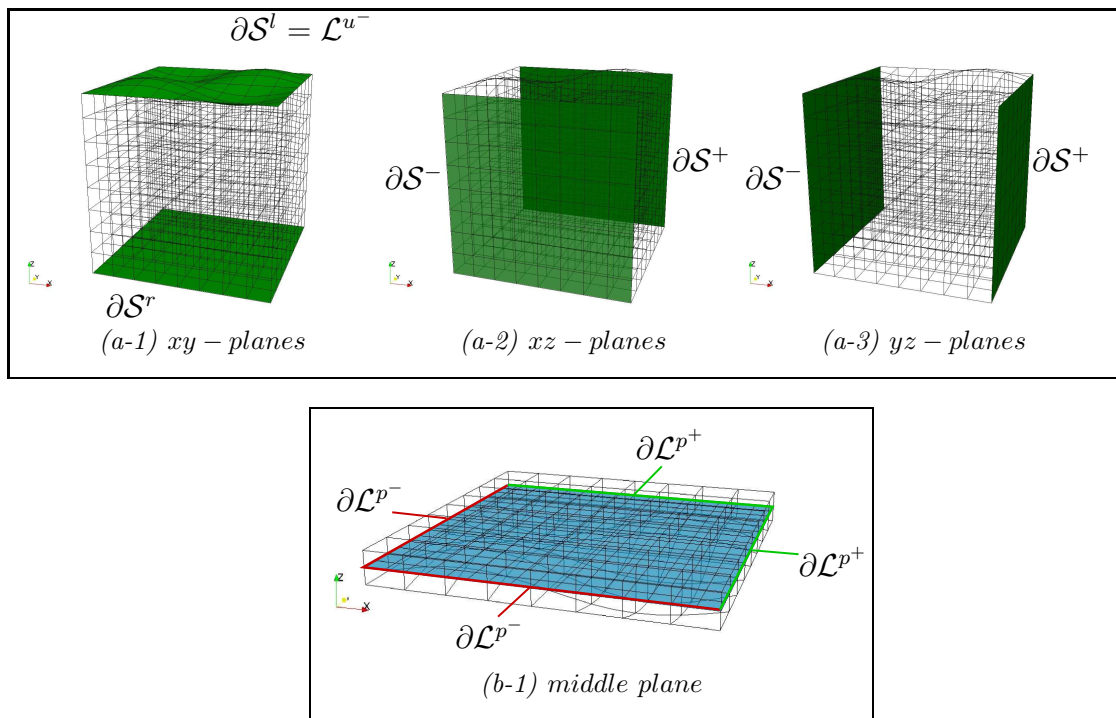


Figure 7.9: Notation of boundaries on (a) the mechanical phase and (b) the lubrication phase

We want to identify macroscopic quantities $(\bar{h}, \bar{p}, \bar{\mu}, \bar{\mathbf{g}})$ via surface averaging to obtain a macroscopic constitutive equation being subject to microscopic rough surfaces

$$\begin{aligned}
\langle \mathbf{q} \rangle &= \left\langle -\frac{h^3}{12\bar{\mu}} \mathbf{g} + h\bar{\mathbf{u}}^r \right\rangle, \quad \begin{cases} \bar{\mu} = \mu(\bar{p}) \\ \mathbf{g} = \text{grad}(p) \end{cases} \\
&= -\frac{1}{12\bar{\mu}} \langle h^3 \mathbf{g} \rangle + \bar{\mathbf{u}}^r \underbrace{\langle h \rangle}_{\equiv \bar{h}} \\
&= -\frac{1}{12\bar{\mu}} \langle h^3 \mathbf{g} \rangle + \bar{h} \bar{\mathbf{u}}^r \\
&= \bar{\mathbf{q}}^p + \bar{\mathbf{q}}^c(\bar{h}, \bar{\mathbf{u}}^r)
\end{aligned} \tag{7.11}$$

and hence we succeed for the COUETTE term but cannot express the Poiseuille term as a function of macroscopic quantities explicitly. It is this term that makes an explicit homogenization analysis necessary, even when the rough surface is rigid.

7.2.5 A micro-macro dissipation equality

In a full Navier-Stokes representation of the fluid, dissipation is induced by the viscous flow which causes temperature rise in the fluid. A consideration of the dissipation effects has been carried out by Cope [23] by simplifying the energy equation under the Reynolds equation assumptions that lead to the thin-film limit. The results obtained have subsequently been verified by Charnes et al. [21] through an alternative derivation where the energy-dissipation relationship was characterized under the thin-film assumptions. Now, since no energy is stored by an incompressible fluid under steady state conditions, the local dissipation \mathcal{D} on the microscale must match the power input \mathcal{P} . Therefore, in order to preserve dissipation through the scale transition of homogenization, the following equivalent conditions must be satisfied:

$$\bar{\mathcal{D}} = \langle \mathcal{D} \rangle \quad \longleftrightarrow \quad \bar{\mathcal{P}} = \langle \mathcal{P} \rangle. \tag{7.12}$$

In this work, the effect of the shear stresses are omitted. Consequently, the power input is expressed only in terms of the *flow work* \mathcal{P}_f [21]:

$$\mathcal{P} \equiv \mathcal{P}_f = -\mathbf{q} \cdot \mathbf{g}. \tag{7.13}$$

The expression of the flow work is admitted to be of the same form on the macroscale:

$$\bar{\mathcal{P}} \equiv \bar{\mathcal{P}}_f = -\bar{\mathbf{q}} \cdot \bar{\mathbf{g}}. \tag{7.14}$$

Consequently, making use of the macroscopic identifications for the flux (sec 7.2.2) and the pressure gradient (sec 7.2.3), preservation of dissipation across the scales requires satisfying

$$\overline{\mathcal{D}} = \langle \mathcal{D} \rangle \quad \longleftrightarrow \quad - \langle \mathbf{q} \cdot \mathbf{g} \rangle = - \langle \mathbf{q} \cdot \mathbf{g} \rangle \quad , \quad (7.15)$$

which will be referred to as the *micro-macro dissipation equality*. The satisfaction of this equality is guaranteed by the periodic boundary conditions employed in this work [78] and therefore the thermodynamical consistency of the computational homogenization approach is guaranteed. It is noted that a complete consideration of the dissipation effects requires incorporating shear stress effects as well. However, this requires imposing shear stresses on the rough surface within the mechanical phase of the micro mechanical test.

Chapter 8

Microscale numerical examples

In this chapter, major aspects of the proposed computational homogenization framework are highlighted. In section 8.1, primarily the influence of the Poisson's ratio ν and surface load \bar{p} is studied at the mechanical phase. Further investigations refer to the lubricant response on changing macroscopic control parameters. For subsequent computations $\bar{\mathbf{g}}$ and $\bar{\mathbf{u}}^r$ have been applied with constant magnitude but changing orientation. Two different surface *geometries* are reviewed in section 8.2 finding an isotropic- and anisotropic-flux behaviour, where the importance of the gap height \bar{h} is additionally exposed. The effect of the displacement gradient $\bar{\mathbf{H}}^S$ will be highlighted in section 8.3. In all other investigations $\bar{\mathbf{H}}^S$ will be set to zero.

Table 8.1: Material parameters employed are summarized. Unless otherwise noted the values in brackets [•] are used.

SOLID (Neo Hook)	Young's Modulus	[N/mm ²]	E	475.0	
	Poisson's Ratio		ν	(0.0-[0.499])	sec 8.1
	Block Dimensions	[mm]	$l_x \times l_y \times l_z$	0.2x0.2x0.4	
	Roughness Amplitude	[mm]	\hat{z}	0.01	
	Number of quadratic Elements		x,y,z	8x8x16	
	Fluid Pressure	[MPa]	\bar{p}	(0.0-[5.0])	sec 8.1
	Surface Geometry			iso-/anisotropic	sec 8.2
	Displacement Gradient		$\overline{\mathbf{H}}^S$	(-1.0,[0.0],1.0)	sec 8.3
LUBRICANT (Water)	Velocity	[mm/s]	$\overline{\mathbf{u}}_\beta^r$	2356.0 ($\overline{\mathbf{g}}=0$)	
	Pressure Gradient	[MPa/mm]	$\overline{\mathbf{g}}_\beta$	0.1 ($\overline{\mathbf{u}}^r=0$)	
	Angle of orientation w.r.t. x-axis	[MPa/mm]	β	[0.0]-360.0	
	Gapheight	[mm]	\bar{h}	([0.05]-0.1)	sec 8.2
	Viscosity (at 20°C)	[MPa s]	μ	$1.0 \cdot 10^{-9}$	
	pressure-viscosity coefficient	[Pa ⁻¹]	α	0.0	
	Number of quadratic Elements		x,y,z	8x8x1	

8.1 Effects of solid incompressibility

To investigate the influence of an incompressible solid onto the surface deformation, a computational test was carried out on six specimens with varying Poisson's ratio ν [figure 8.1]. The specimens have been loaded with increasing pressures \bar{p} acting normal on the top surface $\partial\mathcal{S}_0^l$ of each block, such that the viewer observes decreasing displacement of the top surfaces as well decreasing stress variations from low to high Poisson's ratio $\nu = 0.0 \rightarrow 0.499$ (figure 8.1_{a,b}). However for all specimens stress varies heavily in the surfacial asperities. It is remarked again that $\overline{\mathbf{H}}^S$ is zero for the present investigations.

Two important observations can be made regarding these results. First, for incompressible hyperelastic materials, the effect of the pressure on asperity deformation is negligible. Consequently, the lubrication phase, which is governed primarily by the surface microstructure, will not be influenced significantly by the pressure within the micromechanical testing procedure. However, on the macroscale the pressure may induce surfacial deformation $\overline{\mathbf{H}}^S$, in particular near free edges, which will be observed to have a significant effect on the lubrication response (section 8.3). Similarly, for compressible materials, it has been verified that although large sample compressions are observed, the statistical characteristics of the surface do not vary significantly in the range of pressures investigated (not shown). On the other hand, such large compressions are important because these change the gap height on the macroscopic interface and consequently alter the flow characteristics in a macroscopic elastohydrodynamic lubrication problem, cf. Szeri [73, p.410]. A fully coupled micro-macro simulation strategy, where the coupling between microscopic and macroscopic mechanisms can be clearly observed, is planned for a future work.

8.2 Anisotropic/Isotropic surfaces

Computing the global flux $\overline{\mathbf{q}}$ can deliver information on whether macroscopically isotropic or anisotropic flow conditions are present and hence whether the surface is deemed isotropic or anisotropic for the purposes of lubrication characterization. Isotropy exists when the input parameter $\overline{\mathbf{u}}_\beta^r$ or $\overline{\mathbf{g}}_\beta$, only one of them being active for arbitrary angles β , cause a flux $\overline{\mathbf{q}}_\beta$ such that

$$(\overline{\mathbf{u}}_\beta^r \text{ or } \overline{\mathbf{g}}_\beta) \parallel \overline{\mathbf{q}} \quad , \text{ and } \quad \|\overline{\mathbf{q}}\| = \text{const} \quad \forall \beta \quad \Rightarrow \quad \mathcal{S}_0^l \text{ isotropic} \quad (8.1)$$

holds. Anisotropy is characterized by

$$\exists \beta \quad (\overline{\mathbf{u}}_\beta^r \text{ or } \overline{\mathbf{g}}_\beta) \not\parallel \overline{\mathbf{q}} \quad , \text{ or } \quad \|\overline{\mathbf{q}}\| \neq \text{const} \quad \forall \beta \quad \Rightarrow \quad \mathcal{S}_0^l \text{ anisotropic} \quad (8.2)$$

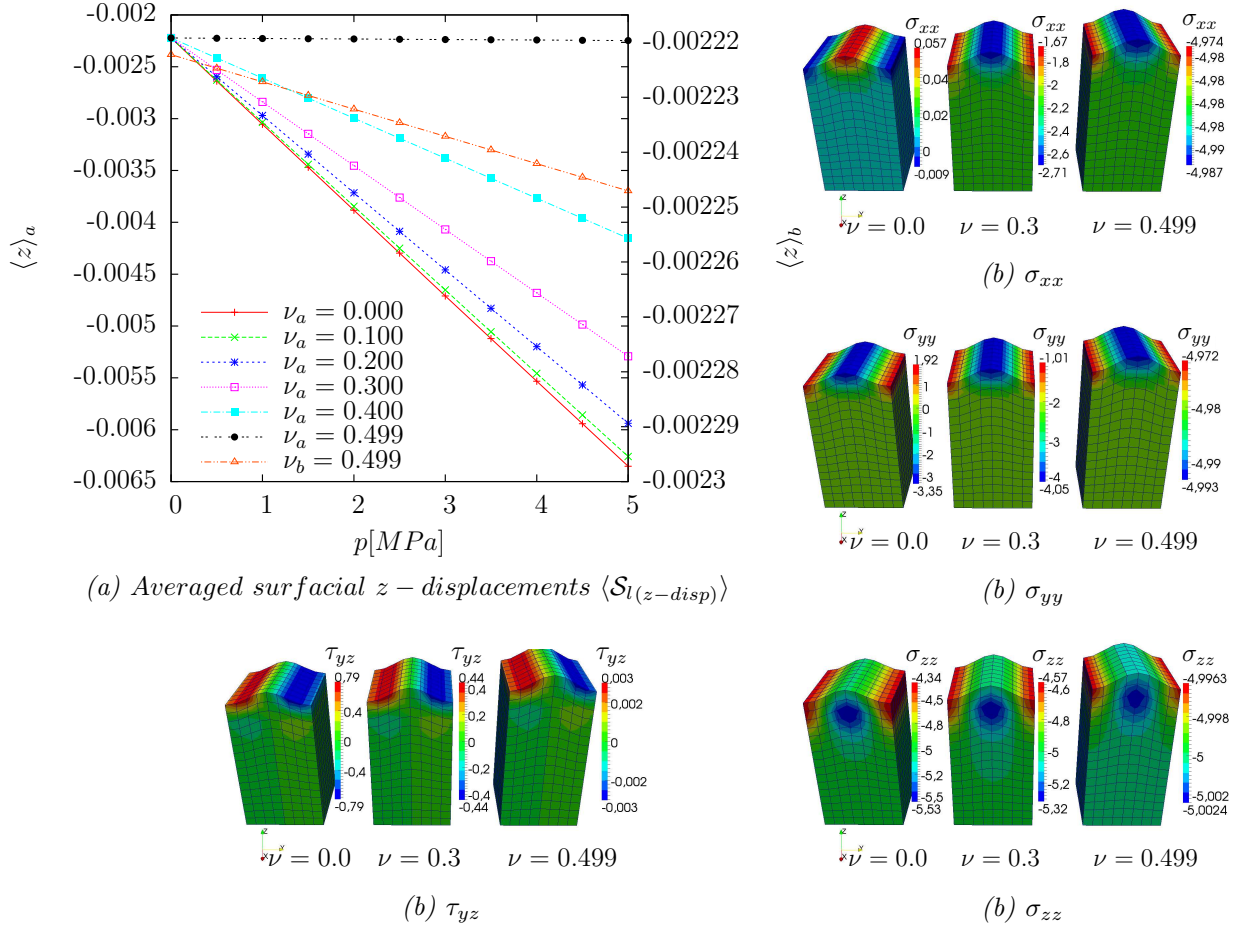


Figure 8.1: Influence of Poisson's ratio ν on: (a) surfacial z -displacements to be subject of an increasing pressure load p (poissons ratio $\nu = 0.499$ is plotted w.r.t. both axis of different ranges to clarify that locking does not occur) and (b) stress distribution to be subject of $\bar{p} = 5$ MPa

Therefore parameter studies with changing orientation of $\overline{\mathbf{u}}_\beta^r$ and $\overline{\mathbf{g}}_\beta$ have been carried out on two different surfaces (figure 8.2), where $\beta \in 0^\circ - 360^\circ$ was incremented in steps of 7.5° .

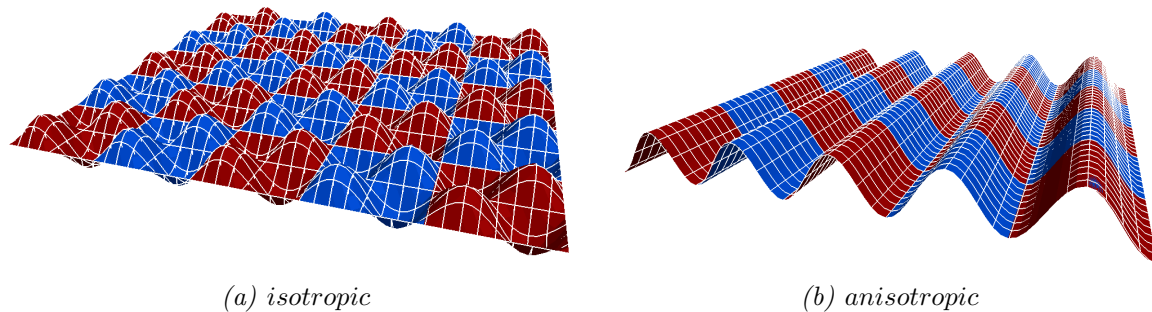


Figure 8.2: Isotropic and anisotropic surface. Amplitudes are scaled by a factor of five.

Figure 8.3 illustrates the macroscopic flux response $\overline{\mathbf{q}}$ for these studies. Here figures (a,b,d,e) in the first and second column are subject to macroscopic velocity $\overline{\mathbf{u}}_\beta^r$ and figures (c,f) in the third column are subject to the macroscopic pressure gradient $\overline{\mathbf{g}}_\beta$. The isotropic surface ((fig 8.2)_a) was applied to figures (a,b,c) in the first row whereas figures (d,e,f) in the second row are subject to the anisotropic surface ((fig 8.2)_b). Each cross in the plots relates the flux $\overline{\mathbf{q}}$ and its components to an input parameter $\overline{\mathbf{u}}_\beta^r$ or $\overline{\mathbf{g}}$. For the start angle of $\beta = 0^\circ$ the computed fluxes are in phase with $\overline{\mathbf{u}}_\beta^r$ ((fig 8.3)_{a,b,d,e}), but phase shifted by 180° for $\overline{\mathbf{g}}$ ((fig 8.3)_{c,f}). Moving inside a plot in counterclockwise direction with increments of 7.5° the viewer observes a circular flux response $\overline{\mathbf{q}}$ and uniformly distributed crosses in figure 8.3_{a,b,c} meaning that equation (8.1) is fulfilled, hence the surface is isotropic. Note that for isotropy the flux components $\overline{\mathbf{q}}^p$ and $\overline{\mathbf{q}}^c$ display the same characteristics as $\overline{\mathbf{q}}$. Reviewing figure 8.3_{d,e,f} an anisotropic response is observed via equation (8.2). Both the flux $\overline{\mathbf{q}}$ and its component $\overline{\mathbf{q}}^p$ have an elliptic and line shape, whereas $\overline{\mathbf{q}}^c$ remains isotropic (circular). For figure 8.3_f the COUETTE term $\overline{\mathbf{q}}^c$ vanishes such that $\overline{\mathbf{q}} = \overline{\mathbf{q}}^p$ causes anisotropy. Reducing the gap height \overline{h} restricts the flow and hence leads to a decrease in the flux magnitude for both isotropic and anisotropic surfaces, compare figure 8.3_{a,b,d,e}. Furthermore, an increase of ellipticity and hence anisotropy for an anisotropic *geometry* can be observed comparing figure 8.3_{d,e}.

A discussion of the macroscopic flux components $\overline{\mathbf{q}}^p$ and $\overline{\mathbf{q}}^c$ requires monitoring their microscopic counterparts \mathbf{q}^p and \mathbf{q}^c . Figures 8.4_{a,c} illustrate that the orientation of the COUETTE flow on both scales (i.e. $\overline{\mathbf{q}}^c$ and \mathbf{q}^c) remain parallel to the input velocity $\overline{\mathbf{u}}_\beta^r$ at all times. Hence the COUETTE term always causes an isotropic flux, which is clear from its constitutive form. The local flux \mathbf{q}^c changes

proportionally to the local gap height h (Eqn.(8.3)) which can be identified in equation (5.1), whereas its macroscopic equivalent remains constant for all angles β :

$$\|\mathbf{q}^c\| \propto h, \text{ if } \bar{\mathbf{u}}^r = \text{const} . \quad (8.3)$$

Due to the fact that $\bar{\mathbf{u}}^r = 0 \text{ mm/s}$ for plots in figure 8.4_{b,d} the COUETTE term vanishes ($\mathbf{q}^c = \bar{\mathbf{q}}^c = 0$) such that

$$\begin{aligned} \mathbf{q} &= \mathbf{q}^p \text{ and } \mathbf{q}^c = 0, \text{ for } \bar{\mathbf{g}} \neq 0 \text{ and } \bar{\mathbf{u}}^r = 0 \text{ and} \\ \bar{\mathbf{q}} &= \bar{\mathbf{q}}^p \text{ and } \bar{\mathbf{q}}^c = 0, \text{ for } \bar{\mathbf{g}} \neq 0 \text{ and } \bar{\mathbf{u}}^r = 0, \end{aligned} \quad (8.4)$$

hold. Flow deflection is caused by the POISEUILLE terms $\bar{\mathbf{q}}^p$ and \mathbf{q}^p depending on the pressure gradient \mathbf{g} as well the gap height h^3 and thus the surface microstructure. Arrows representing the Poiseuille fluxes \mathbf{q}^p and $\bar{\mathbf{q}}^p$ also help visualize pressure gradients. They always point from high pressure areas towards low pressure areas (figure 8.4).

8.3 Deformation gradient

The influence of the surfacial deformation gradient is investigated in this section. In matrix notation,

$$\bar{\mathbf{F}}^S = \mathbf{1} + \bar{\mathbf{H}}^S \quad , \quad [\bar{\mathbf{H}}^S] = \begin{bmatrix} h_{11}^S & h_{12}^S \\ h_{21}^S & h_{22}^S \end{bmatrix} \quad (8.5)$$

where the entries on the main diagonal h_{ii}^S stretch a surface, and hence the remaining entries h_{ij}^S , $i \neq j$ shear a surface, cf. (fig 8.5.)

For $h_{11}^S = h_{22}^S = (-0.2 \rightarrow 0.2)$ isotropy is preserved for velocity and pressure gradient driven computations, refer to figure 8.6. As a consequence of surfacial stretch roughness is flattened, and hence flux increases.

Solely varying the displacement component $h_{11}^S = (-0.2 \rightarrow 0.2)$ gives an anisotropic response. It can be observed for $h_{11}^S = -0.2$ in figure 8.7_b that $\bar{\mathbf{q}}^p$ has an elliptical shape. Its principal direction points towards 0° and causes an elliptical flux $\bar{\mathbf{q}}$ with principal direction pointing towards 90° . Applying a positive displacement gradient $h_{11}^S = 0.2$ (figure 8.7_a) orientation of both fluxes ($\bar{\mathbf{q}}^p$, $\bar{\mathbf{q}}$) turns about 90° . Additionally, an increase of flux from negative to positive displacement gradients can be seen due to an increasing surface.

For a pressure gradient $\bar{\mathbf{g}} = 0.1 \text{ MPa/mm}$ driven computation (figure 8.7_c) the flux $\bar{\mathbf{q}}$ keeps its principal directions towards 0° ($h_{11}^S = 0.2$) and hence it follows $\bar{\mathbf{q}}^p$ according to our observations in section 8.2 .

Finally, the effect of the shearing components are evaluated. This effect is not as dominant compared to stretching. Therefore, the values have been chosen larger, but remaining in a realistic deformation range, to show its influence on the anisotropic behaviour. Varying $h_{12}^S = 0.3 \rightarrow 0.9$ causes an increasing anisotropic flux response (figure 8.8_{a,b,c}). Further on the COUETTE flux \mathbf{q}^c principal direction moves from $\approx 30^\circ$ towards $\approx -30^\circ$ and hence the flux $\bar{\mathbf{q}}$ is shifted by 90° . Applying $h_{12}^S = h_{21}^S = 0.1 \rightarrow 0.7$ causes a stronger surface shrinking and also a strong elliptical response (figure 8.8_{d,e,f}). The principal direction of the flux $\bar{\mathbf{q}}$ points towards 45° . Pressure gradient \mathbf{g} induced fluxes are summarized in figure 8.9. Here, another data representation was chosen to elucidate shearing influence. Again a shrinking surface can be observed for solely varied parameters $h_{i,j}^S$, $i, j \in 1, 2$ and $i \neq j$ as well a moderate anisotropy. A stronger response is observed for shearing $h_{12}^S = h_{21}^S$ at the same time.

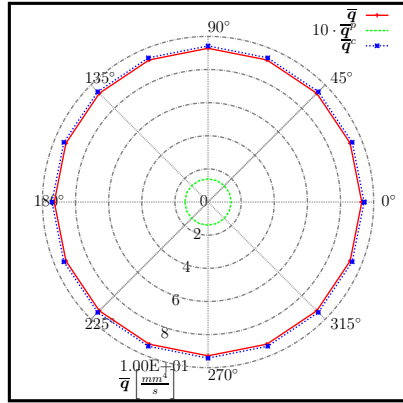
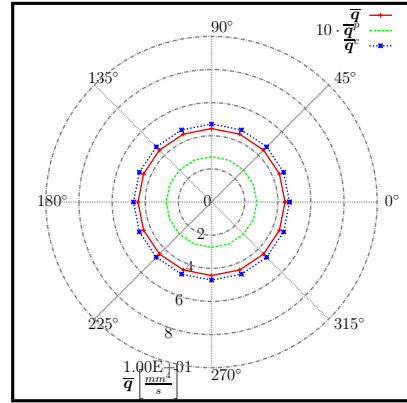
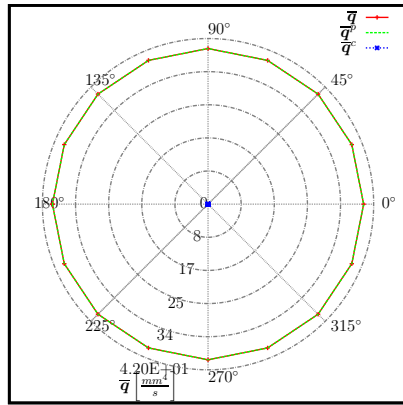
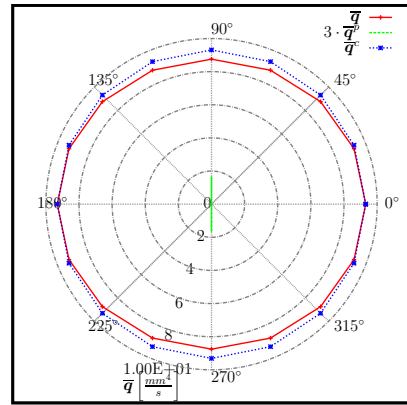
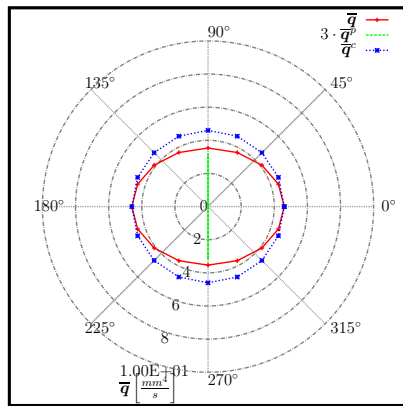
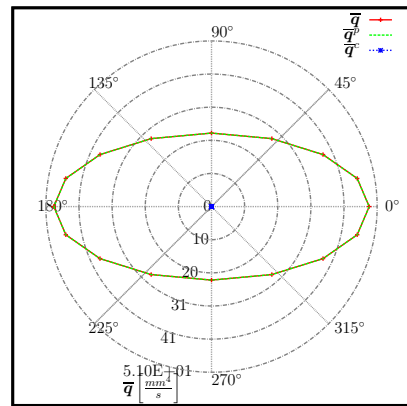
(a) $\bar{h} = 0.1$ mm(b) $\bar{h} = 0.05$ mm(c) $\bar{h} = 0.05$ mm(d) $\bar{h} = 0.1$ mm(e) $\bar{h} = 0.05$ mm(f) $\bar{h} = 0.05$ mm

Figure 8.3: Influence of decreasing gap height \bar{h} on global flux orientation and magnitude on (a, b, c) *isotropic* surface and (d, e, f) *anisotropic* surface. For subfigure (c, f) $\bar{\mathbf{u}}^r = 0$ mm/s and $\bar{\mathbf{g}} = 0.1$ MPa/mm were applied. All other results have been computed using $\bar{\mathbf{u}}^r = 2356$ mm/s and $\bar{\mathbf{g}} = 0$ MPa/mm

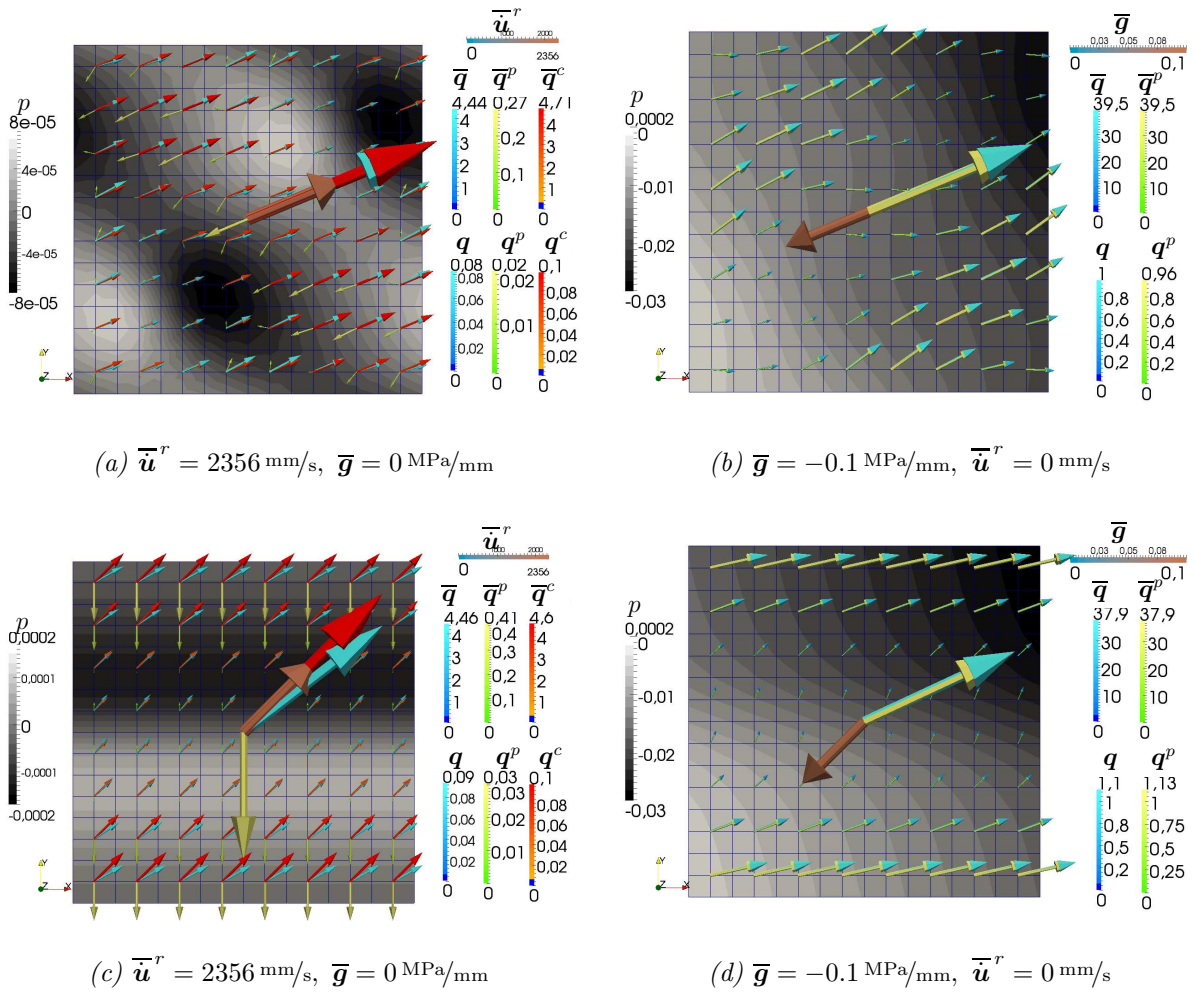


Figure 8.4: Computational results of local flux, pressure distribution (q, q^p, q^c, p) and total flux ($\bar{q}, \bar{q}^p, \bar{q}^c$) on (a,b) isotropic surface and (c,d) anisotropic surface, q.v. figure 8.2. Both input parameters \bar{u}^r and \bar{g} are applied to (a,b) at an angle of $\beta = 22.5^\circ$ and to (c,d) at an angle of $\beta = 45^\circ$ with respect to x-axis. The surface color shows the local pressure distribution p in the lubricant flow. High pressures are coloured white and low pressures are coloured black. Arrows represent the magnitude and orientation of input parameters \bar{u}^r, \bar{g} and output variables q, \bar{q} and its components. They are clearly allocated by the legend. The input and macroscopic output quantities, and hence their corresponding arrows are centered. Local fluxes are centered on their corresponding elements.

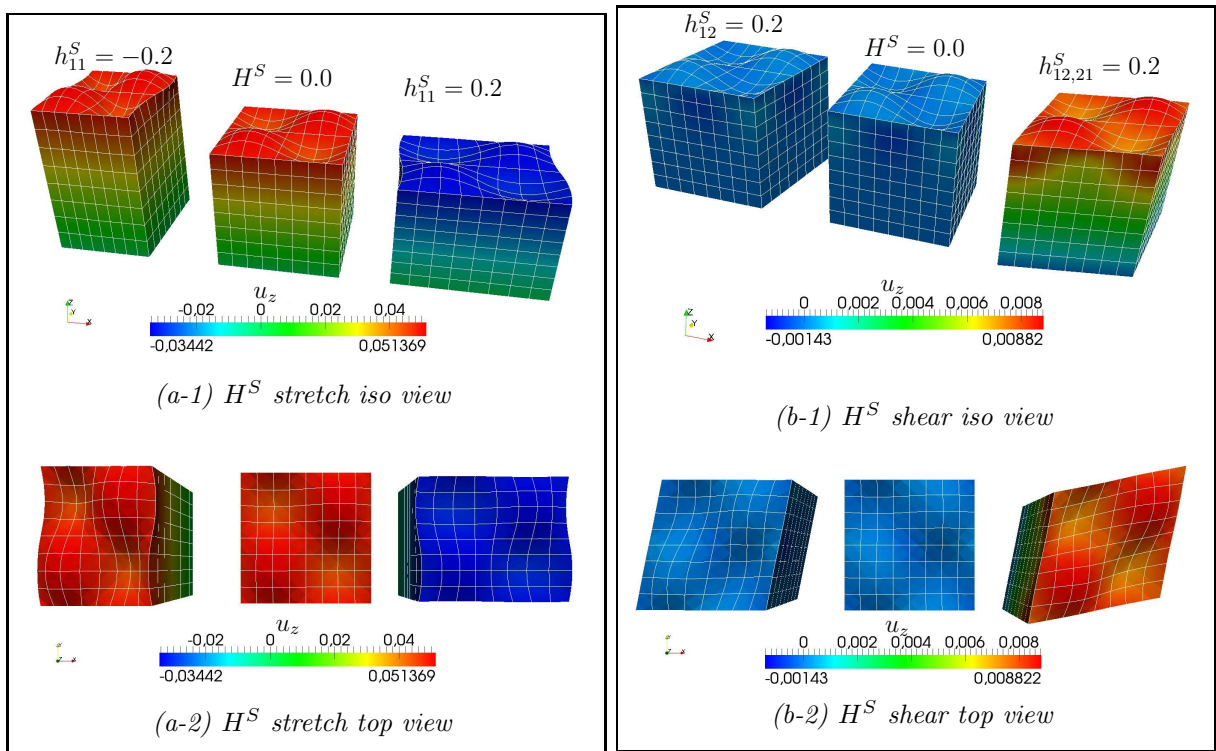


Figure 8.5: Mechanical phase undergoing a) a stretch into h_{11}^S direction and b) a shear into $h_{12,21}^S$ direction and being subject to periodic boundary conditions.

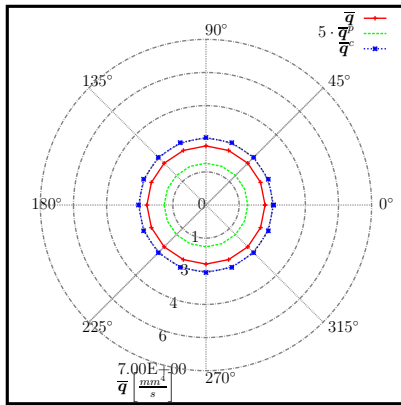
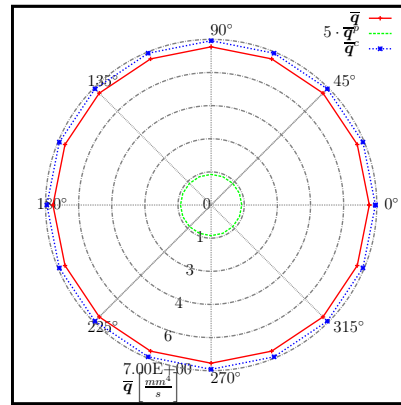
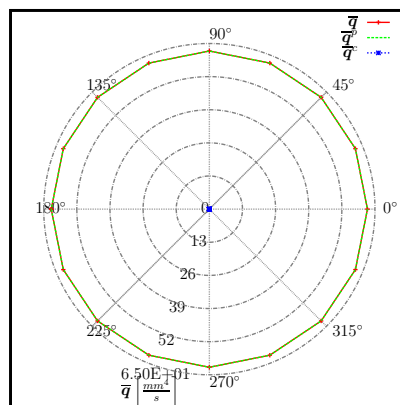
(a) $h_{11}^S = h_{22}^S = -0.2$ (b) $h_{11}^S = h_{22}^S = 0.2$ (c) $h_{11}^S = h_{22}^S = 0.2$

Figure 8.6: Isotropic response of an isotropic surface undergoing uniform stretch into h_{11}^S and h_{22}^S direction: a,b) $\bar{\mathbf{u}}^r = 2356 \text{ mm/s}$, $\bar{\mathbf{g}} = 0 \text{ MPa/mm}$ and c) $\bar{\mathbf{g}} = 0.1 \text{ MPa/mm}$, $\bar{\mathbf{u}}^r = 0 \text{ mm/s}$.

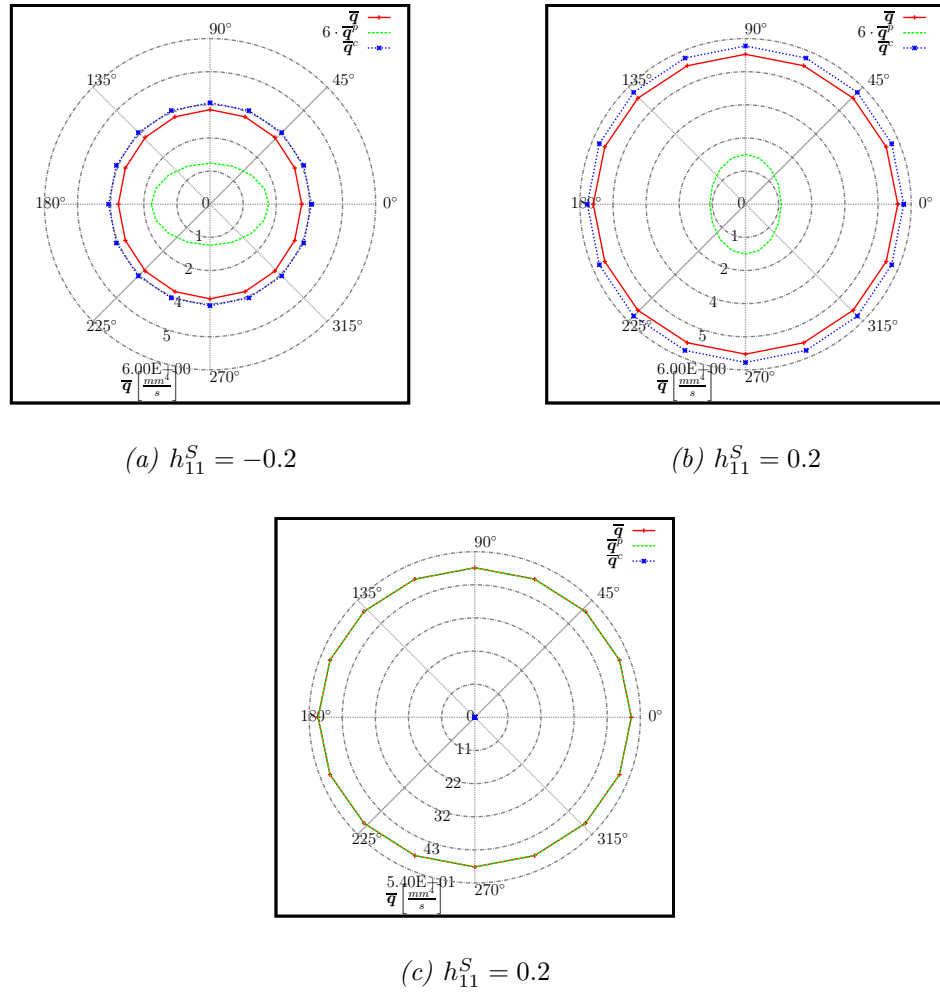


Figure 8.7: Anisotropic response of an isotropic surface stretched along the 0° axis: a,b) $\bar{\mathbf{u}}^r = 2356 \text{ mm/s}$, $\bar{\mathbf{g}} = 0 \text{ MPa/mm}$ and c) $\bar{\mathbf{g}} = 0.1 \text{ MPa/mm}$, $\bar{\mathbf{u}}^r = 0 \text{ mm/s}$

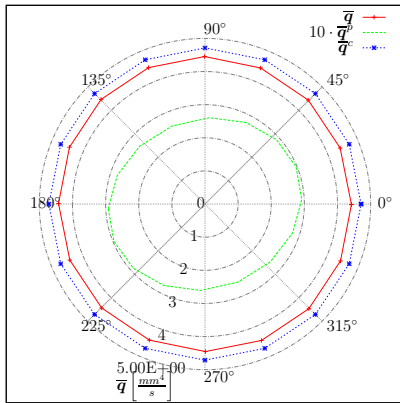
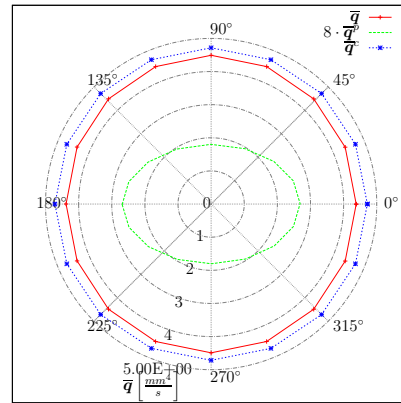
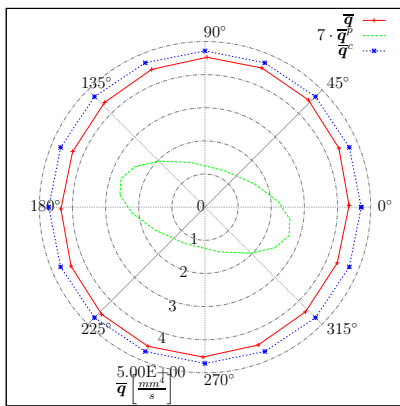
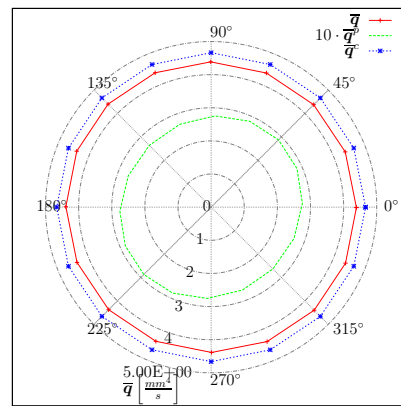
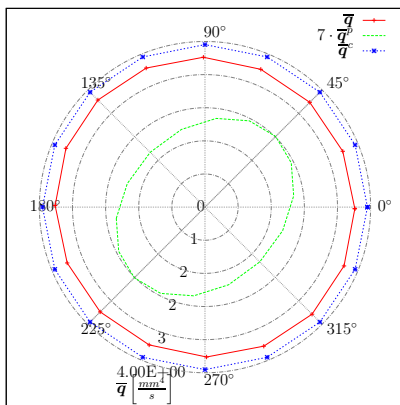
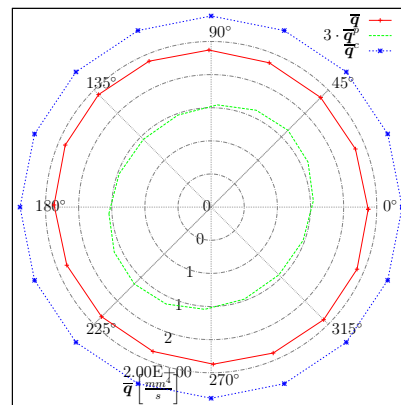
(a) $h_{12}^S = 0.3$ (b) $h_{12}^S = 0.6$ (c) $h_{12}^S = 0.9$ (d) $h_{12}^S,_{21} = 0.1$ (e) $h_{12}^S,_{21} = 0.4$ (f) $h_{12}^S,_{21} = 0.7$

Figure 8.8: Anisotropic flow behavior for surfacial shearing with $\bar{u}^r = 2356 \text{ mm/s}$, $\bar{q} = 0 \text{ MPa/mm}$.

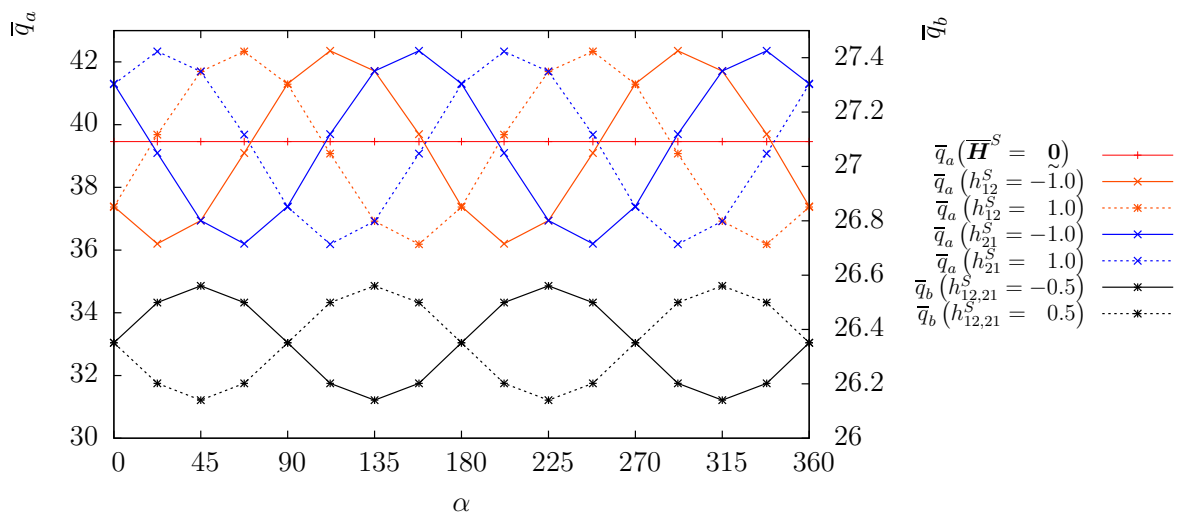


Figure 8.9: Anisotropic flow behaviour for surficial shearing with $\bar{\mathbf{u}}^r = 0$ mm/s, $\bar{\mathbf{g}} = 0.1$ MPa/mm. Quantities denoted by \bar{q}_a refer to the left axis and \bar{q}_b refer to the right axis, respectively.

Chapter 9

Conclusion

In order to predict the macroscopic response of microscopically rough lubricated interfaces in the large deformation regime, a three-dimensional computational homogenization approach was presented, closely following homogenization techniques for rigid and infinitesimally deforming surfaces. The approach is based on proposing a lubrication formulation governed by the classical REYNOLDS equation on the micro scale, in agreement with earlier approaches, but extracting the macroscopic flux within a micromechanical testing procedure.

While the problem remains coupled on the macroscale, the macroscopic flow control parameters are projected onto the micromechanical test sample as boundary conditions such that a *two-phase micromechanical test* was induced. An effective numerical treatment of a *mechanical phase* followed by a *lubrication phase* is achieved, which was demonstrated by comparing computational times of a lubrication problem solved in a decoupled and coupled way. This two-phase split is exact to within a separation of scales assumption, as in multiphysics homogenization strategies for heterogeneous media. A parameter study comparing sample size effects (sec 7) for both the two-phase split and a classical coupled computation shows that the two-phase split complies with a fundamental postulate of homogenization - that sample size may not influence the homogenized result.

The numerical results presented show that within the interface the fluid flow is strongly influenced by the surface geometry which was found to be significantly altered by the surfacial deformation. The surfacial deformation, in turn, is significantly influenced on the macroscale by the gap height and the pressure. Flux \bar{q} changes stronger with varying the gradient \bar{g} than by means of varying the velocity \bar{u}^r as can be seen in section 8. Qualitative observations could be made for these parameters and have been found to be coherent with practical experience.

A validation with experimental results should be conducted but would be premature due to several omitted effects which should be explored for the finite de-

formation regime. Throughout the interface effects like temperature dependence, asperity deformation induced by surface shearing and hence the lubricant tangential friction are present. In particular the lubricant tangential friction as shown by Stupkiewicz and Maciniszyn [72], Yang and Laursen [86] yields to both asperity and flat surface deformations leading to qualitative changes of the pressure profile, such that this effect needs to be considered.

Another shortcoming of the present REYNOLDS equation, is that BARUS equation only holds for moderate pressures. In order to extend the applicability of REYNOLDS equation to the high pressure regime BARUS equation needs to be replaced by ROELANDS formula, see Hamrock et al. [33]. Furthermore, the REYNOLDS equation will be violated for increasing amplitudes or little gap heights such that NAVIER-STOKES equation needs to be solved [25].

Real roughness profiles also need to be investigated. Due to the random characteristics of real surfaces, sample size effects would play a role. Randomness effects can be alleviated by complementing surface averaging with ensemble averaging combined with sample enlargement, albeit at the expense of high computational cost. Applying periodic boundary conditions on real rough surfaces would be an important step to achieve feasible computational times. Here a promising approach was suggested by Uchida et al. [81].

The contact of the adjacent surfaces would complete the present investigations - with one surface being rough and the adjacent surface chosen flat - on rough surfaces, where the present ALE setting can be used for normal contact formulations. However, taking tangential friction into account a time dependent formulation regarding material time history becomes mandatory [87]. In order to prescribe surface to surface contact the penalty formulation or, due to the special LAGRANGIAN type lubrication framework [eqn (5.30)], the LAGRANGE multiplier method seems to be suited, see appendix A. Here the LAGRANGE multiplier λ can be interpreted as a contact pressure Δp . The identification of the boundary between the lubrication and contact zones remains as a challenge. Since fluid is absent within contact regions, flow across the boundary between lubrication domain and contact domain need to be constrained to zero. In order to apply the method to real interface problems both surfaces needs to be rough, demanding a transient computation on the micro scale throughout all lubrication regimes.

Finally, a key future investigation is the realization of the coupling to the macroscale by means of numerical tangent computations enabling the use of implicit solution schemes and hence a reduction of computational times within a microscale setting. Moreover an efficient and simple way of distributing the microscale computations and hence save computational times towards this purpose is suggested in appendix B.

Appendix A

Contact Algorithms

In order to compare the population of stiffness matrices for different frictionless contact algorithms to the lubrication framework stiffness matrix [eqn (5.30)], two algorithms are introduced briefly, namely the penalty method and the LAGRANGE multiplier method. For both methods the normal contact parts are developed with

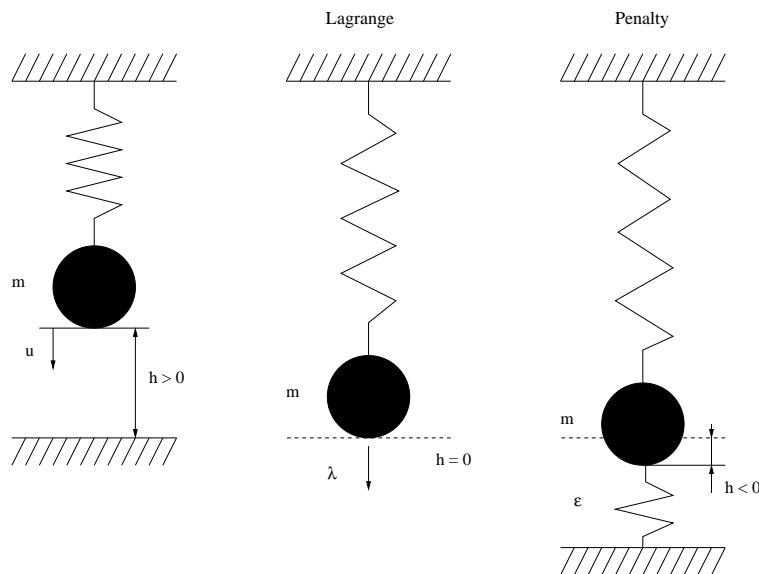


Figure A.1: Mass spring system demonstrating the working principle of the LAGRANGE Multiplier Method and the Penalty Method.

respect to the lubrication framework, such that a contact search is unnecessary because the gap height h is used.

Penalty Method

The constraint formulation reads

$$\text{if } \begin{cases} h < 0: \Pi_C^P = \frac{1}{2} \int_{\Gamma} \epsilon (h)^2 \, da \\ h \geq 0: \Pi_C^P = 0 \\ \epsilon > 0, \end{cases} \quad (\text{A.1})$$

such that the variational formulation evolves to

$$C_C^P = \int_{\Gamma} \epsilon h \delta h \, da, \quad (\text{A.2})$$

with

$$h = (\mathbf{x}^+ - \mathbf{x}^-) \cdot \mathbf{n}^m \quad (\text{A.3})$$

and its variation reads

$$\delta h = (\widehat{\boldsymbol{\eta}}^{u^+} - \widehat{\boldsymbol{\eta}}^{u^-}) \cdot \mathbf{n}^m. \quad (\text{A.4})$$

Linearising equation (A.2) leads to

$$C_C^P = \int_{\Gamma_C} (\epsilon \Delta h \delta h + \overbrace{\epsilon h \Delta \delta h}^{=0}) \, da \quad (\text{A.5})$$

with

$$\Delta h = (\boldsymbol{\Delta u}^+ - \boldsymbol{\Delta u}^-) \cdot \mathbf{n}^m. \quad (\text{A.6})$$

Finally, discretizing equation (A.5) leads to

$$C_C^{P\pm} = \sum_{I=1}^{n_c} (\pm \widehat{\boldsymbol{\eta}}_{Ir}^{\pm}) \sum_{J=1}^{n_c} \int_{\Gamma_C} \epsilon N_I N_J n_{Ir}^m n_{Js}^m \, da (\pm \Delta u_{Js}^{\pm}), \quad (\text{A.7})$$

where nodes $I, J \in 1, 2, 3, 4$ denote lower surface quantities $(-\widehat{\boldsymbol{\eta}}_I^{u^-}, -\boldsymbol{\Delta u}_J^-)$ and nodes $I, J \in 9, 10, 11, 12$ denotes upper surface quantities $(\widehat{\boldsymbol{\eta}}_I^{u^+}, \boldsymbol{\Delta u}_J^+)$ in case of making use of linear shape functions. Previous equation can be introduced into the lubrication linear system of equations [eqn (5.30)] reading

$$\begin{pmatrix} \frac{\partial \mathcal{G}^{C-}}{\partial \mathbf{n}^-} \frac{\partial \mathbf{n}^-}{\partial \mathbf{u}^-} + \frac{\partial C_c^P}{\partial \mathbf{u}^-} & \frac{\partial C_c^P}{\partial \mathbf{u}^+} & \frac{\partial \mathcal{G}^{C-}}{\partial p^m} \\ \frac{\partial C_c^P}{\partial \mathbf{u}^-} & \frac{\partial \mathcal{G}^{C+}}{\partial \mathbf{n}^+} \frac{\partial \mathbf{n}^+}{\partial \mathbf{u}^+} + \frac{\partial C_c^P}{\partial \mathbf{u}^+} & \frac{\partial \mathcal{G}^{C+}}{\partial p^m} \\ \frac{\partial \mathcal{G}^F}{\partial h} \frac{\partial h}{\partial \mathbf{u}^-} & \frac{\partial \mathcal{G}^F}{\partial h} \frac{\partial h}{\partial \mathbf{u}^+} & \frac{\partial \mathcal{G}^F}{\partial p^m} + \frac{\partial \mathcal{G}^F}{\partial \mu} \frac{\partial \mu}{\partial p^m} + \frac{\partial \mathcal{G}^{Cav}}{\partial p^m} \end{pmatrix} \begin{pmatrix} \Delta \mathbf{u}^- \\ \Delta \mathbf{u}^+ \\ \Delta p^m \end{pmatrix} = - \begin{pmatrix} \mathcal{G}^{C-} + C_c^{P-} \\ \mathcal{G}^{C+} + C_c^{P+} \\ \mathcal{G}^F + \mathcal{G}^{Cav} \end{pmatrix} \quad (\text{A.8})$$

Lagrange Method

The potential reads

$$\Pi_C^L = \int_{\Gamma_C} \lambda \delta h \, da \quad (\text{A.9})$$

leading to the constraint formulation

$$C_C^L = \delta \Pi_C^L = \int_{\Gamma_C} (\lambda \delta h + \delta \lambda h) \, da \quad (\text{A.10})$$

via variation of equation (A.9). Subsequently linearising above equation gives

$$C_C^L = \int_{\Gamma_C} \left(\Delta \lambda \delta h + \lambda \Delta \delta h + \Delta \delta \lambda h + \delta \lambda \Delta h \right) \, da, \quad (\text{A.11})$$

with

$$\delta \lambda = \widehat{\eta}^p, \quad \Delta \lambda = \Delta p \quad (\text{A.12})$$

and Δh and δh according equations (A.6) and (A.4). Discretizing leads to

$$C_C^L = \sum_I (\pm \widehat{\eta}_{I_r}^{u^\pm}, \widehat{\eta}_I^p) \sum_J \int_{\Gamma_C} N_I N_J (\mathbf{n}_{I_r}^m + \mathbf{n}_{J_s}^m) \, da (\pm \Delta \mathbf{u}_{J_s}^\pm, \Delta p_j) \quad (\text{A.13})$$

This might be introduced into equation (5.30) populating the red colored entries

$$\begin{pmatrix} \frac{\partial \mathcal{G}^{C-}}{\partial \mathbf{n}^-} \frac{\partial \mathbf{n}^-}{\partial \mathbf{u}^-} & 0 & \frac{\partial \mathcal{G}^{C-}}{\partial p^m} + \frac{\partial C_c^{L-}}{\partial p^m} \\ 0 & \frac{\partial \mathcal{G}^{C+}}{\partial \mathbf{n}^+} \frac{\partial \mathbf{n}^+}{\partial \mathbf{u}^+} & \frac{\partial \mathcal{G}^{C+}}{\partial p^m} + \frac{\partial C_c^{L+}}{\partial p^m} \\ \frac{\partial \mathcal{G}^F}{\partial h} \frac{\partial h}{\partial \mathbf{u}^-} + \frac{\partial C_c^{L-}}{\partial \mathbf{u}^-} & \frac{\partial \mathcal{G}^F}{\partial h} \frac{\partial h}{\partial \mathbf{u}^+} + \frac{\partial C_c^{L+}}{\partial \mathbf{u}^+} & \frac{\partial \mathcal{G}^F}{\partial p^m} + \frac{\partial \mathcal{G}^F}{\partial \mu} \frac{\partial \mu}{\partial p^m} + \frac{\partial \mathcal{G}^{Cav}}{\partial p^m} \end{pmatrix} \begin{pmatrix} \Delta \mathbf{u}^- \\ \Delta \mathbf{u}^+ \\ \Delta p^m \end{pmatrix} = - \begin{pmatrix} \mathcal{G}^{C-} + C_c^{L-} \\ \mathcal{G}^{C+} + C_c^{L+} \\ \mathcal{G}^F + \mathcal{G}^{Cav} + C_c^{Lm} \end{pmatrix} \quad (\text{A.14})$$

Appendix B

Distributed computing

For multiscale problems with a large number of independent microscale problems, distributed and hence parallel computing reduces the solution time tremendously. AMDAHL's law [6] estimates the **speedup** $S(n^p)$

$$S(n^p) = \frac{T(1)}{T(n^p)}, \quad (\text{B.1})$$

being the time ratio of a serial $T(1)$ and parallel/distributed $T(n^p)$ computation, with n^p denoting the number of processors in use. Hereby the computation time of $T(n^p)$ can be distinguished according to serial t^s , parallel t^c and communication time T_C leading to

$$T(n^p) = t^s + \overbrace{\frac{(1-t^s)}{n^p}}^{t^p:=} + T_c(n^p)(n^p - 1) \quad (\text{B.2})$$

and substituting

$$f = \frac{t^s}{t^s + t^p} \quad \text{and} \quad r = \frac{T_c(n^p)}{T(1)}, \quad (\text{B.3})$$

such that equation (B.1) reads

$$S(n^p) = \frac{1}{f + \frac{(1-f)}{n^p} + r(n^p - 1)}. \quad (\text{B.4})$$

Within a parallel/distributed computation the **efficiency** $\epsilon(n^p)$

$$\epsilon(n^p) = \frac{S(n^p)}{n^p}, \quad (\text{B.5})$$

states the averaged work-load of a processor.

In case of the micromechanical test procedure, the child problems are independent of other processes, and hence distributing and parallel solving can be realized in a very efficient way. It is achieved by making use of the resource management system Torque¹ which controls batch jobs and distributed computing resources in an automated way. An extensive and more detailed overview on cluster computing can be found in [8, 19, 20].

Torque runs on both distributed network computers or dedicated cluster systems. Distributed computing as shown in figure B.1 gets very simple, if a cluster is setup such that all nodes² access the same file system (shared storage) and a resource manager organizes the job execution according to the *FIFO*³ principle.

¹<http://www.clusterresources.com/products/torque-resource-manager.php>

²Denotes a computer in a cluster.

³First in first out.

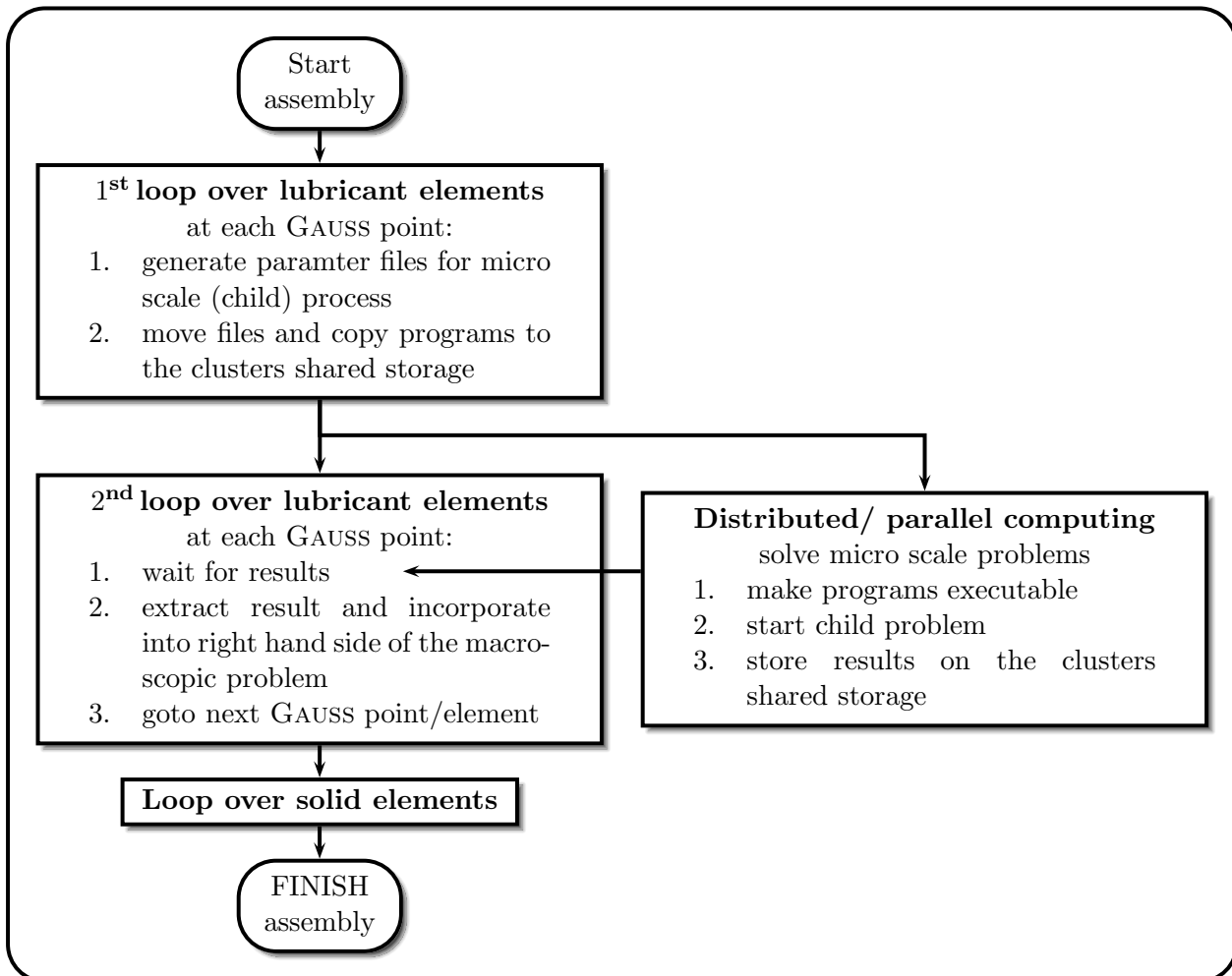


Figure B.1: Flowchart on the assembly of the right hand side vector of a macro scale problem. Here the members of the right hand side vector are computed from micro scale computations, which are distributed to different nodes and CPU's, being solved in a parallel way.

Bibliography

- [1] Almqvist, A. and Dasht, J. (2006). The homogenization process of the Reynolds equation describing compressible liquid flow. *Tribology International*, 39:994–1002.
- [2] Almqvist, A., Essel, E., Fabricius, J., and Wall, P. (2008). Reiterated homogenization applied in hydrodynamic lubrication. *Proceedings of the Institution of Mechanical Engineers, Part J: Journal of Engineering Tribology*, 222(7):827–841.
- [3] Almqvist, A., Essel, E., Persson, L., and Wall, P. (2007a). Homogenization of the unstationary incompressible Reynolds equation. *Tribology International*, 40(9):1344–1350.
- [4] Almqvist, A., Lukkassen, D., Meidell, A., and Wall, P. (2007b). New concepts of homogenization applied in rough surface hydrodynamic lubrication. *International Journal of Engineering Science*, 45(1):139–154.
- [5] Altenbach, J. and Altenbach, H. (1994). *Einführung in die Kontinuumsmechanik*. Teubner.
- [6] Amdahl, G. (1967). Validity of the single processor approach to achieving large scale computing capabilities. In *Proceedings of the April 18-20, 1967, spring joint computer conference*, pages 483–485. ACM.
- [7] Bakhvalov, N. and Panasenko, G. (1989). *Homogenisation: averaging processes in periodic media*. Kluwer.
- [8] Bauke, H. and Mertens, S. (2006). *Cluster computing*. Springer X.system.Press.
- [9] Bayada, G. and Chambat, M. (1989). Homogenization of the Stokes system in a thin film flow with rapidly varying thickness. *Modélisation mathématique et analyse numérique*, 23(2):205–234.

- [10] Bayada, G., Martin, S., and Vázquez, C. (2005). An average flow model of the Reynolds roughness including a mass-flow preserving cavitation model. *Journal of Tribology*, 127:793–802.
- [11] Bayada, G., Martin, S., and Vázquez, C. (2006). Micro-roughness effects in (elasto) hydrodynamic lubrication including a mass-flow preserving cavitation model. *Tribology International*, 39(12):1707–1718.
- [12] Bensoussan, A., Lions, J., and Papanicolaou, G. (1978a). *Asymptotic analysis for periodic structures*, volume 5. North Holland.
- [13] Bensoussan, A., Lions, J. L., and Papanicolaou, G. (1978b). *Asymptotic Analysis for Periodic Structures*. North-Holland.
- [14] Bergenrienäker, K.-P. (2011). Hydrostatisch-hydrodynamisches gleitlagerkonzept für die propellerlagerung in pod-antrieben großer schiffe. *VDI-Berichte/VDI-Tagungsbände*, (2147):243–254.
- [15] Bohan, M., Fox, I., Claypole, T., and Gethin, D. (2003). Influence of non-Newtonian fluids on the performance of a soft elasto-hydrodynamic lubrication contact with surface roughness. *Proceedings of the Institution of Mechanical Engineers, Part J: Journal of Engineering Tribology*, 217(6):447–459.
- [16] Braess, H. and Seiffert, U. (2007). *Vieweg Handbuch Kraftfahrzeugtechnik*. Vieweg+ Teubner.
- [17] Braess, H. and Wriggers, P. (2000). Arbitrary Lagrangian Eulerian finite element analysis of free surface flow. *Computer Methods in Applied Mechanics and Engineering*, 190(1-2):95 – 109.
- [18] Buscaglia, G., Ciuperca, I., and Jai, M. (2007). On the optimization of surface textures for lubricated contacts. *Journal of Mathematical Analysis and Applications*, 335(2):1309–1327.
- [19] Buyya, R. e. a. (1999a). *High Performance Cluster Computing: Architectures and Systems, Volume 1*. Prentice Hall.
- [20] Buyya, R. e. a. (1999b). *High Performance Cluster Computing: Programming and Applications, Volume 2*. Prentice Hall.
- [21] Charnes, A., Osterle, F., and Saibel, E. (1952). On the energy equation for fluid-film lubrication. In [23], pages 133–136.
- [22] Cioranescu, D. and Donato, P. (1999). *An introduction to homogenization*. Oxford University Press New York.

- [23] Cope, W. (1949). The hydrodynamical theory of film lubrication. *Proceedings of the Royal Society of London. Series A, Mathematical and Physical Sciences*, 197(1049):201–217.
- [24] Curnier, A. and Taylor, R. L. (1982). A thermomechanical formulation and solution of lubricated contacts between deformable solids. *Journal of Lubrication Technology*, 104:109–117.
- [25] de Kraker, A., van Ostayen, R. A. J., and Rixen, D. J. (2010). Development of a texture averaged Reynolds equation. *Tribology International*, 43:2100–2109.
- [26] Donea, J., Giuliani, S., and Halleux, J. (1982). An arbitrary Lagrangian-Eulerian finite element method for transient dynamic fluid-structure interactions. *Computer Methods in Applied Mechanics and Engineering*, 33(1-3):689 – 723.
- [27] Dowson, D. (1995). Elastohydrodynamic and micro-elastohydrodynamic lubrication. *Wear*, 190(2):125–138.
- [28] Elrod, H. (1979). A general theory for laminar lubrication with Reynolds roughness. *ASME, Transactions, Journal of Lubrication Technology*, 101:8–14.
- [29] Elrod, H. (1981). A cavitation algorithm. *ASME J. Lubr. Technol*, 103(3):350–354.
- [30] Ervin, R. D. and Balderas, L. (1990). Hydroplaning with lightly-loaded truck tires. Technical Report UMTRI-90-6, Transportation Research Institute, The University of Michigan.
- [31] Fabricius, J. (2008). *Homogenization Theory with Applications in Tribology*. PhD thesis, Luleå University of Technology.
- [32] Fung, Y. C. (1993). *Biomechanics: Mechanical Properties of Living Tissues*. Springer, 2nd edition.
- [33] Hamrock, B., Schmid, S., and Jacobson, B. (2004). *Fundamentals of fluid film lubrication*. CRC.
- [34] Haupt, P. (2002). *Continuum Mechanics and Theory of Materials*. Springer.
- [35] Heinrich, J. C. and Zienkiewicz, O. C. (1977). Quadratic finite element schemes for two-dimensional convective-transport problems. *International Journal for Numerical Methods in Engineering*, 11(12):1831–1844.

- [36] Heywood, J. (1988). *Internal combustion engine fundamentals*. McGraw-Hill New York.
- [37] Hill, R. (1972). On constitutive macro-variables for heterogeneous solids at finite strain. *Proceedings of the Royal Society of London. A. Mathematical and Physical Sciences*, 326(1565):131.
- [38] Hirt, C. W., Amsden, A. A., and Cook, J. L. (1974). An arbitrary Lagrangian-Eulerian computing method for all flow speeds. *Journal of Computational Physics*, 14(3):227 – 253.
- [39] Holzapfel, G. A. (2000). *Nonlinear Solid Mechanics A Continuum Approach For Engineering*. Wiley.
- [40] Jackson, R. L. (2010). A scale dependent simulation of liquid lubricated textured surfaces. *Journal of Tribology*, 132:022001.
- [41] Jaffar, M. (2000). A numerical solution for a soft line elastohydrodynamic lubrication contact problem with sinusoidal roughness using the Chebyshev polynomials. *Proceedings of the Institution of Mechanical Engineers, Part C: Journal of Mechanical Engineering Science*, 214(5):711–718.
- [42] Jai, M. and Bou-Said, B. (2002). A comparison of homogenization and averaging techniques for the treatment of roughness in slip-flow-modified Reynolds equation. *Journal of Tribology*, 124:327.
- [43] Kane, M. and Bou-Said, B. (2004). Comparison of homogenization and direct techniques for the treatment of roughness in incompressible lubrication. *Journal of Tribology*, 126:733.
- [44] Kane, M. and Bou-Said, B. (2005). A study of roughness and non-newtonian effects in lubricated contacts. *Journal of Tribology*, 127:575.
- [45] Kane, M. and Do, T. (2006). A contribution of elastohydrodynamic lubrication for estimation of tire-road friction in wet conditions. In *Proceedings of the International Conference on Tribology, Parma, Italy, September 20-22 2006: AITC-AIT 2006*.
- [46] Khonsari, M. and Booser, E. (2008). *Applied tribology: bearing design and lubrication*, volume 14. John Wiley & Sons Inc.
- [47] Klein, B. (2010). *FEM: Grundlagen und Anwendungen der Finite-element-methode im Maschinen-und Fahrzeugbau*. Vieweg+Teubner.

- [48] Krause, F., Franke, H., and Gausemeier, J. (2007). *Innovationspotenziale in der Produktentwicklung*. Hanser Verlag.
- [49] Larsson, R. (2009). Modelling the effect of surface roughness on lubrication in all regimes. *Tribology International*, 42(4):512–516.
- [50] Lewis, R., Gallardo-Hernandez, E. A., Hilton, T., and Armitage, T. (2009). Effect of oil and water mixtures on adhesion in the wheel/rail contact. *Proc. IMechE Part F: J. Rail and Rapid Transit*, 223:275–283.
- [51] Lukkassen, D., Meidell, A., and Wall, P. (2007). Bounds on the effective behavior of a homogenized generalized Reynolds equation. *Journal of Function Spaces and Applications*, 5:133–150.
- [52] Mitsuya, Y. and Fukui, S. (1986). Stokes Roughness Effects on Hydrodynamic Lubrication. Part I—Comparison Between Incompressible and Compressible Lubricating Films. *Journal of Tribology*, 108:151.
- [53] Möller, H. (1997). Finite elemente in der automobilentwicklung. *Spektrum der Wissenschaft (Deutsche Ausgabe von Scientific American)*, pages 104–105.
- [54] Patir, N. and Cheng, H. (1978). An average flow model for determining effects of three-dimensional roughness on partial hydrodynamic lubrication. *ASME, Transactions, Journal of Lubrication Technology*, 100:12–17.
- [55] Patir, N. and Cheng, H. (1979). Application of average flow model to lubrication between rough sliding surfaces. *ASME Journal of Lubrication Technology*, 101(2):220–230.
- [56] Persson, B. (2000). *Sliding friction: physical principles and applications*, volume 1. Springer Verlag.
- [57] Persson, B. N. J. (2010). Fluid dynamics at the interface between contacting elastic solids with randomly rough surfaces. *Journal of Physics: Condensed Matter*, 22:265004.
- [58] Rabinowicz, E. (1995). *Friction and Wear of Materials*. John Wiley & Sons, 2nd edition.
- [59] Rajagopal, K. and Szeri, A. (2003). On an inconsistency in the derivation of the equations of elastohydrodynamic lubrication. *Proceedings of the Royal Society of London. Series A: Mathematical, Physical and Engineering Sciences*, 459(2039):2771.

- [60] Rannacher, R. and Stein, E. (1997). Finite elemente: die Ideen. *Spektrum der Wissenschaft*, 20(3).
- [61] Reynolds, O. (1886). On the theory of lubrication and its application to Mr. Beauchamp Tower's experiments, including an experimental determination of the viscosity of olive oil. *Philosophical Transactions of the Royal Society of London*, 177:pp. 157–234.
- [62] Sahlin, F., Almqvist, A., Larsson, R., and Glavatskih, S. (2007). Rough surface flow factors in full film lubrication based on a homogenization technique. *Tribology International*, 40(7):1025–1034.
- [63] Sahlin, F., Larsson, R., Almqvist, A., Lugt, P., and Marklund, P. (2010a). A mixed lubrication model incorporating measured surface topography. Part 1: theory of flow factors. *Proceedings of the Institution of Mechanical Engineers, Part J: Journal of Engineering Tribology*, 224(4):335–351.
- [64] Sahlin, F., Larsson, R., Marklund, P., Almqvist, A., and Lugt, P. (2010b). A mixed lubrication model incorporating measured surface topography. Part 2: roughness treatment, model validation, and simulation. *Proceedings of the Institution of Mechanical Engineers, Part J: Journal of Engineering Tribology*, 224(4):353–365.
- [65] Sanchez-Palencia, E. (1980). *Non-Homogeneous Media and Vibration Theory*. Springer-Verlag.
- [66] Shi, F. and Salant, R. (2000). A mixed soft elastohydrodynamic lubrication model with interasperity cavitation and surface shear deformation. *Journal of tribology*, 122(1):308–316.
- [67] Shinkarenko, A., Kligerman, Y., and Etsion, I. (2009). The validity of linear elasticity in analyzing surface texturing effect for elastohydrodynamic lubrication. *Journal of Tribology*, 131:021503.
- [68] Shukla, J. (1978). A new theory of lubrication for rough surfaces. *Wear*, 49(1):33–42.
- [69] Stachowiak, G. and Batchelor, A. (2005). *Engineering tribology*. Butterworth-Heinemann.
- [70] Stark, R., Hayka, H., Israel, J., Kim, M., Müller, P., and Völlinger, U. (2011). Virtuelle produktentstehung in der automobilindustrie. *Informatik-Spektrum*, pages 1–9.

- [71] Stupkiewicz, S. (2007). *Micromechanics of Contact and Interphase Layers*. Springer Berlin Heidelberg.
- [72] Stupkiewicz, S. and Maciniszyn, A. (2004). Modelling of asperity deformation in the thin-film hydrodynamic lubrication regime. In *Proceedings of the 2nd International Conference on Tribology in Manufacturing Processes, Nyborg, Denmark, June 15-18, 2004: ICTMP2004*, page 695.
- [73] Szeri, A. Z. (2011). *Fluid Film Lubrication*. Cambridge, 2nd edition.
- [74] Tala-Ighil, N., Fillon, M., and Maspeyrot, P. (2011). Effect of textured area on the performances of a hydrodynamic journal bearing. *Tribology International*, 44:211–219.
- [75] Temizer, İ. (2007). Micromechanics - Analysis of heterogeneous materials (lecture notes). *Institute of Mechanics and Computational Mechanics, Leibniz University of Hanover*.
- [76] Temizer, İ. (2011). Thermomechanical contact homogenization with random rough surfaces and microscopic contact resistance. *Tribology International*, 44(2):114 – 124.
- [77] Temizer, İ. and Wriggers, P. (2010). Thermal contact conductance characterization via computational contact homogenization: A finite deformation theory framework. *International Journal for Numerical Methods in Engineering*, 83(1):27–58.
- [78] Temizer, İ. and Wriggers, P. (2011). Homogenization in finite thermoelasticity. *Journal of the Mechanics and Physics of Solids*, 59(2):344 – 372.
- [79] Torquato, S. (2002). *Random Heterogeneous Materials: Microstructure and Macroscopic Properties*. Springer, Berlin Heidelberg New York.
- [80] Tripp, J. (1983). Surface roughness effects in hydrodynamic lubrication: the flow factor method. *Journal of lubrication technology*, 105(3):458–465.
- [81] Uchidate, M., Yanagi, K., Yoshida, I., Shimizu, T., and Iwabuchi, A. (2010). Generation of 3-D random topography datasets with periodic boundaries for surface metrology algorithms and measurement standards. *Wear*, In Press:Corrected Proof.
- [82] Wagner, W. and Gruttmann, F. (1994). A simple finite rotation formulation for composite shell elements. *Engineering Computations*, 11(2):153–155.

-
- [83] Walowit, J. and Anno, J. (1975). *Modern developments in lubrication mechanics*. Applied Science Publishers.
- [84] Wriggers, P. (2006). *Computational Contact Mechanics*. Springer Berlin Heidelberg, 2nd edition.
- [85] Wriggers, P. (2008). *Nonlinear finite element methods*. Springer Verlag.
- [86] Yang, B. and Laursen, T. A. (2009). A mortar-finite element approach to lubricated contact problems. *Computer Methods in Applied Mechanics and Engineering*, 198(47-48):3656–3669.
- [87] Ziefle, M. (2007). *Numerische Konzepte zur Behandlung inelastischer Effekte beim reibungsbehafteten Rollkontakt*. PhD thesis, Institut für Baumechanik und Numerische Mechanik, Leibniz Universität Hannover.
- [88] Zienkiewicz, O., Taylor, R., and Zhu, J. (2005). *The Finite Element Method: Its Basis and Fundamentals*. Elsevier Butterworth Heinemann.
- [89] Zohdi, T. I. and Wriggers, P. (2008). *An introduction to computational micromechanics*, volume 20 of *Lecture Notes in Applied and Computational Mechanics*. Springer.

Curriculum vitea

Michael Budt
born June 07th, 1978 in Hannover, Germany

Research

since 05/08
10/07 - 04/08

Research staff at
Institut of Continuum Mechanics,
Institut of Mechanics and Computational Mechanics,
Leibniz Universität Hannover,
under guidance of Prof. Dr.-Ing. habil. Peter Wiggers

Study

09/06 - 09/07 Qualification study of “Computational Engineering” for a PhD
position at Leibniz Universität Hannover

10/02 - 08/06 Produktdevelopment at FH Bielefeld, University of Applied
Sciences
Degree: Dipl.-Ing.(FH)

08/04 - 03/05 Semester aboard at University of Manitoba, Winnipeg, Canada

Work experience

07/02-09/02 Mechanic at Werner Kammann Maschinenfabrik GmbH, Bünde

07/01-06/02 Trade representative at C.V.Spar- u. Finanzplanung, Bielefeld

Apprenticeship

07/99 - 06/01 Tool mechanic at Imperial Werke GmbH, Bünde
Degree: Werkzeugmechaniker

Civilian service

07/98 - 06/99 Special school for children displaying behavior and discipline
problems, Schweicheln

School

08/89 - 06/98 Middle and secondary school, Erich-Kästner Gesamtschule Bünde

08/84 - 06/89 Primary school, Grundschule Ennigloh